Evaluation Systems for Intuitive Building Wireless Performance Metrics

Yixin Huang

Department of Electronic and Electrical Engineering

University of Sheffield

Supervisors: Prof. Jie Zhang, Prof. Xiaoli Chu

This thesis is submitted for the approval of the

Doctor of Philosophy

August 2023

This thesis is dedicated to my beloved mom and dad.

Acknowledgements

First and foremost, I would express my greatest appreciation to my supervisor Professor Jie Zhang for his support and trust during my PhD studies. His inspiring teachings and eclectic thinking gave me endless inspiration.

I am really grateful to Professor Jiliang Zhang for his constant help. Thanks to his support, I shaped my own research methodology and study attitudes.

I would like to express my special thanks to Professor Xiaoli Chu, whose encouragement enabled me to start my doctoral study bravely.

I also want to thank my friends and colleagues, Dr Wenfei Yang, Dr Songjiang Yang, Dr Zeyang Li, Dr Yan Jiang and Mr Jixuan Lin, for their accompany and help in my study and life.

Last but not least, I am extremely grateful to my parents for their unconditional love and patience.

Abstract

With the explosive demand for indoor wireless traffic, indoor wireless communication systems are incorporating complex application scenarios and state-of-the-art wireless technologies. As the building structure is a ceiling that inhibits the performance of indoor wireless systems, future building design should consider wireless communication friendliness as a critical component. This thesis evaluates the impacts of building structures on different performance indicators for indoor wireless systems. The thesis proposes a general building wireless performance (BWP) evaluation scheme to define BWP metrics so that each metric can systematically characterise the influence of architectural design on one performance indicator of the indoor wireless system.

Firstly, this thesis defines the impact of buildings on the root-mean-square (RMS) delay spread (DS) of the wireless system as the BWP metric, DS gap, and provides the evaluation method. By contrast, previous studies only focused on the BWP of the system's received power and interference intensity. For a given building design, an analytical solution for calculating the DS gap is derived by comparing the expectation value of the RMS-DS of the wireless system in the building under design (BUD) with the expectation value of the RMS-DS of the wireless system in the same-sized open space. Using the DS gap, architects can quickly evaluate the impact of a building design on the DS of an indoor wireless system, thereby alleviating the building's contribution to the inter-symbol interference (ISI) of indoor wireless systems.

Secondly, considering that massive multiple-input multiple-output (MIMO) systems are being introduced indoors, this thesis defines the BWP metric, channel hardening obstruction (CHO), of how destructive the building is to channel hardening in indoor massive MIMO

systems. An analytical solution of CHO for a given antenna number of massive MIMO is derived, and an approximate closed-form solution is also present. Similar to DS gap, CHO enables architects to rapidly analyse the massive-MIMO-friendliness of a building design.

Finally, a general scheme for defining BWP metrics is proposed based on the aforementioned evaluation approaches. This scheme can quantify the impact of building structures on various propagation-environment-sensitive wireless performance indicators. The planar shape of the evaluated building and its rooms can be irregular. The proposed scheme has robust scalability and usability. By simulating the line-of-sight (LOS) probability model and the same-room probability model of a small number of irregular rooms, architects can quickly calculate the different BWP metrics of large-quantity architectural designs to finally determine a more wireless-friendly architectural design. The works in this thesis broadens the application scenarios for BWP evaluation and provides an essential foundation for designing and optimising future 6G smart buildings.

List of Publications

Published

Yixin Huang, Haonan Hu, Jiliang Zhang and Jie Zhang, "Foam Evolution Inspired Modeling for Staged Construction of Ultra-Dense Small Cell Network", *IEEE Access*, vol. 9, pp. 35431-35438, Feb., 2021.

Yixin Huang, Jiliang Zhang and Jie Zhang, "Building Wireless Performance Evaluation of Channel Hardening for Massive MIMO System",*IEEE Communications Letters*, vol. 27, pp. 1874-1878, Jul., 2023.

Accepted

Yixin Huang, Jiliang Zhang and Jie Zhang, "Wireless Channel Delay Spread Performance Evaluation of a Building Layout",*IEEE Transactions on Vehicular Technology* (Chapter 3)

Yixin Huang, Jiliang Zhang and Jie Zhang, "A Building Wireless Performance Evaluation Scheme in terms of Root-Mean-Square Delay Spread for Buildings with Complex Structures", *2023 IEEE International Conference on Communications Workshops (ICC Workshops)*, May, 2023 (Chapter 5)

Table of contents

List of figures

List of tables

Abbreviations

1D One-Dimensional

2D Two-Dimensional

2G Second Generation

3D Three-Dimensional

3G Third Generation

3GPP Third Generation Partnership Project

4G Fourth Generation

5G Fifth Generation

6G Sixth Generation

AOA Angle of Arrival

APs Acess Points

AR Augmented Reality

ASE Area Spectral Efficiency

BSs Base Stations

BUD Building Under Design

BWP Building Wireless Performance

CAPEX Capital Expenditures

CDFs Cumulative Distribution Functions

CHO Channel Hardening Obstruction

CSI Channel State Information

DS Delay Spread

EB Exabytes

eMBB Enhanced Mobile Broadband

EM Electromagnetic

FoM Figure of Metric

GPP Ginibre Point Process

HBF Hybrid Beamforming

HetNet Heterogeneous Network

IG Interference Gain

IoT Internet-of-Thing

ISI Inter-Symbol-Interference

IRT Intelligent Ray-Tracing

LOS Line-Of-Sight

MBP Measurement-Based Prediction

MHCPP Matérn Hard Core Point Processes

MIMO Multiple-Input-Multiple-Output

MPLP Manhattan Poisson Line Process

mMTC Massive Machine Type Communication

MR Mixed Reality

MUs Mobile Users

NLOS Non-Line-Of-Sight

OPEX Operational Expenditure

PCP Poisson Cluster Process

PDF Probability Density Function

PG Power Gain

PHP Poisson Hole Process

PLP Poisson Line Process

PPP Poisson Point Process

QoS Quality of Service

RF Radio Frequency

RMS Root-Mean-Square

RSS Received Signal Strength

Rx Receiver

SINR Singnal-to-Interference-and-Noise-Ratio

Tx Transmitter

UHF Ultra-High Frequency

ULA Uniform Linear Array

URLLC Ultra-Reliable Low Latency Communications

UTD Uniform Theory of Diffraction

UWB Ultra Wide Band

VR Virtual Reality

XR eXtended Reality

Chapter 1

Introduction

Overview

Over the last decade, the proliferation of high-traffic software applications has led to exponential growth in wireless traffic, the vast majority of which occurs indoors. Designing the indoor wireless system to satisfy the increasing wireless traffic demand has become a research hotspot. As a result, increasingly new wireless technologies are being introduced to improve indoor wireless performance. Building Wireless Performance (BWP) is a concept proposed to improve the indoor wireless performance threshold from the building design perspective. However, the research of BWP is still in the initial stage, and many basic studies are left in the blank field. This motivates the thesis to fill a gap in the field of rapid and intuitive indoor wireless performance evaluation of building design.

In this chapter, the research background of this thesis will be first introduced, followed by the research motivations and thesis contributions. Finally, the organisation of the thesis will be presented.

1.1 Background

1.1.1 Requirement of Indoor Wireless Systems

With the popularity of smartphones and smart vehicles, the promotion of visualisation services, and the marketisation of extended-reality (XR)-type application scenarios (such as Virtual Reality (VR), Augmented Reality (AR), and Mixed Reality (MR)), mobile traffic demand has entered a high-speed explosion [1–4]. According to Ericsson's 2022 annual report, global mobile data is growing at a rapid rate of 4 Exabytes (EB) per year, from nearly 90 EB by the end of 2022 to an estimated 325 EB by 2028 [5]. Fig. 1.1 shows the trend of global traffic growth in the last decade and the forecast for future growth. Since most application scenarios require a stable and safe environment, people routinely use traffic-demand services in offices, schools, homes, or shopping malls. High-definition video conferencing, telecommuting, cloud gaming, and the Internet-of-Thing (IoT) require constant access to unlimited data. As a result, 80% of the tremendous rise in traffic demand occurs indoors, and it will be considerably more urgent than anticipated as new services proliferate [6].

In an urban network deployment, most Base Stations (BSs) are placed outdoors to serve indoor Mobile Users (MUs) through walls or windows. Signals experience severe attenuation as they pass through walls and windows, so indoor MUs often experience vastly different network performance in different locations, often far worse than outdoors. Placing Acess Points (APs) indoors improves the experience to a large extent. However, for offices, schools, hospitals, shopping malls, and other crowded places with high traffic demand, the installation of indoor APs is approaching saturation. While the number of MUs remains stable, the demand for personal mobile traffic is rising rapidly, resulting in the current indoor wireless system being gradually unable to fully cover users' needs [7–10].

Indoor wireless requirements constantly vary with application scenarios, and such requirements for wireless systems in different application scenarios are usually defined as the Quality of Service (QoS) [11]. These QoS indicators can be related to the system's capacity. For example, most scenarios require the system's Received Signal Strength (RSS) or

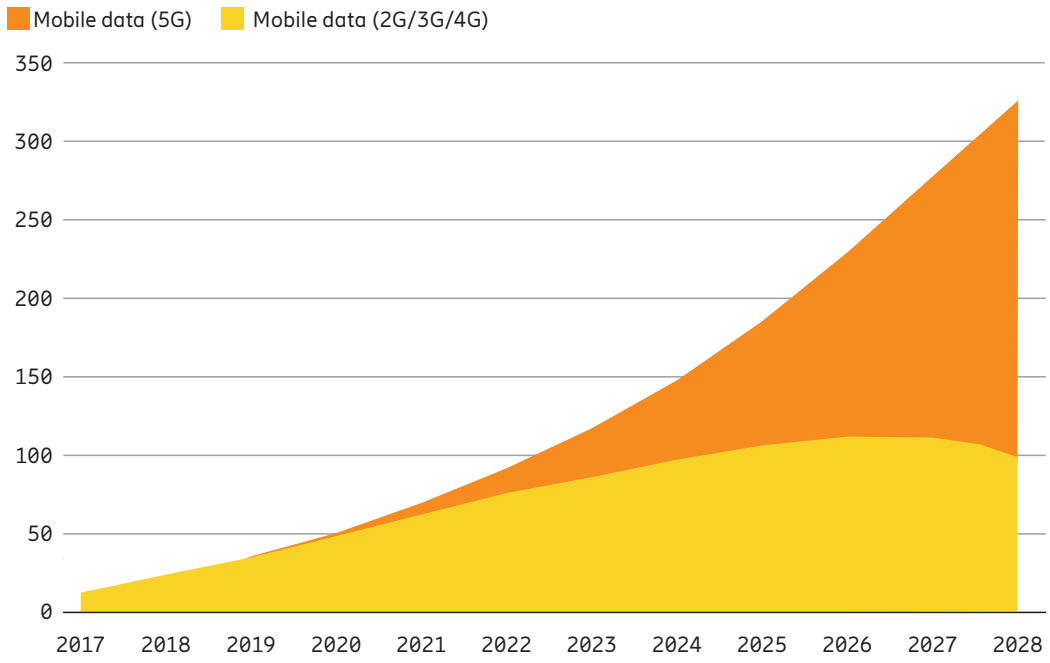

Fig. 1.1 Global mobile traffic trend [Source: Ericsson mobility report 2022].

Singnal-to-Interference-and-Noise-Ratio (SINR) to be no lower than a certain threshold [12]. It can also be reliability-related. For example, Ultra-Reliable Low Latency Communications (URLLC) usually require the minimum reliability and delay provided by the system [13, 14]. The increased performance requirements imposed by these innovative application scenarios necessitate the upgrading of indoor wireless system technologies.

1.1.2 Technologies to Improve Indoor Wireless Performance

The ultra-dense small cell network is current research hotspot of the indoor wireless system. Ultra-dense small BSs usually transmit high-frequency signals for communication [7, 15]. The Fifth Generation (5G) system can operate in a broader range of carrier frequencies, in which higher frequencies can carry a larger network capacity due to their larger distributable bandwidth. By contrast, high frequency has a smaller coverage area, which makes it more adaptable indoors [16].

Ultra-dense small cell networks can provide high capacity, high density and high-quality wireless communication service for indoor wireless communication systems. On the one hand, deploying multiple small cell BSs in indoor areas can greatly improve the network's capacity and user connection density. Consequently, more users can simultaneously connect and enjoy high-speed data transmission and stable communication services. On the other hand, introducing the spectrum resource reuse technology of ultra-dense small cell networks can effectively reduce interference and improve the anti-interference ability of the system, which is important in indoor environments where multipath propagation and interference are significant, providing better signal quality and a more stable connection.

Massive Multiple-Input-Multiple-Output (MIMO) systems are also being introduced into indoor wireless systems. The massive MIMO system provides greater signal strength and more stable signal transmission by utilising a large number of antennas and beam-forming techniques. This allows indoor users to get higher data rates, more stable connections and a better user experience. In addition, the massive MIMO system can reduce multipath effects and interference in indoor environments, improving channel capacity and system reliability. Therefore, the massive MIMO system plays a crucial role in meeting the wireless demand of indoor wireless communication, such as high-speed indoor networks, IOT applications, and indoor location services.

Conventional indoor massive MIMO systems are limited to 4-transmitter-4-receiver, whereas in a distributed massive MIMO system, multiple distributed antennas can be integrated into a single logical unit, and the capacity of 64-transmitter-64-receiver active antenna units or more can be achieved. A study by Huawei confirmed that using distributed massive MIMO has a 3-4 fold increase in uplink and downlink capacity compared to four-way cellular splitting [17].

Multi-user (MU) MIMO is also being introduced into indoor wireless systems [18]. Indoor wireless communication systems usually adopt multiple antennas to implement MIMO technology. In MU-MIMO, these antennas can be deployed in base stations, wireless APs, and user devices to enable simultaneous communication with multiple data streams between user devices. MU-MIMO technology involves the simultaneous transmission of

data between multiple user devices. This requires optimization in signal processing and scheduling algorithms to achieve data flow allocation and scheduling among multiple user devices. This includes directional transmission of signals to different user devices through beam-forming and space-time coding techniques, reducing interference and improving signal quality. In order to implement MU-MIMO technology, the base station or wireless AP ought accurately estimate the channel condition in the indoor environment as to obtain better signal quality and system performance [19].

The MU-MIMO system is mainly used in user-dense, concurrent large traffic and relatively fixed terminal locations, such as offices, conference centres, and electronic classrooms. It can bring significant benefits to wireless networks. MU-MIMO technology can effectively improve the throughput of wireless networks. Compared to single-user MIMO (SU-MIMO), wireless networks using MU-MIMO can typically increase throughput by 2-3 times. MU-MIMO allows data to be transmitted to multiple terminals simultaneously rather than being limited to one terminal. MU-MIMO technology enables multiple terminals to transmit data concurrently, thus improving data transmission efficiency in wireless networks. It reduces terminal latency in waiting time and can better meet the needs of video, audio and other high-traffic, low-latency applications. Because of that, wireless networks have more idle time or capacity to serve traditional SU-MIMO-only Wi-Fi terminals, so the application experience of traditional Wi-Fi terminals will also be improved. Therefore, MU-MIMO technology can significantly improve the throughput of wireless networks, improve data transmission efficiency, and positively impact the application experience of traditional Wi-Fi terminals in indoor wireless systems [20].

Device-to-device (D2D) communication in 5G networks encompasses numerous application scenarios, offering numerous benefits [21]. It facilitates direct data transmission between users, enhancing user experience while conserving network resources. Moreover, D2D communication plays a critical role in emergencies. D2D communication can still establish a wireless network and enable communication between devices when traditional communication networks are damaged or unavailable. Additionally, D2D communication

enhances IoT applications by enabling D2D connectivity and resource sharing, enabling seamless interconnection among IoT devices.

For enabling D2D communication, it is essential to address the detection and recognition of neighbouring D2D terminals, which poses a significant research challenge. For instance, in ultra-dense small cell networks, detecting D2D terminals becomes more complex. Furthermore, the wireless resource management problem becomes more intricate due to the inclusion of various communication modes like broadcast, multicast, and unicast, as well as diverse application scenarios such as multi-hop and relay. D2D communication based on cellular networks introduces additional interference into the existing cellular communication, emphasising the need to study power control and interference coordination for effective 5G network D2D implementation [22].

1.1.3 Challenges Brought by New Technologies

Introducing new technologies into indoor wireless systems brings new challenges. The higher path loss in the propagation of high-frequency signals becomes a significant issue in indoor wireless system design. Path loss increases when blockage exists in the link compared to a Line-Of-Sight (LOS) link, and countable Non-Line-Of-Sight (NLOS) links occur more frequently indoors due to ubiquitous walls and interior furnishings [23, 24]. Therefore, the building structure seriously affects the system capacity for indoor wireless systems.

Furthermore, the complex indoor structure will bring about more severe multipath effects than outdoor propagation environments. A large number of random subchannels have different path loss and propagation times, resulting in the larger Delay Spread (DS) and more significant difficulties in estimating the signal strength of a channel, thus increasing the precoding complexity and, ultimately, decreasing the system capacity and reliability [25–28]. Encouragingly, in the massive MIMO system, the channel hardening effect can reduce the subchannel randomness caused by the multipath effect [29]. The channel hardening effect is also related to propagation environments. When the propagation path is blocked, or a small hole effect exists, the channel hardening will attenuate, thus reducing the reliability of the channel [30].

Radio Frequency (RF) engineers improve the performance of indoor wireless systems by optimising their deployment and configuration [31]. Since the performance of an indoor wireless communication network is upper-bounded by the building itself, in some cases, RF engineers find that no matter how they deploy the wireless network, the indoor wireless system cannot meet the performance requirements for indoor wireless services. Therefore, costly and time-consuming building retrofits may become a last resort to meet wireless performance requirements in these scenarios.

1.1.4 The Study of BWP

The propagation environment in indoor wireless systems is more complex compared to outdoor systems due to the presence of building structures. This complexity leads to increased signal attenuation, reduced SINR, and lower system capacity. Indoor communications also suffer from severe multi-path effects, resulting in larger channel delay spread, decreased coherence bandwidth, and increased Inter-Symbol-Interference (ISI). These factors negatively impact both the capacity and reliability of the wireless communication system. Fig. 1.2 illustrates the difference in signal propagation between a building and an open space, highlighting the varying blockage conditions and room structures in the building. In contrast, the Transmitter (Tx)-Receiver (Rx) links in the open space experience the same LOS propagation conditions.

The impact of building structures on indoor wireless system performance is becoming non-negligible with the advancement of novel technologies and the higher performance requirements of new application scenarios. Hence, the definition and assessment of the influence of architecture on indoor wireless system performance have emerged as the latest study path of wireless systems, and the theory of BWP has been proposed. BWP describes the difference in the wireless performance of indoor wireless systems compared to the same configuration in the open space [31–33].

The significance of introducing BWP has two aspects. First, the BWP evaluation provides architects with a quantifiable analysis tool to incorporate various wireless performance indicators into the factors that need to be balanced in architectural design, and ultimately

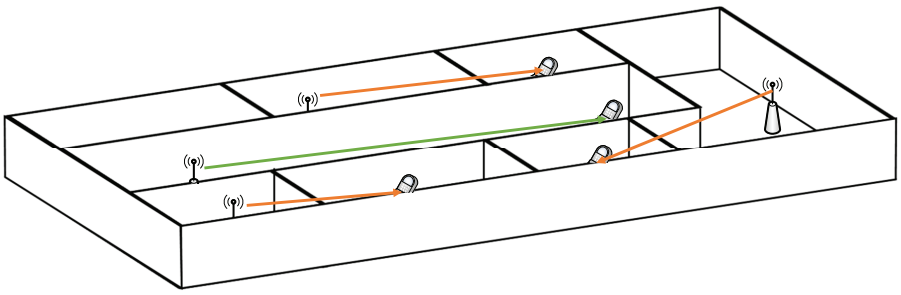

(a) Randomly generated links in the Building Under Design (BUD).

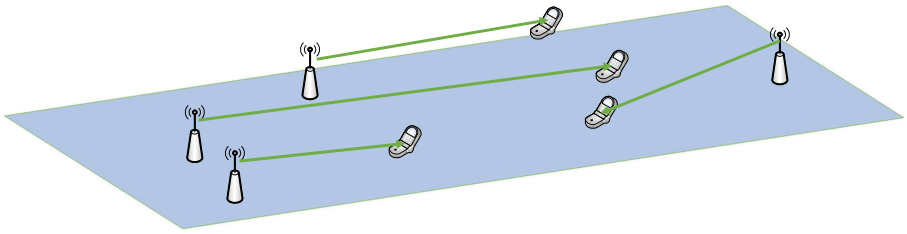

(b) Randomly generated links in the same-sized open space.

Fig. 1.2 The impact of building structures on the wireless system.

enhance indoor wireless system performance from the architectural design perspective. Second, wireless network researchers can refer to the BWP evaluation metrics when designing wireless systems to meet higher performance requirements.

In the current research on BWP evaluation, it is necessary to simplify the assumptions about building structures to develop a practical evaluation method. This paper aims to investigate the impact of buildings on wireless communication systems from various perspectives. The following assumptions are applied to the evaluated building and wireless communication system to realise the tractability of the proposed method.

- This thesis focuses on the impact of single-storey buildings on the performance of wireless communication systems. Therefore, the structure of the building, the layout of the rooms, and the Tx and Rx unknowns within them are approximated by their projection on a Two-Dimensional (2D) plane. In chapters 3 and 4, the building and its rooms are assumed to be rectangular. In Chapter 5, the building and its rooms can be assumed as any arbitrary shape. The thickness of the wall is ignored.

- To decouple the transceiver locations from the BWP evaluation, this these assumes both Txs and Rxs of the wireless system are randomly distributed in the evaluated building.

- Different performance parameters require the use of different empirical or physical models. Therefore, for the assessment of BWP, the communication environment of the rooms in the test building is assumed to be consistent with the empirical model. In Chapter 3, the rooms are categorized into offices and corridors, and their communication environment is assumed to be consistent with the building described in [34]. In Chapters 4 and 5, the communication environment within the building is assumed to be consistent with the environment of scenario A1 in the WINNER II project [35].

- Transceiver links are all assumed to be LOS in the open space. Chapter 3 applies the Two-ray model for evaluation in open space. In chapters 4 and 5, the open space scenario is assumed to be consistent with the environment of scenario B5a in the WINNER II project [35].

1.2 Motivations

At present, the research on BWP is still in its infancy. The impact of building structure on the wireless system's interference strength and signal strength was defined as metrics, and mathematical models have been built. Based on this, the technical status and future development prospects of BWP have been summarised, and a research scheme has been proposed, laying the groundwork for the upcoming indoor wireless system's capacity expansion. These studies on BWP are based on the known Tx and Rx locations and can provide the intensity distribution of target metrics on the map of a BUD.

This thesis aims to study the BWP to fill more gaps that deserve attention and systematic description. Some of the motivations are summarised as follows:

- Existing BWP studies are dedicated to describing performance metrics that affect system capacity. However, more research is needed on the performance indicators that affect system reliability, which is vital for updating application scenarios. As a result, different wireless performance indicators that can describe system reliability should be included in the definition and modelling of the BWP evaluation scheme. In addition, as new technologies are introduced into indoor wireless network designing, the system performance indicators related to the new technologies also need to be included in the BWP evaluation system.

- The existing BWP evaluation system employs a predefined network layout for the BWP evaluation of buildings. However, the actual BWP evaluation is usually carried out during the building design phase, leaving the deployment of the wireless system uncertain. Therefore, it is necessary to construct BWP evaluation schemes under the premise of unknown network deployment.

- Various new technologies and application requirements are continually introduced into indoor wireless systems, which are difficult for architects and RF engineers to predict. Therefore, a general method and model that can evaluate the different indicators of the BWP are urgently needed. On this basis, the output of a BWP evaluation scheme should be intuitive and easy to understand to facilitate architects to evaluate the architectural design quickly and to assist RF engineers in guiding wireless system layout for an architectural design.

1.3 Contributions

The main research contributions of the thesis are summarised as follows:

Firstly, the metric of DS gap as G_τ is defined by comparing the expected Root-Mean-Square (RMS)-DS within a BUD to the RMS-DS in a same-sized open space. The metric helps architects avoid ISI at the building design stage and assess a building's wireless friendliness from both capacity and reliability perspectives. The contributions are four-fold:

- The first evaluation approach for BWP in terms of channel DS is proposed. The associated evaluation metric, namely the DS gap, is defined to capture the impact of a building on the DS of indoor wireless transmission in it.
- A statistical model for the proposed metric is also derived for quick and accurate metric calculation. The PDF of RMS-DS is deduced according to the room layout of the assessed building, and the analytic expression of the metric DS gap is derived.
- The proposed analytical model is verified by the Monte-Carlo simulation, and the results show that the analytic results match simulation results very well.

Secondly, a novel BWP metric, Channel Hardening Obstruction (CHO), is defined, by comparing the ratio of average channel hardening ratios of all possible channels in the BUD and the average channel hardening ratios of all possible channels in the same-sized open space. The metric CHO helps architects assess the friendliness of BUD to the channel hardening of indoor massive MIMO systems. The contributions are three-fold:

- The first evaluation approach for BWP regarding channel hardening of the indoor massive MIMO system is proposed. The associated evaluation metric, namely the CHO, is defined and derived to capture the impact of a building on the channel hardening ratio of the indoor massive MIMO system in it.
- A closed-form approximation model is derived to quickly and accurately calculate the metric, where the impact of spatial correlation on channel hardening is considered.
- The proposed model is verified by the Monte-Carlo simulation. The proposed model shows the potential for rapid evaluation in future architectural design.

Thirdly, a general BWP evaluation model for more complex architectural design structures is proposed to statistically evaluate building structures' impact on various indoor wireless systems' performance indicators. Introducing the proposed scheme into construction practices can effectively help architects quickly evaluate different wireless performance indicators of building design to improve the performance of future indoor wireless systems. The contributions are four-fold:

- The first general BWP evaluation scheme for various wireless performance indicators is proposed. For any performance indicator of an indoor wireless system, the influence of a building structure on it can be summarised into a numerical metric to be visually quantified by the proposed scheme.

- General statistical models for the target indicator of randomly generated Tx-Rx links are derived for quick and accurate BWP evaluation.

- A polynomial fitting method for approximating the LOS probability and same-room probability of the Tx-Rx link is introduced when Tx is located in an irregular-shaped room. Fitting functions for typical irregular shapes are listed. The proposed fitting functions can simplify the computational complexity and effort of complex building structures with irregular-shaped rooms.

- The RSS, RMS-DS and channel hardening ratio are evaluated via the proposed scheme as examples of performance indicators of the BWP and compared with the Monte-Carlo simulation results, verifying that the scheme can significantly reduce the computation time while ensuring accuracy.

1.4 Thesis Outline

The rest of the thesis is outlined and introduced as follows:

Chapter 2 firstly summarises the application scenarios and performance requirements of indoor wireless systems and reviews the modelling methods of indoor wireless channels. The concept of BWP is then introduced. Finally, the research history of the performance indicators of concern, i.e., the DS and the channel hardening ratio, are retrospected. It provides detailed descriptions of the models that may be cited or improved. Then, the potential challenges in these existing studies are analysed.

Chapter 3 proposes the earliest systematic BWP evaluation approach dedicated to RMS-DS to bridge the gap between the BWP evaluation and channel DS modelling. More specifically, Chapter 3 defines a metric, namely DS gap, to capture the impact of a building

on the RMS-DS of wireless connections in it. Subsequently, an analytical model of the RMS-DS is proposed to facilitate quick DS gap evaluation given a building layout.

Chapter 4 proposes a new system-level evaluation method for channel hardening in indoor massive MIMO systems to bridge the gap between the BWP evaluation and the channel hardening modelling of indoor massive MIMO systems. Specifically, Chapter 4 presents a novel BWP evaluation metric, CHO, to evaluate the influence of a BUD on channel hardening. The analytical model and the approximation closed-form expression of the proposed evaluation metric are also given in detail to assist architects in quickly quantifying the impact of an architectural design on the performance of an indoor wireless network in channel hardening.

Chapter 5 integrates the characteristics of the above performance indicators, and provides a more general evaluation scheme for various wireless performance indicators. The proposed evaluation scheme can evaluate the BWP of building designs in terms of various wireless performance indicators. Moreover, the proposed scheme can be applied to complex building structures with rooms in irregular shapes, which is different from the assumption in previous chapters that both buildings and rooms are assumed to be rectangular.

Chapter 6 concludes the thesis and discusses future research directions based on the current work.

Chapter 2

State-of-the-Art and Research Challenges

Overview

This chapter first reviews the application scenarios for indoor communication systems facing higher performance requirements and introduces the methods in indoor communication systems modelling. Secondly, this chapter reviews the current indoor channel modelling methods and performance evaluation methods, and then introduces the concept of BWP, which helps expand the performance of indoor communication systems. Thirdly, this chapter reviews the modelling and measurement studies of some performance indicators, such as DS and channel hardening ratio, that affect the performance of indoor communication systems yet are not included in the BWP evaluation system. The potential challenges in the reviewed works are analysed at the end of the chapter.

2.1 Reviews of Indoor Wireless Communications

Indoor wireless traffic has accounted for more than 80% of the total communication system, and different wireless communication scenarios applied to indoor wireless systems have different performance requirements. This section reviews the new application scenarios for 5G systems and summarises their performance requirements for indoor wireless systems. In addition, the building's walls, floors, furniture and human activity will impact the Electromagnetic (EM) wave transmission, reflection, refraction, scattering, diffraction and other

propagation behaviour. Therefore, the indoor channel must be modelled in combination with the building structure. This section also reviews the empirical, physical, and hybrid models of channel modelling.

2.1.1 Application Scenarios in Indoor Wireless Communications

Indoor scenarios have always been the most common environments for humans to work, study, and live. As people's wireless demands increase, indoor wireless systems have evolved and improved from the Second Generation (2G) to 5G era. However, 5G systems present more advanced application scenarios that require more incredible wireless performance, and IMT-2020 proposes three prominent use cases covering future mobile communication scenarios: Enhanced Mobile Broadband (eMBB), Massive Machine Type Communication (mMTC) and URLLC [36]. Fig. 2.2 shows the most representative usage scenarios of the three technologies and their enhanced requirements for wireless communication, especially for indoor wireless communication systems.

The eMBB is one of the first 5G main use cases as the extension of Fourth Generation (4G) services. In addition to satisfying multimedia consumption, it supports staff telecommuting and seamless wireless connectivity for indoor devices. The eMBB will eventually enable real-time interaction for immersive VR and AR. In densely populated areas, eMBB use cases necessitate a higher wireless capacity to facilitate access to a greater range of mobile users. Furthermore, more reliable linkages are essential for allowing effective access from any location in the scenario and for presenting consumers with a more consistent experience. In compliance with the enhanced experience of the operated services, the eMBB imposes more expectations on wireless systems.

The mMTC supports linking large-scale devices in IoT applications, which are primarily indoors. Unlike eMBB, the communication activity of mMTC devices is intermittent and requires lower and more stable transmission rates, whereas the density and range of connected devices are crucial. In addition, due to the large-scale IoT that requires monitoring different devices for long periods, mMTC requires devices to communicate with higher energy efficiency to maintain low-cost management for long working periods.

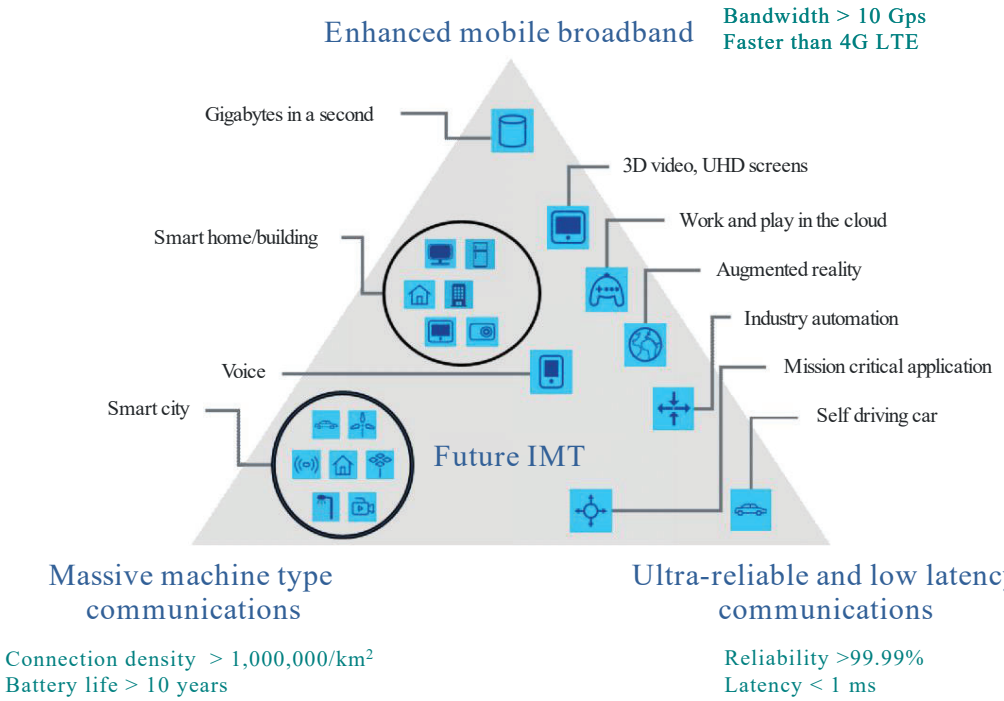

Fig. 2.1 Usage scenarios for eMBB, mMTC and URLLC [Source: IMT-2020].

The URLLC defines the minimum requirements for wireless communication systems to provide high reliability and extremely low latency communication. In indoor scenarios, URLLC is typically used to support industrial automation, real-time human-machine collaboration, and other use cases. Compared to mMTC, URLLC provides intermittent communication transmission activities for fewer devices but requires high predictability of communication resources and high system reliability.

2.1.2 Indoor Wireless Channel Modelling

For RF engineers to determine whether the performance of the wireless system satisfies the use case requirements, channel modelling has become mandatory. During the wireless system design stage, accurate channel models can precisely anticipate the performance of a system installed at multiple locations across the building to guarantee the system's performance in use. Moreover, channel modelling can optimise indoor wireless systems. An accurate

propagation model at the design stage can help RF engineers estimate the antennas' service coverage and choose suitable deployment locations for wireless systems such as ultra-dense small-cell networks. Channel modelling can also help evaluate the performance of wireless systems whose practical measurements are challenging. When some measuring sites in the actual building have restricted access permissions, the only option for estimating the performance of these indoor wireless networks is to use channel models.

Models can be built in different methods. Researchers can evaluate various performance indicators in real-world scenarios and determine the performance indicators' mathematical models by fitting the measurements. The model created by this method is known as an empirical model [37]. This modelling approach involves less in-depth environmental data but delivers a more comprehensive model in a scenario. Nevertheless, the settings of the scenario and the wireless system also play a crucial part in this strategy. The accuracy of the empirical model cannot be maintained when the estimated scenario deviates significantly from the empirical scenario or when the operating frequency of the wireless system varies, requiring extensive extra measurements and parameter fitting.

The measurement results directly influence the establishment of the empirical model. Ergo, the error between the model and the real measurement can be minimised by adjusting parameters and determining variables according to various transmission conditions, building structures, and frequencies.

Taking the path loss model as an example, the simplest path loss model constructs the function using the transmitting and receiving distance as the dependent variables and modifies the path loss exponent parameter to match the measured value. Since the model does not incorporate any propagation environment or frequency-related variables, the path loss exponent value must be refit for every channel whose frequency or propagation environment alters. As a result, additional empirical path loss models are constructed and considered. The Keenan-Motley Model adds variables for the number of walls and floors to the fundamental path loss model, allowing users to predict wireless system performance in buildings with several rooms using the same model [38]. The path loss resulting from the number of floors is modelled by a nonlinear function in the ITU-R indoor model, which further improves

the accuracy of cross-floor path loss estimation [39]. More breakpoints are set in other empirical models to improve accuracy. In order to allow the empirical model to be utilised to obtain accurate results quickly in a carrier band (900-1800MHz), the Ericsson radio system model establishes four breakpoints for the variable transmit-receive distance [40]. Naturally, the drawback is the typical circumstance of a narrowly available frequency. In addition to considering the effects of wall, floor, and frequency, the Tuan Empirical Indoor Model also considers the impact of the angle of incidence between signal and wall on path loss [41]. The model is able to simulate frequencies between 900 MHz to 5.7 GHz, albeit parameter readjusting after changes in the building environment still necessitates several measurements.

In addition, depending on the fundamental physical mechanism, researchers can derive performance indicators for various scenarios, and the models developed using this method are classified as physical models [37]. To establish further system design concepts, the physical model may be employed to perform extensive parameter modifications and study more relationships between various parameters and indicators. Since it is difficult to gather a significant amount of exact data in the actual scenario, it is frequently difficult for the estimated results derived using the physical model to closely match the observed values of a real system. To develop a more accurate physical model, additional scenario factors must be entered, boosting computational complexity.

The most prevalent modelling technique for indoor channel physical modelling is ray tracing. By applying the precise input of building geometry, construction materials, and other characteristics, it is possible to anticipate the specific performance indicators of the target site accurately. Ray tracing necessitates the prediction of all possible ray trajectories between the transmitting and receiving ends. In addition to the unobstructed direct propagation, the performance evaluation of the transceiver system must incorporate signal transmission created by numerous ray paths, such as reflection, secondary reflection, refraction, and diffraction of the object's surface in the propagation environment. Different materials and shapes of walls, floors, windows, and decorations must be estimated independently, which considerably increases the complexity and feasibility of computation. In that case, appropriate simplifying assumptions are required for ray tracing, such as presuming that walls and floors are flat

and that each surface has identified simple electromagnetic properties. These assumptions, evidently, increase the disparity between the physical model and actual measurements. Ray tracing is now concentrating on how to simplify the model in order to minimise processing complexity while preserving accuracy.

The Honcharenko-Bertoni Model divides the indoor communication environment into a congested area near the floor (such as a furniture area on the floor and a hanging light fixture) and an area near the free-space-like in the centre of the floor [42]. In order to create a ray tracing model, attenuation and reflection of walls and diffraction in chaotic regions are modelled in this model. In order to provide accurate predictions regarding the multipulse response of radio propagation, site-specific models employ geometric optics principles [43]. In this model, importing comprehensive AutoCAD interior layout plans and retaining those objects significantly larger than the wavelength enhances the accuracy. To boost accuracy even further, the model accounts for all possible emission angles at the transmitting end, whereas it does not assume that all rays would be received at the receiving end. This method can integrate as many pathways as possible into the calculation, but at the expense of a substantial increase in calculation time.

The calculation time for particular channels within the building can be considerably decreased when the building is preprocessed prior to computation. The intelligent ray-tracing (IRT) model accounted for the shadow effect of walls, the waveguide effect of corridors and the debris-caused diffraction effect, and generated a simplified hypothesis of the indoor environment [44]. In this modelling approach, obstacles in building data are segmented into pixel blocks, and the visible relationship between each pixel block is examined and recorded before channel estimation. In channel prediction, the channel performance between incoming and outgoing pixels can be promptly calculated due to the established relationship between each location. Complex preprocessing inevitably results in lengthy computation times, which entails further optimisation.

Combining the minimal processing complexity of the empirical model with the comprehensive parameter modification and the powerful universality of the physical model, the hybrid model predominates [37]. In general, the hybrid model uses the physical principle as

the framework, and it uses the empirical model to alter the parameters inside the model. This enables the hybrid model to produce more accurate predictions yet requires less processing.

The Reduced-Complexity Uniform Theory of Diffraction (UTD) Model incorporates a number of different physical models, one of which is a theory of uniform diffraction [45]. In the meantime, the empirical model of signal attenuation of walls and floors, which is correlated with various materials and the angles between transmission pathways and walls and floors, is produced by measuring. The Reduced-Complexity UTD Model can maintain its accuracy in more varied application circumstances since it uses both advanced ray tracing and empirical methods. Another approach that combines physical and empirical models is Measurement-Based Prediction (MBP) [46]. This method initially fits a distance-dependent path loss model independent of the propagation environment by measuring fading at a material- and layout-specific location. Fading data relevant to the environment and accounting for shadows are acquired by comparing the measurement values with the fitted empirical model outcomes, which are challenging to calculate using the physical model. These fading data and path loss models are processed and preserved to be reused in other structures. Including frequency, floor, and wall loss components into the path loss model is effortless, confirming that the MBP can estimate the complicated situation at various frequencies and that the model accounts for shadows cast by walls and furniture in the scene. As a consequence of its broad variety of application situations and correctness, the computation burden calculated by this approach is acceptable.

Table 2.1 classifies these channel modelling approaches for better comparison.

2.1.3 Tractable Approaches of Wireless System Evaluation

Appropriation deployment strategies and propagation environments must be assumed to evaluate network performance. Researchers in [47] configured the deployment to a One-Dimensional (1D) linear cellular array and 2D hexagonal cellular pattern in order to simplify the calculation and rapidly examine the true wireless system's performance. In this con-

Table 2.1 Indoor wireless channel modelling

Channel modelling approaches		Reference
Empirical model	Keenan-Motley model	[38]
	ITU-R indoor model	[39]
	Ericsson radio system model	[40]
	Tuan empirical indoor model	[41]
Physical model	Honcharenko-Bertoni model	[42]
	Site-specific model	[43]
	IRT model	[44]
Hybrid model	UTD model	[45]
	Measurement based prediction	[46]

figuration, the signal received by the receiver is composed of the signal transmitted by the transmitter in the same cell, the signal transmitted by the transmitter in nearby cells multiplied by the interference factor α $(0 < \alpha < 1)$ and Gaussian noise. When each cell can handle a large number of users, the network performance of the system is evaluated by the maximum rate that each transmitter in the cell can achieve according to Shannon's theory. Researchers in [48] expanded the evaluation model to consider the impact of fading on the system and presented an evaluation model of achievable rates. In [49], the evaluation model of a straightforward 1D linear cellular array was expanded to evaluate general linear or planar structures.

Stochastic geometry has been utilised extensively in biology, astronomy, and other fields and plays an increasingly significant role in communication network research. Stochastic geometry was first used to explain interference in wireless networks in 1978 [50]. Since then, the mathematical works in [51, 52] have served as essential references for network communication researchers. The core of stochastic geometry in mathematics investigates random phenomena in two and higher dimensions where spatial point processes are required [53]. Point processes are the most fundamental object of study in stochastic geometry. A point process can be defined as a random set of points in space or a measurable mapping from points in a probability space to points in Euclidean space. When the process is Poisson distributed, it is called the Poisson Point Process (PPP) [51].

The implementation of PPP provides a practical computing foundation for base station distribution and performance evaluation. Andrews et al. in [54] modelled the 2D BSs distribution as a homogeneous PPP and calculated this stochastic geometry model's outage probability and average rate. When compared to the traditional method of using a grid to model the base stations uniformly and the Monte Carlo method to calculate network performance, this method of using PPP to simulate the location of the base stations (with the same BS density as the grid model) can simplify complex operations into closed forms that can be rapidly calculated. In terms of evaluation precision, the lower bound of network performance derived by PPP modelling work is more credible than the looser upper bound supplied by conventional grid modelling work.

Researchers in [55] proposed a soft-core point process, Ginibre Point Process (GPP), between the low regularity of PPP and the high regularity of Matérn Hard Core Point Processes (MHCPP) to handle the problem of base station location modelling and network evaluation and to further improve the operability of the study. In [55], the researchers evaluated the system with β-GPP BS deployment strategy, which is a more general GPP. By changing the value of β, $(0 < \beta < 1)$, the regularity of the point process can be modified. β-GPP converges to a PPP with the same strength when $\beta \to 1$ and reverts to GPP when $\beta = 0$. Using actual data, the authors of [55] determined that altering the value of β can improve β-GPP's fit in various base station construction circumstances. The coverage probability's calculable expression is discovered. The equilibrium between the high operability of PPP and the high degree of fitting of MHCPP have been discovered.

Heterogeneous cellular networks have begun to be assessed for evaluating more complicated wireless systems. Dhillon [56] performed PPP-based modelling and obtained the downlink network performance evaluation for multi-tier heterogeneous networks. It is claimed that employing random processes to model and analyse heterogeneous networks is more meaningful, as small cells are more likely than macro-cells to gravitate toward random distribution. In this heterogeneous network, the base station position distributions for each tier are created by an independent PPP, resulting in a PPP heterogeneous network model with tier-dependent base station density, transmission power, and maximum transmission

rate. A closed-form solution of the coverage probability that mobile users can be served by BS in at least one tier was proposed.

Given that PPP cannot provide an accurate interference model in densely populated locations, the Poisson Cluster Process (PCP) was utilised to determine the base station distribution in a K-tier Heterogeneous Network (HetNet) [57]. The evaluation model implies that base stations are clustered in distinct hotspots called clusters, that each cluster contains multilayer networks, and there is no intra-cluster interference. Under this assumption, an analytical solution of the interference distribution in the system was provided, as well as a design strategy for K-tier HetNets based on the optimal performance of PCP. This theory is significantly more sensitive to spatial density than the PPP hypothesis. More HetNet tiering conditions were evaluated for practical applications in [58]. When a picocell is a supplemental service for users at the edge of the macro cell, the macro cell tiers follow the PPP, the picocell tiers follow the Poisson Hole Process (PHP), and the user distribution follows the PPP. When picocell is utilised to boost the capacity of hot areas, the macro cell tiers follow PPP, and picocells follow MHCPP. In this scenario, the user distribution similarly focuses on hot spots following the Cox process. Table 2.2 classifies these tractable wireless system evaluation approaches for better comparison.

Table 2.2 Tractable approaches of wireless system evaluation

System models for evaluation		Reference
Simplified Cellular Array Models		[47–49]
Models with stochastic geometry	Poisson Point Process (PPP)	[54]
	Ginibre Point Process (GPP)	[55]
	HetNet with PPP	[56]
	HetNet with Poisson Cluster Process (PCP)	[57]
	HetNet with Poisson Hole Process (PCP)	[58]

The methods for assessing the efficacy of wireless networks described above frequently neglect to account for blockage or only integrate it into the fading model. Besides that, these evaluation methods overlook the electromagnetic wave propagation effect of complicated spatial features such as walls and furniture. The attenuation imposed by these structures in

indoor environments can be as severe as that induced by distance. As a result, assessing the impacts of blockages on indoor wireless systems by modelling and statistics are essential.

2.1.4 Indoor LOS Probability

The largest distinction between an interior communication environment and an outdoor communication environment is its complicated spatial structure. Walls and floors easily hinder indoor communication links in wireless communication. When a Tx-Rx link has no blockage in the propagation process, it is called a LOS link. On the contrary, when walls, floors and other barriers occur in the propagation process, it is called a NLOS link. The path loss of an NLOS link differs from that of a LOS link, even if the transceiver distance is the same. The multipath effect can also induce small-scale fading. The small-scale fading of the NLOS link is commonly viewed as Rayleigh fading, while the small-scale fading of the LOS link can be regarded as Ricean fading due to the existence of an unimpeded direct channel. Hence, it is only possible to evaluate the performance of an indoor wireless system by considering whether the links in the system are LOS.

As discussed in Section 2.1.3, many evaluations of network performance based on random geometry do not account for the influence of occlusion on link performance. Nevertheless, other research has examined the impact of occlusion on performance. In [59], varying path loss exponents were utilised to calculate path loss for various sending and receiving distances while evaluating the performance of a wireless system. When the transceiver distance increases, so does the path loss exponent. This partially accounts for the impact of obstruction, as the greater the transceiver distance, the greater the likelihood that the link may be obstructed. In [60], on the basis of the LOS probability model supplied by Third Generation Partnership Project (3GPP), both LOS and NLOS components were addressed in channel modelling, and the system performance disparities under various LOS ratios were examined. Using a piecewise function to represent the link between path loss and distance and introducing an exponential-decreasing LOS probability model, researchers in [61] investigated the effect of LOS on coverage and Area Spectral Efficiency (ASE) performance of dense small cell networks. In [62], the distinction between LOS and NLOS

in small-scale fading was considered. The LOS link was characterised by Rayleigh fading, and path loss was described by the two-slope function. In order to simplify the calculation, researchers in [62] simplified the LOS probability model by considering all links within a specific transceiver distance to be LOS and all others to be NLOS. Researchers in [63] examined the impact of ultra-dense small cell networks on network performance when base stations are idle and LOS linkages are considered.

The discrepancy between LOS and NLOS should be added into the model to analyse network performance from extra dimensions, and it has gained general recognition. Nevertheless, most of these performance evaluations focus on outdoor wireless systems or ignore the variation in LOS ratio between indoor and outdoor wireless systems, preferring to employ a very simple exponential decline function to explain the LOS probability of system links. This simplistic LOS probability model will lead to deviations in performance evaluation in complicated indoor environments and may even result in facts-inconsistent performance principles. Thus, a model that accurately describes the blockages within the building and an accurate, modifiable LOS probability model based on the interior structure are required.

Since channel indicators such as path loss and small-scale fading are directly related to the blocked status of the Tx-Rx link, the statistics and calculation of LOS probability are now obligated to evaluate indoor wireless systems' performance. In [60, 61, 63], for instance, the 3GPP standard LOS probability was given as an exponentially decreasing function of transceiver distance [64]. Moreover, an outdoor LOS probability model considering building height was released in [65]. In [66], 3D LOS probability model was applied to evaluate 3D urban channels. Alas, these LOS probability distribution models are empirical models based on outside situations, making their application to indoor scenarios challenging.

Researchers in [67] proposed a LOS distribution model based on rectangular rooms. The Txs were randomly positioned within a rectangular room, and the blockage condition of the Tx-Rx link caused by the room's walls was computed at various transceiver distances. This study proposes a piecewise function for describing the LOS probability model, which can be employed to calculate the performance of wireless systems in rectangular-roomed

typical building environments. In [68], a 3D LOS probability model for ordinary multi-storey buildings was then proposed.

When addressing the effect of obstructions on propagation performance, ray tracing is a common indoor channel modelling technique [69, 70]. As stated in Section 2.1.2, ray tracing requires the input of building data and the Tx and Rx locations to judge the LOS/NLOS status of the Tx-Rx link. As a result, ray tracing is computationally intensive, which makes it hard to reach a comprehensive conclusion on the impacts of blocking on wireless performance in this manner. Consequently, randomisation has been introduced into indoor obstacle modelling. There is no requirement to provide building-specific information, and impediments are distributed randomly over the target region using a specific random process. On this premise, the statistical correlation between barriers and distance in the target region is examined to offer an operational and universally applicable barrier model. The location of the obstructions in [71] was determined using PPP, and each obstruction was modelled as a line of random length and direction. This investigation confirmed the relationship between network performance and the magnitude and density of obstructions. The model can also simulate blockages caused by buildings in dense urban areas, using Poisson Line Process (PLP) to model blockage locations. In addition, researchers in [72] modelled the blockages as a random direction and size rectangle whose central point location still follows PPP. This modelling technique is enlightening, despite the fact that the objective of these efforts is to investigate impediments imposed in outdoor scenarios.

In [73], researchers investigated the impact of various wall barriers on signal propagation in an interior environment with several transmitters. The walls were modelled as line segments based on a random geometric distribution, and the effect of wall angle and transmitter placement on the barrier was investigated. In [24], an indoor network of transmitters arranged in a typical network configuration was simulated, and the effect of wall barriers generated by various means on the system SIR was examined. This study simulated a random blockage distribution that occurs when the wall is considered a line segment. At this time, the centre coordinates of the walls adhered to PPP, while the length of the walls was random and autonomous. In the uniform model, wall orientations were uniformly random, whereas, in

binary modelling, wall orientations were either horizontally or vertically distributed. Walls can also be configured to stretch forever, replicating the relationship between walls in a physical room. At this time, the model separated the space from the horizontal and longitudinal by dividing it into a grid with infinitely long walls. The Manhattan Poisson Line Process (MPLP) can compute the horizontal and vertical wall coordinates, thereby splitting the space into irregular rectangular rooms with infinitely stretching walls. The investigation's findings indicated that the binary random wall model resulted in the poorest system performance, whereas the regular wall model produced the greatest results. These studies incorporated the blockage model into the framework for evaluating indoor wireless performance. However, since its calculation predetermines the transmitter layout, it is not relevant to a wider variety of application cases.

The base station positions in [74] were determined using the Cox point process, while the line segment consisting of obstructing structures was determined using the MPLP. This work examined the impact of blockage on a wireless system in the classic Manhattan urban model. In [75], an indoor 3D blocking model was developed, and the shadow impact of a wireless system was explained. As a multidimensional expansion of MPLP, the bottlenecks in this scenario were modelled as Poisson grids to reflect the uneven distribution of actual room volumes. This blockage modelling can also be created by deleting particular walls to replicate a more realistic room structure. Typically, the transmitters were installed against the wall or ceiling, which follows the Cox point process. This technique can compute interference fields within a building of a given size.

Table 2.3 classifies these researches studying on the impact of blockages on wireless systems for better comparison.

Researchers typically assess system performance in a known or assumed-to-be-known communication environment to optimise the evaluation system and network configuration. The constraints of architecture on indoor wireless networks' performance cannot be ignored. Nevertheless, no consideration has been given to altering the building structure in order to improve the performance of wireless systems in buildings. This is because RF engineers normally focus on the communication environment within a constructed building yet are

Table 2.3 Researches studying on the blockages

	System models for evaluation	Reference
Studies considering LOS linkages	LOS probability model in 3GPP	[60]
	LOS effect on coverage and ASE	[61]
	Simplified LOS probability in small-scale fading study	[62]
	LOS linkages in ultra-dense small cell networks	[63]
LOS probability modelling	Outdoor LOS probability models	[60, 65]
	LOS probability model for rectangular rooms	[67]
	3D LOS probability model for multi-storey buildings	[68]
Random blocking modelling	Random geometric blocking model	[73]
	Binary blocking model	[24]
	Blocking model with MPLP	[74]
	3D blocking model with Poisson grids	[75]

independent from the design optimisation of the building itself. In reality, there are numerous aspects affecting the design of a building, such as building function, surrounding environment, building materials, construction cost, etc. Suppose a set of indicators that can evaluate the impact of architecture on the wireless system are examined and weighed in the architectural design stage, in such a case, the performance of indoor wireless systems can be drastically enhanced from the ground up.

2.2 Reviews of Fundamental BWP

More revolutionary wireless systems, such as ultra-dense small cell networks and massive MIMO systems, are being launched indoors to cope with the rapid growth of indoor wireless traffic demand. However, due to the building's complicated construction, the performance of wireless systems inside the building may differ from that outside. Earlier chapters have reviewed the impact of blockage in the building structure on the indoor transceiver links and the evaluation system that considers how this factor can affect the performance of wireless systems. Such studies usually use a simple probabilistic model to simulate indoor surroundings, despite the fact that different building types ought to have distinct effects on

the same-configured wireless networks in reality. The impact of building structures on the indoor wireless system performance is defined as the BWP.

Since the building structure inevitably affects the wireless system performance, BWP should be considered in the architectural design to improve indoor wireless system performance fundamentally. Currently, many factors are influencing the design of buildings, such as materials, functions, Capital Expenditures (CAPEX), Operational Expenditure (OPEX), etc., but the impacts of wireless performance have yet to be considered. However, after the construction of a building, the wireless system designers find that no matter how the wireless system is designed and no matter how many new wireless technologies are introduced, the indoor wireless system cannot meet the explosive demand for indoor wireless traffic. This limitation is due to the fact that the architects have yet to consider the effect of the building structure on the wireless performance at the building design stage. Therefore, it is vital to model and analyse the influences of building structure on wireless system performance from various aspects and provide quantifiable analysis models. It will help architects incorporate wireless performance into the factors that need to be balanced in architectural design to enhance indoor wireless system performance from the perspective of architectural design.

At this stage, the BWP evaluation system is taking shape. Two figure of metrics (FoMs) of BWP was defined in [32], namely, the Power Gain (PG) and the Interference Gain (IG). The metrics evaluate the building structure's impact on an ultra-dense small cell cooperative network. Small cell BSs are assumed to be uniformly distributed in a high density in the scene and cooperate in sending signals to the user. The transmitting power of each BS is inversely proportional to the distribution density of the BS, i.e., the average transmitting power of each region is uniform and fixed. For an evaluated building structure, the average transmitting power $P_{\mathrm{T}} = -34\mathrm{dBWm}^2$, the threshold is set as $P_{\mathrm{th}} = -110\mathrm{dBWm}^2$. The building structure is evaluated for the wireless system in 6-GHz and 28-GHz band.

Then the sum of received signal power from all transmitters in the system by the user equipment at the specified location in the building is denoted as P_{B}, and the corresponding sum of signal power received by the user equipment at the same location in the same-sized open space is denoted as P_{O}. The quotient of the P_{B} and P_{O} is defined as the PG of the

building as

$$g_P = \frac{P_{\mathrm{B}}}{P_{\mathrm{O}}}. \tag{2.1}$$

In the same setting, the sum of the power of interference signals received by the user equipment at specified locations inside and outside the building is denoted as I_{B} and I_{O}, while the sum of the power of indoor and outdoor noise and interference can be compared to obtain IG as

$$g_I = \frac{I_{\mathrm{O}}}{I_{\mathrm{B}}}. \tag{2.2}$$

The larger the PG is, the smaller the power attenuation by the building structure in signal propagations. The larger the IG is, the more significantly the building will eliminate interference. In [32], the power attenuation by multiple walls is regarded as a wall, i.e., the link blocked by multiple walls is simplified to one-wall blockage. However, researchers in [76] faced up to this situation and proposed a more practical calculation model for IG and PG considering multi-wall blockages.

On this premise, [31] constructs a systematic BWP concept to objectively quantify the impact of building structure on specific wireless system performance characteristics. The evaluation system and indicators can be utilised to direct the building's design. In addition, [31] has proposed the potential research direction of BWP to help develop future wireless-friendly smart buildings for Sixth Generation (6G).

The state-of-art BWP evaluation is based on the assumption of extremely ultra-dense small cell networks in building design, which is too extreme and limits its applicability in real-world scenarios. At the same time, the evaluation method is user-location dependent. Each building location has a unique indicator value and is presented as a metric distribution map. However, besides the impact of wireless system performance, there are many other factors to consider in architectural design. Therefore, a more intuitive approach to define BWP metrics and evaluation scheme is needed so that architects can quickly adjust building designs by comparing differences in metrics. Such an evaluation scheme will enable architects to fully evaluate and optimise the wireless connectivity of buildings, resulting in better design and user experience.

In addition, the present BWP evaluation focuses on the indicators that affect the SINR of the system, e.g., received power and interference, as these are the most influential factors affecting the capacity of the system. In the 5G and 6G eras, however, as ever-more technologies are introduced into indoor wireless systems, an increasing number of application scenarios require indicators other than capacity, such as system delay and reliability. Moreover, new channel evaluation indicators introduced by new technologies must also be considered.

2.3 Performance Indicators of Concern

Currently, BWP evaluation focuses exclusively on the evaluation of signal received strength and interference intensity, despite the fact that there are additional indicators that can be used to characterise the performance of a communication system. This section focuses on wireless systems' unscrutinised performance indicators, RMS DS and channel hardening.

2.3.1 RMS-DS

A comprehensive description of indoor electromagnetic wave propagation is essential for evaluating indoor wireless systems. Many channel-based impulse response characteristics are studied in indoor channel measurement and modelling. However, describing the impulse response of a channel in detail is complicated, but using a specific index can replace a complete description of the impulse response of a channel to some extent, namely, the RMS-DS of the channel.

Consider a communication scenario with multipath effects, as shown in Fig. 2.2. The channel's impulse response can be represented by the power distribution diagram, as shown in Fig. 2.3, where g_i represents the power of the i-th path component, and τ_i is the time delay generated when the signal reaches Rx through this path. The difference in time delay caused by signal reaching Rx through different paths is called delay spread. RMS-DS is a parameter to quantify the delay spread. RMS-DS is the root-mean-square of the delay generated by each path and weighted by the received signal intensity of each path. Therefore, the calculation of

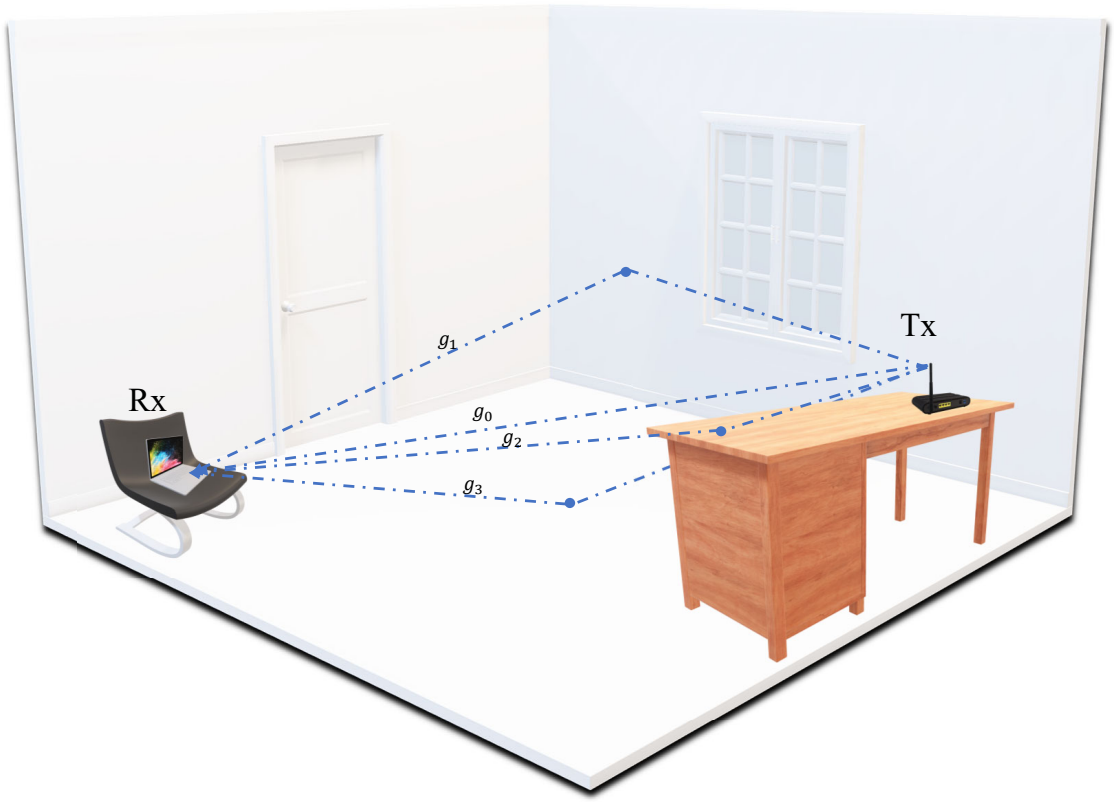

Fig. 2.2 A example of the multipath effect.

RMS-DS requires the calculation of the weighted average delay $\overline{\tau}$:

$$\overline{\tau} = \frac{\sum_i g_i \tau_i}{\sum_i g_i}. \tag{2.3}$$

RMS-DS τ_{rms} can then be expressed as:

$$\tau_{\text{rms}} = \sqrt{\frac{\sum_i g_i (\tau_i - \overline{\tau})^2}{\sum_i g_i}}. \tag{2.4}$$

In summary, RMS-DS is an indicator for evaluating the delay spread of the signal propagation path, which is calculated by measuring the delay propagation difference of the signal. Delay propagation difference refers to the difference between the propagation delay of each path in the received signal. These paths can be caused by multipath propagation,

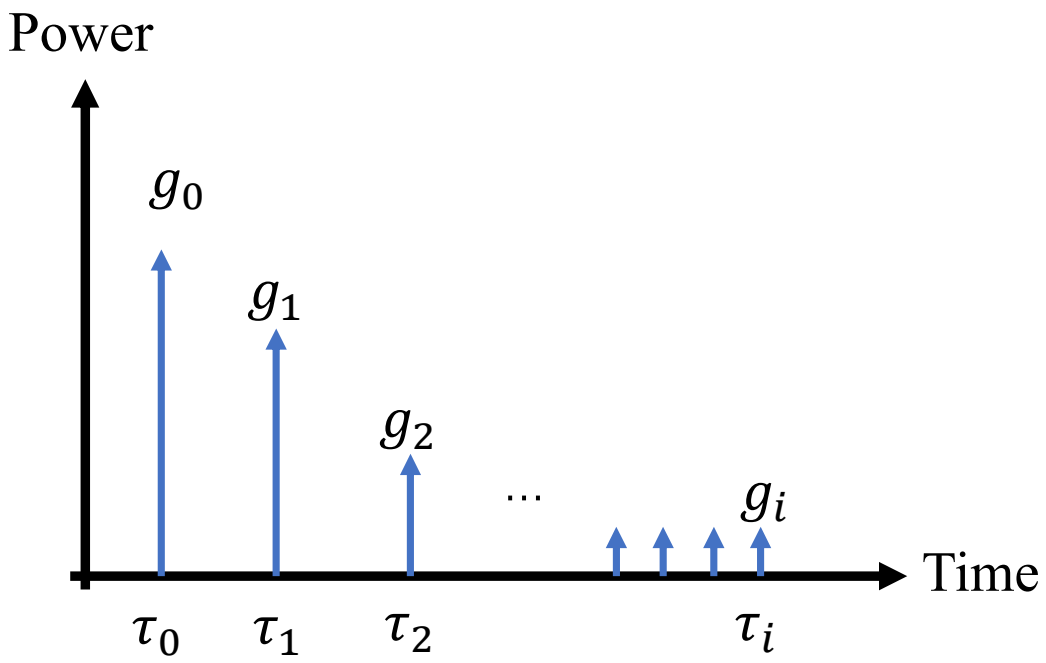

Fig. 2.3 The power delay profile of channel impulse responses describing multi-path.

in which the signal travels through a number of different paths to reach the receiver during transmission. By measuring the arrival delay of different paths, the delay spread of the signal can be analysed, and the RMS-DS value can be obtained. Therefore, signal modulation is not needed in RMS-DS measurement.

Since the signal received by Rx is the superposition of signals with different time delays through different paths, there may be interference between different symbols at this time. This interference caused by the delay spread of the multipath effect is called ISI. In order to avoid ISI, the symbol duration needs to be positively correlated with the delay extension, so the symbol rate is negatively correlated with DS. It has been proved that the performance of wireless systems with multipath effects is susceptible to RMS-DS [25, 26]. Studies in [27, 28] demonstrated that the maximum transmission data rate in an indoor wireless system is linearly dependent on τ_{rms}^{-1}.

In addition, RMS-DS directly affects the channel's coherence bandwidth in the frequency domain. When the coherence bandwidth B_C of the channel is greater than the signal bandwidth B_S, the signal will not be distorted in the frequency domain after transmission. However, when the coherence bandwidth of the channel is too narrow, i.e., $B_C < B_S$, the received signal via the channel will selectively fade in the frequency domain, that is, distortion. The coherence bandwidth for a healthy channel is linear to the τ_{rms}^{-1} of the channel.

The ISI in the time domain and the frequency selective distortion in the frequency domain are two aspects of the relationship, both becoming serious with the increase of RMS-DS. If the influence of RMS-DS is not considered in signal transmission, the reliability of the communication system will be seriously affected. Considering the effect of RMS-DS, the signal bandwidth needs to be reduced, which affects the system capacity. Therefore, the RMS-DS of wireless systems must be addressed considering the system capacity and reliability.

In OFDM systems, delay spread also introduces challenges. OFDM relies on frequency-domain equalization to compensate for frequency-selective fading caused by multipath channels. However, delay spread results in time variations of the multipath channel frequency response, requiring more frequent equalization updates to maintain the desired performance. This can increase computational complexity and introduce additional overhead in the system. Moreover, delay spread may cause overlapping of multipath replicas with neighbouring OFDM frames, resulting in inter-frame interference. This requires additional interference mitigation techniques at the receiver to mitigate the effects of inter-frame interference, potentially impacting system reliability [77].

A large number of measurements demonstrate that RMS-DS is correlated with transceiver distance d and path loss. In [78], researchers measured the RMS-DS of the stairwell scenario in the frequency band of 5 GHz but did not obtain the relationship between RMS-DS and distance. In [79], researchers measured the RMS-DS of Ultra Wide Band (UWB) indoor channels in office buildings. The relationship between RMS-DS and frequency was analysed by comparing the differences between RMS-DS in $54-59$ GHz and $61-64$ GHz. In [80], RMS-DS of LOS links were measured in three buildings and found to be positively correlated

with distance. In [81], after analysing the transmission data collected in two office buildings, the researchers discovered that RMS-DS was highly correlated with both transceiver distance and path loss.

The multipath effect of different sending and receiving locations will lead to the randomness of the RMS-DS, which is ignored in the above study. The researchers argued in [34] that RMS-DS should be described as a random variable related to transceiver distance and path loss. RMS-DS can be expressed as:

$$\tau_{\text{rms}} = kL(d) + B + X_{\text{z}}, \tag{2.5}$$

where X_{z} is a normally distributed random variable with the mean value $\mu = 0$ and standard deviation σ. $L(d)$ is the path loss which can be described as:

$$L(d) = L(d_0) + 10n\log_{10}(d/d_0) + C + X_{\text{s}}, \tag{2.6}$$

where $L(d_0)$ is the reference path loss in decibel ($d_0 = 1$ m), X_{s} is a normally distributed random variable with the mean value $\mu = 0$ and standard deviation σ_{s}. Values of parameters k, B, σ, n, C and σ_{s} vary according to the propagation environment, such as blockage conditions and room types. In [34], researchers tested LOS and NLOS links in offices, corridors and stairwells at 2.595 GHz, and fitted parameter values of k, B, σ, n, C and σ_{s} at different propagation environments.

2.3.2 Channel Hardening Ratio

Massive MIMO has been introduced into indoor wireless communication systems as a key 5G technology. In [82], researchers studied indoor channel simulation modelling based on the ray launching of massive MIMO and presented a statistical model for convenient calculation. In [83], three indoor massive MIMO systems with different cooperation levels were simulated to investigate the effect of massive MIMO suppression of inter-cell interference on system capacity enhancement under different cooperation modes. In [29], the millimetre wave

(mmWave) and massive MIMO were combined to achieve greater system capacity and higher transmission rates. The indoor massive MIMO channels with 64-array and 128-array at 26ghz were characterised. Similarly, the throughput of massive MIMO systems using Hybrid Beamforming (HBF) algorithms at 38 GHz and 65 GHz was experimentally tested in [84]. In [85–87], researchers proposed to combine the network cooperation principle of cell-free MIMO with Massive MIMO to improve the fairness of regional user data rates.

These studies simplify the precoding strategy due to the channel hardening phenomenon specific to massive MIMO. However, in practice, the channel hardening is not completed. Study [88] proved that both antenna numbers and density would affect the channel hardening effect. Researchers in [89] proposed the channel hardening indicator: the channel hardening ratio. Further, researchers in [89] demonstrated that once the degree of channel hardening is inadequate, the massive MIMO system's stability degrades. As a result, in the channel evaluation of massive MIMO systems, the degreeof channel hardening should be defined and calculated. Study in [90] proposed a basic mathematical model of channel hardening ratio in different propagation environments.

When evaluating channel hardening, the researchers in [87, 89] simply assumed the channel as a space-independent Rayleigh fading channel. However, the spatial correlation of antennas in the massive MIMO system cannot be ignored [91]. In addition, Rayleigh fading channels cannot accurately describe communication links in short-range propagation due to the presence of LOS components. [30] gives a comprehensive channel hardening model considering the spatial correlation of the antenna and the LOS component when the link is not blocked, as shown below.

When a base station consisting of a $M \times 1$ Uniform Linear Array (ULA) transmits signals to a single-antenna user, the channel vector is represented by $\mathbf{h}$, which can be expressed as:

$$\mathbf{h} = \beta \left[1, e^{j\pi\sin\phi}, ..., e^{j(M-1)\pi\sin\phi}\right]^T, \tag{2.7}$$

where ϕ is the Angle of Arrival (AOA) of the antenna and β is the large-scale propagation losses of the evaluated Tx-Rx link.

For a channel, the channel is considered hardened when:

$$\frac{\mathrm{Var}\{\|\mathbf{h}\|^2\}}{\mathrm{E}\{\|\mathbf{h}\|^2\}^2} \to 0, \text{ as } M \to \infty. \tag{2.8}$$

Normally, the number of antennas M is finite, so this incomplete channel hardening can be measured by the channel hardening ratio:

$$\xi = \frac{\mathrm{Var}\{\|\mathbf{h}\|^2\}}{\mathrm{E}\{\|\mathbf{h}\|^2\}^2}. \tag{2.9}$$

When the channel hardening ratio is high, the channel hardening is damaged and the system reliability is threatened.

When considering the spatial correlation of antennas, $\mathbf{R}$ as a positive semi-definite matrix is used to describe the spatial correlation between different antennas, the closer the antennas are, the stronger the spatial correlation is. And $\mathbf{R}$ follows $\mathrm{Tr}(\mathbf{R}) = M$ [92].

The channel is considered as a Ricean fading channel when the Tx-Rx path is LOS. The Ricean fading can be considered as adding the LOS component to the Rayleigh fading component of a NLOS link. K-factor is a parameter for describing the proportion of LOS component in the Ricean fading channel.

Therefore, according to [30], for a perfect Channel State Information (CSI) case, when spatial correlation and Ricean fading channel are considered, the channel hardening ratio can be expressed as:

$$\xi = \frac{2K\bar{\mathbf{h}}^{\mathrm{H}}\mathbf{R}\bar{\mathbf{h}} + \mathbf{Tr}(\mathbf{R}^2)}{M^2(1+K)^2}, \tag{2.10}$$

where $\bar{\mathbf{h}}$ is the normalised channel vector, expressed as:

$$\bar{\mathbf{h}} = \left[1, e^{j\pi\sin\phi}, ..., e^{j(M-1)\pi\sin\phi}\right]^T. \tag{2.11}$$

2.4 Research Challenges

Establishing a BWP evaluation system is very important for improving indoor wireless performance. The current BWP metrics IG and PG have been proposed to evaluate the impact of building structure on indoor wireless system capacity. However, there are still some challenges in current BWP research.

First, for facilitating architects to weigh and optimise building designs in multiple dimensions, including but not limited to wireless network performance, BWP evaluation metrics should be more intuitive. It is necessary to describe the impact of the whole building design on one wireless performance indicator with one BWP metric. The current BWP metrics are still receiver location dependent, while a BWP evaluation system independent of receiver and transmitter locations needs to be established.

Second, the current BWP evaluation is limited to two wireless performance indicators: interference and received signal power. In contrast, more indicators are left to be considered in a bid to help improve the capacity and reliability of wireless systems. In the evaluation, the influence of the building structure on different indicators also needs to be carefully discussed.

Third, the desired BWP evaluation system should have high scalability to adapt to more new indicators being included in the BWP evaluation. On this basis, computational complexity should be limited to achievable conditions.

The building structure significantly influences the channel multipath effect, including signal reflection and diffraction. These effects will lead to signal strength fading, inter-symbol interference (ISI), delay expansion and other problems, thus affecting the capacity and stability of wireless systems. Multipath effects affect the capacity and stability of wireless systems, so it is essential to evaluate the impact of architecture on multipath effects. In order to evaluate the multipath effect, it is necessary to select a suitable performance indicator to measure its impact degree. General wireless performance indicators that can assess the multi-path effect are delay spread, coherence time, Rician K-factor, Doppler spread and error vector magnitude. Table 2.4 lists these performance indicators and there descriptions.

Delay spread is often considered as a good starting point due to its direct relevance to signal dispersion and coherence bandwidth. Moreover, delay spread is relatively easy to

Table 2.4 Performance indicators describing the multi-path effect

Performance Indicator	Description
Delay Spread	Measuring the spread or difference in arrival times of multipath components
Coherence Time	Representing the duration over which a channel remains relatively unchanged
Rician K-factor	Quantifying the strength of the LOS component relative to scattered multipath
Doppler Spread	Measuring the spread or difference in Doppler frequencies of multipath components
Channel Capacity	Representing the maximum data rate that can be reliably transmitted over a given channel
Error Vector Magnitude	Quantifying the distortion and deviation of the received signal from the ideal signal

measure and interpret compared to other indicators, making it a practical choice for channel characterisation.

In massive MIMO systems, the channel hardening can reflect the multipath effects. Channel hardening refers to the phenomenon where the time variation of the channel response is reduced. When multipath effects are weak, i.e., when there are fewer paths, and their strength is low, the channel response remains relatively stable without frequent changes. In this case, the channel is considered to be hardened. Conversely, when multipath effects are strong, i.e., when there are multiple paths with significant strength, the channel response undergoes frequent changes, leading to significant variations in the time-domain and frequency-domain characteristics of the signal. In this case, the channel is considered to be softened. Therefore, as a performance indicator to measure the channel hardening effect, the channel hardening ratio is worth studying in the BWP evaluation of massive MIMO systems.

Chapter 3

Wireless Channel Delay Spread Performance Evaluation of a Building Layout

Overview

A new approach for wireless communications in building design is proposed for evaluating a building's wireless performance throughout the building design stage. The earliest BWP evaluation theory, concentrating on the DS channel, is proposed in this chapter. The following are the novel contributions of this chapter. 1) The first metric for assessing the channel DS performance of a building under design is defined, named DS gap. 2) To rapidly and precisely calculate the metric, an analytical model is derived. 3) Monte-Carlo simulations performed in typical interior environments are used to validate the proposed scheme. According to numerical results, the RMS-DS are clearly impacted by building design. In the future, architects should carefully consider a building's DS gap during the building design process. Otherwise, because of an excessively high DS gap, wireless systems within it will experience severe ISI.

3.1 Introduction

3.1.1 Background and Motivations

The BWP has to be considered in the building design process [31–33, 76]. The performance of the densely deployed indoor wireless devices is upper bounded by the building design regardless of specific network deployment and configuration. With the evolution of wireless reliability-dependent use case scenarios such as augmented reality, virtual reality, smart building, smart factories, etc.[93–96], the wireless performance demand, e.g., throughput, latency, and reliability, increases continuously and will eventually hit the upper bound.

Currently, RF engineers improve the performance of indoor wireless systems by optimising their deployment. Since the performance of an indoor wireless communication network is upper-bounded by the building itself, in some cases, RF engineers find that no matter how they deploy the wireless network, the indoor wireless system cannot meet the performance requirements for indoor wireless services. Therefore, costly and time-consuming building retrofits may become a last resort to meet wireless performance requirements in these scenarios. As a result, BWP metrics, which can assist architects in avoiding employing room layouts with bad wireless performance, are essential in the building design stages.

The BWP evaluation must take DS as a crucial channel indicator into account. As the delay spread increases, the multipath signals arrive at the receiver with larger time differences, causing them to interfere with the current symbol being received. This interference leads to higher levels of ISI and an increased probability of symbol errors. A larger delay spread can also result in stronger constructive or destructive interference between the multipath signals. This increased interference power within the channel leads to higher interference, potentially degrading the system's performance. In turn, ISI and interference caused by delay spread can increase the BER by distorting and overlapping symbols, making it difficult for the receiver to detect and decode the transmitted information accurately [97, 98].

A strong ISI could happen if a building is poorly designed, considering its impact on channel DS, and leading to a narrower coherence bandwidth [99–101]. Poor building design can decrease the reliability of indoor wireless networks and lower the upper bound of

indoor transmitted signal bandwidth because selective fading in the channel occurs when the transmitted signal bandwidth is wider than the coherence bandwidth [102, 103]. On the other hand, the broader the coherence bandwidth is, the more accurate the channel estimation in the wider frequency band and the easier the pilot design is. As a result, the building's inner layout will also affect the complexity and effectiveness of the pilot design [104].

However, how to evaluate BWP considering channel DS is still unknown. Most existing studies on channel DS lie in the perspective of channel modelling rather than BWP evaluation [78–81, 34, 105–111]. Whereas in the field of BWP, the impact of building layout on channel DS has never been considered before [31, 32, 76]. In [79, 80, 107–110], the RMS-DS of indoor channels was measured and modelled in the Ultra-High Frequency (UHF) band, UWB and visible light communication system. In [78, 34, 107, 111], multiple room configurations, including offices, corridors, and staircases, were adopted for RMS-DS modelling. The results demonstrated that RMS-DS modelling in various propagation environments frequently exhibits similar patterns: the RMS-DS of a link presents a linear correlation with the path loss. Specifically, according to [79, 34, 106, 111, 108], RMS-DS in indoor scenarios has a stronger association with distance, or, more precisely, with path loss than they do in outdoor environments. Particularly, the results of [34] demonstrate that indoor scenarios with a variety of room types and LOS or NLOS conditions can exhibit a wide variety of probability density distributions of the RMS-DS. Nevertheless, how to avoid strong DS when designing buildings has never been considered, which could make the building a bottleneck limiting the performance of 5G and 6G reliability-demand services.

3.1.2 Contributions in This Chapter

To bridge the gap between the BWP evaluation and channel DS modelling, this chapter proposes the earliest systematic BWP evaluation approach dedicated to RMS-DS. More specifically, this chapter defines a metric, namely DS gap, to capture the impact of a building on the RMS-DS of wireless connections in it. Then, this chapter proposes an analytical model of the RMS-DS to facilitate quick DS gap evaluation given a building layout.

3.2 Definition of Metric to Evaluate Building Channel DS Performance

We define the metric, the DS gap G_τ, to evaluate the building wireless performance for RMS-DS:

$$G_\tau = \mathrm{E}[\tau_\mathrm{I}] - \mathrm{E}[\tau_\mathrm{O}], \tag{3.1}$$

where τ_I and τ_O are the realisation of random variable RMS-DS in indoor and in open space environments, and $\mathrm{E}[\tau_\mathrm{I}]$ denotes the expectation value of RMS-DS for the assessed indoor environment in the distance and time domain, and $\mathrm{E}[\tau_\mathrm{O}]$ denotes the expectation of RMS-DS for an open space with the same occupied area in the distance domain. The indicator G_τ represents a building's inherent wireless performance characteristic. It indicates the effective varying in RMS-DS levels when the network covers a building as opposed to open space. Physically, more complicated building structures result in more severe multi-path effects, leading to greater RMS-DS and ISI, and finally results in narrower coherence bandwidth.

According to measurements in [79, 80, 107–110], τ_I is a random variable in any given indoor scenario, and the distribution of RMS-DS for a specific link depends on the distance between the Tx and the Rx, denoted by d. Therefore, $\mathrm{E}[\tau_\mathrm{I}]$ must be found with the given Probability Density Function (PDF) of τ and d, as:

$$\mathrm{E}[\tau_\mathrm{I}] = \int_0^{+\infty} \tau_\mathrm{I} \int_0^{+\infty} f(\tau_\mathrm{I}|d) p_{\iota,\chi}(d) \mathrm{d}d \mathrm{d}\tau_\mathrm{I}, \tag{3.2}$$

where $f(\tau_\mathrm{I}|d)$ denotes the indoor RMS-DS distribution function that varies with d, ι denotes the event that Tx is in the BUD, and χ denotes the event that Rx is in the BUD, and $p_{\iota,\chi}(d)$ denotes the PDF of the distance between Tx and Rx when they randomly locate in the BUD. As a contrast, given the same area compared with the indoor scenario, τ_O as the RMS-DS value in the open space, only depends on d, i.e., given a definite d, the value of τ_O is determined. As the result, $\mathrm{E}[\tau_\mathrm{O}]$ can be found with the given PDF of d, as:

$$\mathrm{E}[\tau_\mathrm{O}] = \int_0^{+\infty} \tau_\mathrm{O}(d) p_{\iota,\chi}(d) \mathrm{d}d, \tag{3.3}$$

where $\tau_{\mathrm{O}}(d)$ denotes the open-space RMS-DS function of d.

Moreover, whether the transmission is LOS or NLOS impacts the distribution of RMS-DS substantially in an indoor environment. Measurement results also show that different room types, e.g., offices and corridors lead to different distributions of RMS-DS [34]. Therefore, the distribution of τ_{I} depends on i) the distribution of the transmission condition between Tx and Rx, in terms of the blockage effect and the room type, ii) the distribution of Tx-Rx distance d, and iii) the distribution of RMS-DS for a link given d and definite transmission conditions. Similarly, the distribution of τ_{O} depends on i) the distribution of Tx-Rx distance d, and ii) the RMS-DS in open space for a link given d.

To decouple the intrinsic property of the building and the specific deployment of indoor wireless devices, we need to assume that the Txs and the Rxs are randomly deployed in the building under consideration in the building design stage. Under this situation, d is a random variable, too.

In a complex building environment, G_τ needs to be quantified in the building design stage, considering both the random position of transceivers and the blockage effect.

3.3 Analytical Model of the DS gap

To quickly and accurately compute the DS gap, in this section, the detailed procedure for deriving G_τ is provided, and the final analytic expression of G_τ is given. Table 3.1 describes the main notations that appear in this chapter.

$\mathrm{E}[\tau_{\mathrm{I}}]$ and $\mathrm{E}[\tau_{\mathrm{O}}]$ are derived in the following subsections III-A and III-B.

3.3.1 Derivation of $\mathrm{E}[\tau_{\mathrm{I}}]$

Within a BUD, $f(\tau_{\mathrm{I}}|d)$ can be calculated as:

$$f(\tau_{\mathrm{I}}|d) = \int_{\mathbf{r}} \sum_{\kappa} \sum_{\upsilon} f_{\tau_{\mathrm{I}},\chi|d,\kappa,\upsilon,\mathbf{r}_{\mathrm{T}}}(\tau_{\mathrm{I}}) \mathscr{P}(\upsilon) \mathscr{P}(\kappa|d) g_{\mathbf{r}_{\mathrm{T}}}(\mathbf{r}) \mathrm{d}\mathbf{r}, \tag{3.4}$$

Table 3.1 Notation definition for Chapter 3

Notation	Description
G_τ	DS gap
τ	RMS-DS
τ_{I}	Instantaneous value of RMS-DS indoors
τ_{O}	Instantaneous value of RMS-DS in the open space
d	Distance between Tx and Rx
$f(\tau_{\mathrm{I}})$	Indoor RMS-DS distribution function that varies with d
$\mathscr{P}$	Probability of an event
p	PDF of d
ι	The event that the TX is in the BUD
χ	The event that the Rx is in the BUD
κ	The set of blockage situation
υ	The set of room types that Tx is located
$g_{\mathbf{r}_{\mathrm{T}}}$	PDF of Tx locating at a position
r_{A}	Aspect ratio
$\mathbf{r}$	The coordinates
N_{r}	The amount of rooms in the BUD
S	The size of a room
n	The room number of a room in the BUD
V	The size of the BUD
m	The long edge of a room
l	The short edge of a room
X	The long edge of the BUD
Y	The short edge of the BUD
$\mathscr{C}$	The set of coordinates
$L_{\kappa,\upsilon}$	Path loss of indoor transmission with definite transmission conditions
μ	Expectation
$\mu_{\kappa_n,\upsilon,\tau}$	Expectation value of RMS-DS indoors with definite transmission conditions
$G_{\tau,\mathrm{sim}}$	The simulation result of G_τ
$G_{\tau,\mathrm{ana}}$	The analytic result of G_τ
σ	The reliability of the model

where $\mathscr{P}(\cdot)$ denotes the probability of an event, $\kappa \in \{\text{LOS}, \text{NLOS}\}$ denotes the blockage effect, $\upsilon \in \{\text{office}, \text{hall}, \text{corridor}, \text{staircase}, ...\}$ denotes the type of the room where the Tx locates, $\mathbf{r}_\text{T} = (x_\text{T}, y_\text{T})$ denotes the position of the Tx whose PDF is $g_{\mathbf{r}_\text{T}}(\mathbf{r})$, $f_{\tau_\text{I},\chi|d,\kappa,\upsilon,\mathbf{r}_\text{T}}(\tau_\text{I})$ is the PDF of RMS-DS with given scenario υ and blockage condition κ. Since $f_{\tau_\text{I},\chi|d,\kappa,\upsilon,\mathbf{r}_\text{T}}(\tau_\text{I})$ denotes the PDF of τ, it requires specific distribution assumptions of τ to be further determined. Given that the BUD is composed of N_r rooms, and the n-th room is with type υ_n and an area of S_n. Then the total area of the entire building is calculated by

$$V = \sum_{n=1}^{N_\text{r}} S_n. \tag{3.5}$$

Then $\text{E}[\tau_\text{I}]$ can be calculated as

$$\begin{aligned}\text{E}[\tau_\text{I}] = &\int_0^{+\infty} \tau_\text{I} \sum_{n=1}^{N_\text{r}} \int_0^{+\infty} p_{\iota,\chi}(d) \\ &\int_{\mathbf{r}} \sum_{\kappa} \sum_{\upsilon} f_{\tau_\text{I},\chi|d,\kappa,\upsilon_n,\mathbf{r}_\text{T}}(\tau) \mathscr{P}_\upsilon(\mathbf{r}_\text{T}) \mathscr{P}_{\upsilon_n,d}(\kappa|\chi) g_{\mathbf{r}_\text{T}|\upsilon_n}(\mathbf{r}) \mathscr{P}(\upsilon_n) \text{d}\mathbf{r}\text{d}d\text{d}\tau_\text{I}.\end{aligned} \tag{3.6}$$

The aim of this section is to provide an analytical evaluation of the DS gap for a BUD. To facilitate the derivation, we make the following assumptions.

- All rooms in the BUD are assumed to be rectangular. The size of the n-th room S_n can be calculated by $m_n \times l_n$, where m_n denotes the long edge and l_n denotes the short edge of the n-th room. The BUD is assumed to be rectangular as well, with a size of $X \times Y$, where X denotes the long edge of the BUD, and Y denotes its short edge. We set the coordinate system on BUD, with origin at the left bottom. With this assumption, V can be expressed as:

$$V = \sum_{n=1}^{N_\text{r}} S_n = XY. \tag{3.7}$$

- Both the Tx and the Rx are assumed to be distributed in the BUD uniformly with heights h_{T} and h_{R}. Therefore,

$$g_{\mathbf{r}_{\mathrm{T}}}(\mathbf{r}) = \begin{cases} \frac{1}{V} & \mathbf{r}_{\mathrm{T}} \in \mathscr{C}_{\mathrm{B}}, \\ 0, & \text{else}, \end{cases} \tag{3.8}$$

and

$$\mathscr{P}(\upsilon_n) = \frac{S_n}{V}, \tag{3.9}$$

where $\mathscr{C}_{\mathrm{B}}$ is defined as the set of coordinates occupied by the BUD. Similarly, we define the set of coordinates occupied by the n-th room as $\mathscr{C}_n$. Therefore, the conditional PDF of $\mathbf{r}_{\mathrm{T}}$ when Tx is located in the n-th room is defined as $g_{\mathbf{r}_{\mathrm{T}}|\upsilon_n}(\mathbf{r})$:

$$g_{\mathbf{r}_{\mathrm{T}}|\upsilon_n}(\mathbf{r}) = \begin{cases} \frac{1}{S_n} & \mathbf{r}_{\mathrm{T}} \in \mathscr{C}_n, \\ 0, & \text{else}. \end{cases} \tag{3.10}$$

- We assume that two possible types of rooms, which are offices and corridors, consist of the BUD, i.e., $\upsilon = \{\text{office}, \text{corridor}\}$. We define the sum size of offices as S_{offi} and corridors as S_{corr}, and define the set of coordinates occupied by the offices as $\mathscr{C}_{\text{offi}}$ and the corridors as $\mathscr{C}_{\text{corr}}$. Therefore,

$$\mathscr{P}_{\upsilon}(\mathbf{r}_{\mathrm{T}}) = \begin{cases} \frac{S_{\text{offi}}}{V} & \mathbf{r}_{\mathrm{T}} \in \mathscr{C}_{\text{offi}}, \\ \frac{S_{\text{corr}}}{V} & \mathbf{r}_{\mathrm{T}} \in \mathscr{C}_{\text{corr}}, \\ 0 & \text{else} \end{cases} \tag{3.11}$$

- We assume that RMS-DS has a linear relationship with path loss in indoor environments according to measurement results in [34]. Therefore, in this study, the communication environment of the rooms in the evaluated building is assumed to be consistent with

the empirical model in [34]. More specifically, RMS-DS can be expressed as follows:

$$\tau_{\kappa,\upsilon,d,\mathrm{I}} = k_{\kappa,\upsilon} L_{\kappa,\upsilon,\mathrm{I}}(d) + B_{\kappa,\upsilon} + X_{\kappa,\upsilon,\mathrm{z}}, \tag{3.12}$$

where $X_{\kappa,\upsilon,\mathrm{z}}$ is a normally distributed random variable with the mean value $\mu_{\kappa,\upsilon} = 0$ and standard deviation $\sigma_{\kappa,\upsilon}$. $L_{\kappa,\upsilon,\mathrm{I}}(d)$ is the path loss which can be described as:

$$L_{\kappa,\upsilon,\mathrm{I}}(d)[\mathrm{dB}] = L(d_0) + 10\alpha_{\kappa,\upsilon}\log_{10}(d/d_0) + C_{\kappa,\upsilon} + X_{\kappa,\upsilon,s}, \tag{3.13}$$

where $L(d_0)$ is the reference path loss in decibel ($d_0 = 1$ m and the test band is centred at 2.595 GHz), which is 40.7 dB according to [34]. $X_{\kappa,\upsilon,s}$ is a normally distributed random variable with the mean value $\mu_{\kappa,\upsilon,s} = 0$ and standard deviation $\sigma_{\kappa,\upsilon,s}$. Values of parameters $k_{\kappa,\upsilon}$, $B_{\kappa,\upsilon}$, $\sigma_{\kappa,\upsilon}$, $\alpha_{\kappa,\upsilon}$, $C_{\kappa,\upsilon}$ and $\sigma_{\kappa,\upsilon,s}$ vary according to the κ and υ. In this chapter, to validate the RMS-DS expectation model, the parameter values for different κ and υ in [34] are employed, as shown in Table 3.2. The model suggested in this chapter is still valid for the room types not mentioned, as long as the necessary experimental data is supplied. In addition, in this chapter, the RMS-DS in open space is calculated using a two-ray model.

Table 3.2 Parameters of the RMS-DS model

υ	κ	k	B	σ	α	C	σ_s
Office	LOS	0.40	-3.43	2.34	2.55	0.37	3.76
	NLOS	0.40	-4.77	3.30	2.40	10.73	3.62
Corridor	LOS	0.38	-5.72	2.40	1.81	0.32	2.69
	NLOS	0.39	-8.04	2.97	1.82	5.56	2.73

By combining Eqs. (3.12) and (3.13), for Tx locating at the n-th room, the RMS-DS of the indoor channel can be represented as a normal distributed random variable with the expectation value:

$$\mu_{\kappa,\upsilon_n,\tau_\mathrm{I}}(d) = k_{\kappa,\upsilon_n} L(d_0) + 10k_{\kappa,\upsilon_n}\alpha_{\kappa,\upsilon_n}\log_{10}(d/d_0) + k_{\kappa,\upsilon_n} C_{\kappa,\upsilon_n} + B_{\kappa,\upsilon_n}, \tag{3.14}$$

and the standard deviation:

$$\sigma_{\kappa,\upsilon_n,\tau_\mathrm{I}} = \sqrt{\sigma^2_{\kappa,\upsilon_n} + k^2_{\kappa,\upsilon_n}\sigma^2_{\kappa,\upsilon_n,s}}. \tag{3.15}$$

Therefore, $f_{\tau_\mathrm{I},\chi|d,\kappa,\upsilon_n,\mathbf{r}_\mathrm{T}}(\tau_\mathrm{I})$ is given by

$$f_{\tau_\mathrm{I},\chi|d,\kappa,\upsilon_n,\mathbf{r}_\mathrm{T}}(\tau_\mathrm{I}) = \frac{\exp\left(-\frac{1}{2}\left(\frac{\tau_\mathrm{I}-\mu_{\kappa_n,\upsilon,\tau_\mathrm{I}}(d)}{\sigma_{\kappa_n,\upsilon,\tau_\mathrm{I}}}\right)^2\right)}{\sqrt{2\pi}\sigma_{\kappa_n,\upsilon,\tau_\mathrm{I}}} \tag{3.16}$$

under this assumption.

From (3.6), we can see that with given (3.9), (3.10), (3.11), and (3.16), as long as we have the analytical expression of $\mathscr{P}_{\upsilon_n,d}(\kappa|\chi)$ and $p_{\iota,\chi}(d)$, $\mathrm{E}[\tau_\mathrm{I}]$ can be derived analytically. $\mathscr{P}_{\upsilon_n,d}(\kappa|\chi)$ and $p_{\iota,\chi}(d)$ are given by the following Lemma 1 and Lemma 2, respectively.

Lemma 1.

$$\mathscr{P}_{\upsilon_n,d}(\kappa|\chi) = \begin{cases} \frac{Z(d,l_n,m_n)}{Z(d,Y,X)}, & \text{LOS}, \\ 1-\frac{Z(d,l_n,m_n)}{Z(d,Y,X)}, & \text{NLOS}, \end{cases} \tag{3.17}$$

where $Z(d,a,b),(a<b)$ is defined as

$$Z(d,a,b) = \begin{cases} \frac{d^2-2d(a+b)+ab\pi}{ab\pi}, & 0<d\le a, \\ \frac{-a^2+2db(\sqrt{1-\frac{l^2}{d^2}}-1)+2ab\arcsin\frac{a}{d}}{ab\pi}, & a<d\le b, \\ -\frac{d^2+a^2+b^2-2d(b\sqrt{1-\frac{a^2}{d^2}}+a\sqrt{1-\frac{b^2}{d^2}})+2ab(\arccos\frac{a}{d}+\arccos\frac{b}{d}-\frac{\pi}{2})}{ab\pi}, & b<d\le\sqrt{a^2+b^2}, \\ 0, & \sqrt{a^2+b^2}<d. \end{cases} \tag{3.18}$$

Proof. The function $Z(d,a,b)$ is defined for: In the promise that a point A is in a rectangle with the size $a\times b,(a<b)$, the probability that a point B at a distance d from the point A is also in the rectangle is calculated by $Z(d,a,b)$ [67, Eq. (3)].

Referring the function $Z(d,a,b)$, we define that when Tx is in the n-th room and the Tx-Rx distance is d, the probability that the Tx-Rx link is LOS is $\mathscr{P}_{\upsilon_n,d}(\mathrm{LOS})$. Similarly,

$\mathscr{P}_{\upsilon_n,d}(\chi)$ denotes the probability that Rx is located in the BUD when Tx is in the n-th room, and the distance between Tx and RX is d. According to the definition of $Z(d,a,b)$, we can derive:

$$\mathscr{P}_{\upsilon_n,d}(\mathrm{LOS}) = Z(d,l_n,m_n), \tag{3.19}$$

and

$$\mathscr{P}_{\upsilon_n,d}(\chi) = Z(d,Y,X), \tag{3.20}$$

When the Tx-Rx link is LOS and Tx is located in BUD, then Rx is always located in BUD. Therefore, we can derive:

$$\begin{aligned}\mathscr{P}_{\upsilon_n,d}(\mathrm{LOS}|\chi) &= \frac{\mathscr{P}_{\upsilon_n,d}(\mathrm{LOS},\chi)}{\mathscr{P}_{\upsilon_n|d}(\chi)} \\ &= \frac{\mathscr{P}_{\upsilon_n,d}(\mathrm{LOS})}{\mathscr{P}_{\upsilon_n|d}(\chi)} \\ &= \frac{Z(d,l_n,m_n)}{Z(d,Y,X)},\end{aligned} \tag{3.21}$$

and therefore

$$\begin{aligned}\mathscr{P}_{\upsilon_n,d}(\mathrm{NLOS}|\chi) &= 1-\mathscr{P}_{\upsilon_n,\chi}(\mathrm{LOS}|\chi) \\ &= 1-\frac{Z(d,l_n,m_n)}{Z(d,Y,X)}.\end{aligned} \tag{3.22}$$

□

Lemma 2.

$$p_{\iota,\chi}(d) = \frac{2\pi d Z(d,Y,X)}{XY}, \tag{3.23}$$

where $Z(d)$ is defined as (3.18) as well.

Proof. As Fig. 3.1 shows, for Tx locating at $\mathbf{r}_\mathrm{T}$ in the building, all possible positions of receiver Rx which is d far from Tx, can form a circle with the centre of $\mathbf{r}_\mathrm{T} = (x_\mathrm{T}, y_\mathrm{T})$ and

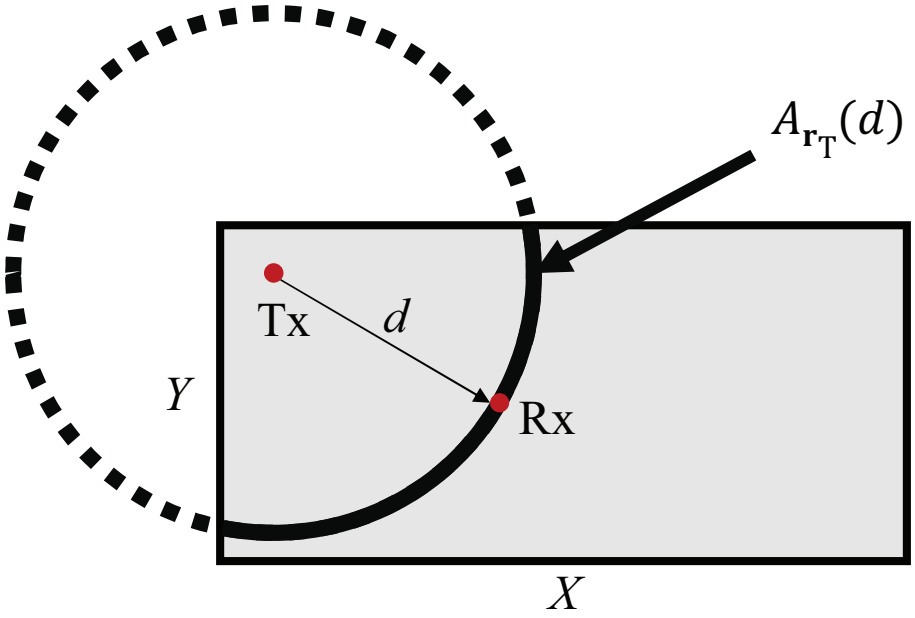

Fig. 3.1 For a transmitter Tx at any position in the building, when the distance between it and the receiver Rx is d, Rx is located on an arc of radius d with Tx as the centre of the circle.

radius of d, whose circumference is $2\pi d$. Rx that locates on the arc of the circle in the building can communicate with Tx in LOS condition. We define the length of the arc inside the building as $A_{\mathbf{r}_T}(d)$. Under this premise, when Rx is randomly located at any position in an infinitely extended plane, the probability that it locates on $A_{\mathbf{r}_T}(d)$ is defined as $\mathscr{P}_{\text{arc},\mathbf{r}_T}(d)$. Similarly, we define the probability that an Rx locates in the BUD as $\mathscr{P}_{\chi,\mathbf{r}_T}(d)$.

Therefore, for any Rx in the building, the probability that its distance from Tx locating at $\mathbf{r}_T$ is d can be defined as $\mathscr{P}_{\mathbf{r}_T}(d|\chi)$, which can be calculated as:

$$\begin{aligned}\mathscr{P}_{\mathbf{r}_T}(d|\chi) &= \frac{\mathscr{P}_{\text{arc},\mathbf{r}_T}(d)}{\mathscr{P}_{\chi,\mathbf{r}_T}(d)} \\ &= \frac{A_{\mathbf{r}_T}(d)\mathrm{d}d/\Phi}{XY/\Phi} \\ &= \frac{A_{\mathbf{r}_T}(d)\mathrm{d}d}{XY},\end{aligned} \tag{3.24}$$

where Φ denotes the size of the infinitely extended plane.

We define the probability that distance between an Rx with Tx locating at $\mathbf{r}_T$ is d as $\mathscr{P}_{\mathbf{r}_T}(d)$. With given Tx locating at $\mathbf{r}_T$, the probability that an Rx is inside the building when

it is d far from Tx can be defined as $\mathscr{P}_{\mathbf{r}_\mathrm{T}}(\chi|d)$, which can be calculated as:

$$\begin{aligned}\mathscr{P}_{\mathbf{r}_\mathrm{T}}(\chi|d) &= \frac{\mathscr{P}_{\mathrm{arc},\mathbf{r}_\mathrm{T}}(d)}{\mathscr{P}_{\mathbf{r}_\mathrm{T}}(d)} \\ &= \frac{A_{\mathbf{r}_\mathrm{T}}(d)}{2\pi d}.\end{aligned} \tag{3.25}$$

Combining Eq. (3.24) and (3.25), we can derive:

$$\mathscr{P}_{\mathbf{r}_\mathrm{T}}(d|\chi) = \frac{2\pi d\,\mathscr{P}_{\mathbf{r}_\mathrm{T}}(\chi|d)\mathrm{d}d}{XY}. \tag{3.26}$$

For Tx at all possible positions in the BUD, the probability that the randomly located Rx is d far from Tx is in the building is:

$$\mathscr{P}(\chi|d) = \int_0^Y \int_0^X \mathscr{P}_{\mathbf{r}_\mathrm{T}}(\chi|d)\mathrm{d}x_\mathrm{T}\mathrm{d}y_\mathrm{T}. \tag{3.27}$$

Based on the definition of $Z(d,a,b)$ that has been explained in Lemma 1, (3.27) can be expressed as:

$$\mathscr{P}(\chi|d) = Z(d,Y,X). \tag{3.28}$$

Combining (3.26), (3.27) and (3.28), for any randomly located Rx in the building, the probability that its distance from Tx located at $\mathbf{r}_\mathrm{T}$ is d can be derived as:

$$\begin{aligned}p_{\iota,\chi}(d) &= \int_0^Y \int_0^X \mathscr{P}_{\mathbf{r}_\mathrm{T}}(d|\chi)\mathrm{d}x_\mathrm{T}\mathrm{d}y_\mathrm{T} \\ &= \int_0^Y \int_0^X \frac{2\pi d\,\mathscr{P}_{\mathbf{r}_\mathrm{T}}(\chi|d)}{XY}\mathrm{d}x_\mathrm{T}\mathrm{d}y_\mathrm{T} \\ &= \frac{2\pi d\,\mathscr{P}(\chi|d)}{XY} \\ &= \frac{2\pi d Z(d,Y,X)}{XY}.\end{aligned} \tag{3.29}$$

□

Theorem 3.1. *The* $\mathrm{E}[\tau_\mathrm{I}]$ *can be derived as an analytical expression as:*

$$\begin{aligned}\mathrm{E}[\tau_{\mathrm{I}}] = \sum_{i}^{N_{\mathrm{r}}} \frac{S_n}{V} \int_0^{+\infty} \frac{2\pi d}{XY} \Bigg[& Z(d,l_n,m_n) \left(\frac{\sigma_{\mathrm{LOS},\upsilon_n,\tau_{\mathrm{I}}}}{\sqrt{2\pi}} \exp\left(-\frac{1}{2} \left(\frac{\mu_{\mathrm{LOS},\upsilon_n,\tau_{\mathrm{I}}}(d)}{\sigma_{\mathrm{LOS},\upsilon_n,\tau_{\mathrm{I}}}} \right)^2 \right) \right. \\ & \left. + \frac{\mu_{\mathrm{LOS},\upsilon_n,\tau_{\mathrm{I}}}(d)}{2} \mathrm{erfc}\left(-\frac{\mu_{\mathrm{LOS},\upsilon_n,\tau_{\mathrm{I}}}(d)}{\sqrt{2}\sigma_{\mathrm{LOS},\upsilon_n,\tau_{\mathrm{I}}}} \right) \right) \\ & + (Z(d,Y,X) - Z(d,l_n,m_n)) \left(\frac{\sigma_{\mathrm{NLOS},\upsilon_n,\tau_{\mathrm{I}}}}{\sqrt{2\pi}} \exp\left(-\frac{1}{2} \left(\frac{\mu_{\mathrm{NLOS},\upsilon_n,\tau_{\mathrm{I}}}(d)}{\sigma_{\mathrm{NLOS},\upsilon_n,\tau_{\mathrm{I}}}} \right)^2 \right) \right. \\ & \left. + \frac{\mu_{\mathrm{NLOS},\upsilon_n,\tau_{\mathrm{I}}}(d)}{2} \mathrm{erfc}\left(-\frac{\mu_{\mathrm{NLOS},\upsilon_n,\tau_{\mathrm{I}}}(d)}{\sqrt{2}\sigma_{\mathrm{NLOS},\upsilon_n,\tau_{\mathrm{I}}}} \right) \right) \Bigg] \mathrm{d}d. \end{aligned} \tag{3.30}$$

Proof. By substituting (3.9), (3.10), (3.11), (3.16), (3.17), and (3.23) into (3.6), we have an analytical expression of $\mathrm{E}[\tau_{\mathrm{I}}]$ as:

$$\begin{aligned}\mathrm{E}[\tau_{\mathrm{I}}] = \int_1^{+\infty} \tau_{\mathrm{I}} \int_0^{+\infty} \sum_{n}^{N_{\mathrm{r}}} \frac{S_n}{V} \frac{2\pi d}{XY} \Bigg[& \frac{Z(d,l_n,m_n)}{\sqrt{2\pi}\sigma_{\mathrm{LOS},\upsilon_n,\tau_{\mathrm{I}}}} \exp\left(-\frac{1}{2} \left(\frac{\tau_{\mathrm{I}} - \mu_{\mathrm{LOS},\upsilon_n,\tau_{\mathrm{I}}}(d)}{\sigma_{\mathrm{LOS},\upsilon_n,\tau_{\mathrm{I}}}} \right)^2 \right) \\ & + \frac{Z(d,Y,X) - Z(d,l_n,m_n)}{\sqrt{2\pi}\sigma_{\mathrm{NLOS},\upsilon_n,\tau_{\mathrm{I}}}} \exp\left(-\frac{1}{2} \left(\frac{\tau_{\mathrm{I}} - \mu_{\mathrm{NLOS},\upsilon_n,\tau_{\mathrm{I}}}(d)}{\sigma_{\mathrm{NLOS},\upsilon_n,\tau_{\mathrm{I}}}} \right)^2 \right) \Bigg] \mathrm{d}d\mathrm{d}\tau_{\mathrm{I}}. \end{aligned} \tag{3.31}$$

After exchanging the integral order and some straight forward derivation, we can obtain a more computationally tractable analytical solution as (3.30). □

3.3.2 Derivation of $\mathrm{E}[\tau_{\mathrm{O}}]$

With the same assumption in subsection III-A, $\mathrm{E}[\tau_{\mathrm{O}}]$ can be calculated in the open space whose range is the same as the BUD as:

$$\mathrm{E}[\tau_{\mathrm{O}}] = \int_0^{+\infty} p_{\iota,\chi}(d) \int_{\mathbf{r}} \tau_{\mathrm{O},\chi|\mathbf{r}_{\mathrm{T}}}(d) g_{\mathbf{r}_{\mathrm{T}}}(\mathbf{r}) \mathrm{d}\mathbf{r}\mathrm{d}d. \tag{3.32}$$

where $\tau_{\mathrm{O},\chi|\mathbf{r}_{\mathrm{T}}}(d)$ denotes the RMS-DS in the open space when the transmission distance is d. Given (3.9), (3.10), and (3.23), as long as we have the analytical expression of $\tau_{\mathrm{O},\chi|\mathbf{r}_{\mathrm{T}}}(d)$, we can derive $\mathrm{E}[\tau_{\mathrm{O}}]$. $\tau_{\mathrm{O},\chi|\mathbf{r}_{\mathrm{T}}}(d)$ is given in Lemma 3.

Lemma 3. *$\tau_{\mathrm{O},\chi|\mathbf{r}_\mathrm{T}}(d)$ can be derived in a closed-form expression as*

$$\tau_{\mathrm{O},\chi|\mathbf{r}_\mathrm{T}}(d) = \frac{d_\mathrm{D} d_\mathrm{R}(d_\mathrm{R}-d_\mathrm{D})}{c(d_\mathrm{D}^2+d_\mathrm{R}^2)}, \tag{3.33}$$

$$= \frac{\sqrt{d^2+(h_\mathrm{T}-h_\mathrm{R})^2}\left(\sqrt{\frac{d^2h_\mathrm{R}^2}{(h_\mathrm{R}+h_\mathrm{T})^2}+h_\mathrm{R}^2}+\sqrt{\frac{d^2h_\mathrm{T}^2}{(h_\mathrm{R}+h_\mathrm{T})^2}+h_\mathrm{T}^2}\right)}{c\left(\left(\sqrt{\frac{d^2h_\mathrm{R}^2}{(h_\mathrm{R}+h_\mathrm{T})^2}+h_\mathrm{R}^2}+\sqrt{\frac{d^2h_\mathrm{T}^2}{(h_\mathrm{R}+h_\mathrm{T})^2}+h_\mathrm{T}^2}\right)^2+d^2+(h_\mathrm{T}-h_\mathrm{R})^2\right)}$$
$$\times\left(\sqrt{\frac{d^2h_\mathrm{R}^2}{(h_\mathrm{R}+h_\mathrm{T})^2}+h_\mathrm{R}^2}+\sqrt{\frac{d^2h_\mathrm{T}^2}{(h_\mathrm{R}+h_\mathrm{T})^2}+h_\mathrm{T}^2}-\sqrt{d^2+(h_\mathrm{T}-h_\mathrm{R})^2}\right), \tag{3.34}$$

where c denotes the light speed.

Proof. In this chapter, we have assumed that the RMS-DS in the open space is calculated using a two-ray model. It assumes that in an open environment, the signal will travel through two paths: a direct path and a reflected path through the ground, as fig. 3.2 shows [112]. As introduced in Chapter 3 (2.3) and (2.4), in the two-ray model, the RMS-DS is given by the weighted root mean square of the delay of the directive path and the delay of the reflective path as (3.33). Therefore, $\tau_{\mathrm{O},\chi|\mathbf{r}_\mathrm{T}}(d)$ can be derived as (3.34), where c denotes the light speed.

□

Theorem 3.2. *The* $\mathrm{E}[\tau_\mathrm{O}]$ *can be derived in an analytical expression as:*

$$\mathrm{E}[\tau_\mathrm{O}] = \int_0^{+\infty} \frac{2\pi dZ(d,Y,X)}{XYc} \frac{\sqrt{d^2+(h_\mathrm{T}-h_\mathrm{R})^2}\left(\sqrt{\frac{d^2h_\mathrm{R}^2}{(h_\mathrm{R}+h_\mathrm{T})^2}+h_\mathrm{R}^2}+\sqrt{\frac{d^2h_\mathrm{T}^2}{(h_\mathrm{R}+h_\mathrm{T})^2}+h_\mathrm{T}^2}\right)}{\left(\left(\sqrt{\frac{d^2h_\mathrm{R}^2}{(h_\mathrm{R}+h_\mathrm{T})^2}+h_\mathrm{R}^2}+\sqrt{\frac{d^2h_\mathrm{T}^2}{(h_\mathrm{R}+h_\mathrm{T})^2}+h_\mathrm{T}^2}\right)^2+d^2+(h_\mathrm{T}-h_\mathrm{R})^2\right)}$$
$$\times\left(\sqrt{\frac{d^2h_\mathrm{R}^2}{(h_\mathrm{R}+h_\mathrm{T})^2}+h_\mathrm{R}^2}+\sqrt{\frac{d^2h_\mathrm{T}^2}{(h_\mathrm{R}+h_\mathrm{T})^2}+h_\mathrm{T}^2}-\sqrt{d^2+(h_\mathrm{T}-h_\mathrm{R})^2}\right)\mathrm{d}d. \tag{3.35}$$

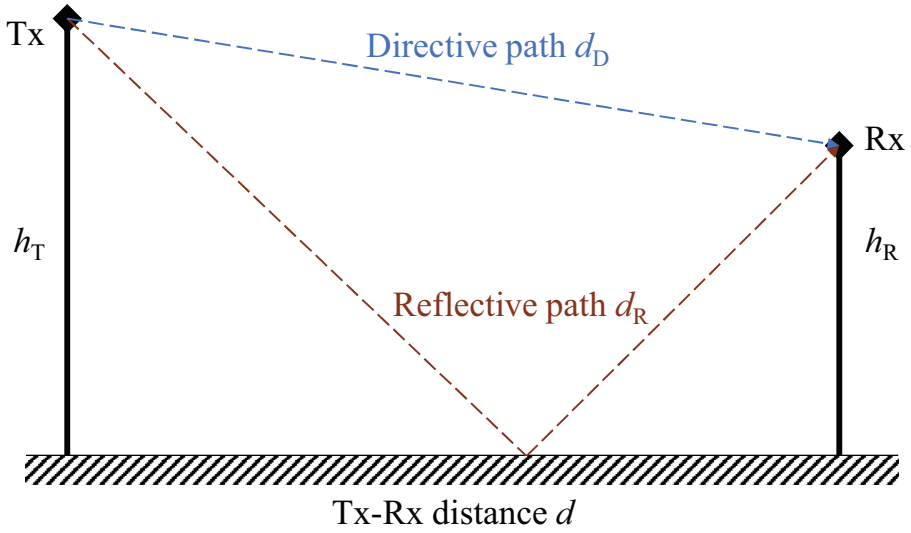

Fig. 3.2 Two ray model.

Proof. By substituting (3.9), (3.10), (3.23), and (3.34) into (3.32), the analytical expression of $\mathrm{E}[\tau_O]$ can be obtained as (3.35) via straightforward derivations. □

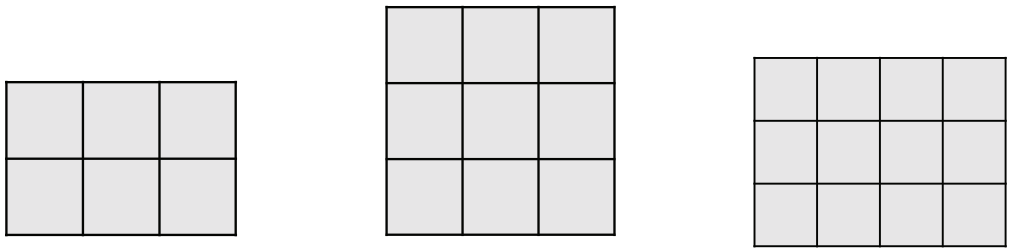

(a) 2 by 3 (b) 3 by 3 (c) 3 by 4

Fig. 3.3 The N by M rooms layouts.

3.3.3 Derivation of G_τ

Based on Theorems 1 and 2, we can derive the analytic expression of G_τ as follows.

By substituting (3.30) and (3.35) into (3.3), and only consider the far-field conditions, we finally obtain the analytical expression of G_τ as:

$$
\begin{aligned}
G_\tau = & \sum_{n}^{N_\mathrm{r}} \frac{S_n}{V} \int_1^{+\infty} \frac{2\pi d}{XY} \left[\frac{Z(d,l_n,m_n)\sigma_{\mathrm{LOS},\upsilon_n,\tau_\mathrm{I}}}{\sqrt{2\pi}} \exp\left(-\frac{1}{2} \left(\frac{\mu_{\mathrm{LOS},\upsilon_n,\tau_\mathrm{I}}(d)}{\sigma_{\mathrm{LOS},\upsilon_n,\tau_\mathrm{I}}} \right)^2 \right) \right. \\
& + \frac{Z(d,l_n,m_n)\mu_{\mathrm{LOS},\upsilon_n,\tau_\mathrm{I}}(d)}{2} \mathrm{erfc}\left(-\frac{\mu_{\mathrm{LOS},\upsilon_n,\tau_\mathrm{I}}(d)}{\sqrt{2}\sigma_{\mathrm{LOS},\upsilon_n,\tau_\mathrm{I}}} \right) \\
& + \frac{(Z(d,Y,X) - Z(d,l_n,m_n))\,\sigma_{\mathrm{NLOS},\upsilon_n,\tau_\mathrm{I}}}{\sqrt{2\pi}} \exp\left(-\frac{1}{2} \left(\frac{\mu_{\mathrm{NLOS},\upsilon_n,\tau_\mathrm{I}}(d)}{\sigma_{\mathrm{NLOS},\upsilon_n,\tau_\mathrm{I}}} \right)^2 \right) \\
& \left. + \frac{(Z(d,Y,X) - Z(d,l_n,m_n))\,\mu_{\mathrm{NLOS},\upsilon_n,\tau_\mathrm{I}}(d)}{2} \mathrm{erfc}\left(-\frac{\mu_{\mathrm{NLOS},\upsilon_n,\tau_\mathrm{I}}(d)}{\sqrt{2}\sigma_{\mathrm{NLOS},\upsilon_n,\tau_\mathrm{I}}} \right) \right] \mathrm{d}d \\
& - \int_0^{+\infty} \frac{2\pi d Z(d,Y,X)}{XYc} \frac{\sqrt{d^2 + (h_\mathrm{T} - h_\mathrm{R})^2} \left(\sqrt{\frac{d^2 h_\mathrm{R}^2}{(h_\mathrm{R}+h_\mathrm{T})^2} + h_\mathrm{R}^2} + \sqrt{\frac{d^2 h_\mathrm{T}^2}{(h_\mathrm{R}+h_\mathrm{T})^2} + h_\mathrm{T}^2} \right)}{\left(\left(\sqrt{\frac{d^2 h_\mathrm{R}^2}{(h_\mathrm{R}+h_\mathrm{T})^2} + h_\mathrm{R}^2} + \sqrt{\frac{d^2 h_\mathrm{T}^2}{(h_\mathrm{R}+h_\mathrm{T})^2} + h_\mathrm{T}^2} \right)^2 + d^2 + (h_\mathrm{T} - h_\mathrm{R})^2 \right)} \\
& \times \left(\sqrt{\frac{d^2 h_\mathrm{R}^2}{(h_\mathrm{R}+h_\mathrm{T})^2} + h_\mathrm{R}^2} + \sqrt{\frac{d^2 h_\mathrm{T}^2}{(h_\mathrm{R}+h_\mathrm{T})^2} + h_\mathrm{T}^2} - \sqrt{d^2 + (h_\mathrm{T} - h_\mathrm{R})^2} \right) \mathrm{d}d. \qquad (3.36)
\end{aligned}
$$

3.4 Numerical Results

For validating the model's reliability, the Monte-Carlo simulations are first performed in room layouts of 3 by 2 and 3 by 3. In Monte Carlo simulation, all propagation environments in evaluated buildings are assumed to be consistent with the propagation environment measured in [34]. When assessing a building consisting of a single type of room, the room is assumed to be consistent with the communication environment of the office in [34]. Fig. 3.3 illustrates the naming conventions for a single type of room layout, e.g., N by M denotes a room layout consisting of N rows and M columns. h_t is set as 4 m and h_r is set as 3 m for all scenarios. The model is then verified step by step. In every Monte-Carlo simulation, we randomly pick 10000 positions in the scene to position transmitters and receivers, respectively, and then established one-to-one communication links for them.

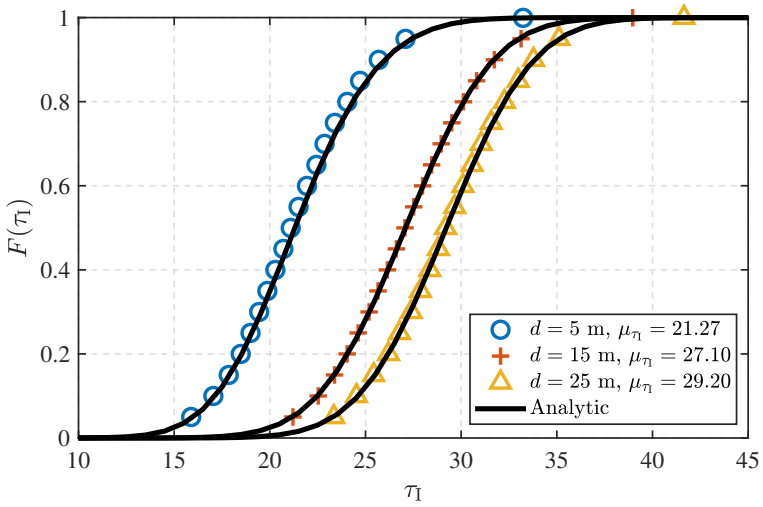

(a) CDFs of τ_I in a 3 by 2 scenario.

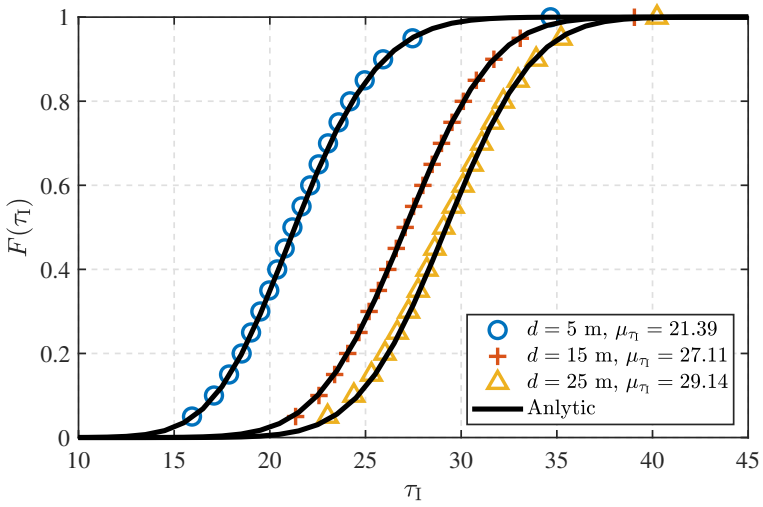

(b) CDFs of τ_I in a 3 by 3 scenario.

Fig. 3.4 CDF of τ with different d in 3 by 2 and 3 by 3 scenarios.

The Cumulative Distribution Functions (CDFs) of RMS-DS for 3 by 2 and 3 by 3 room layouts at various transceiver distances ($d = 5$ m, 15 m, and 25 m) are compared to the analytical values determined by (3.16) in Fig. 3.4. As can be observed, the statistical results closely correspond to the simulated values in different layouts. The images demonstrate that the expectation value of τ_I, denoted as μ_{τ_I}, grows as the transceiver distance d increases and the increase is more pronounced with a shorter d.

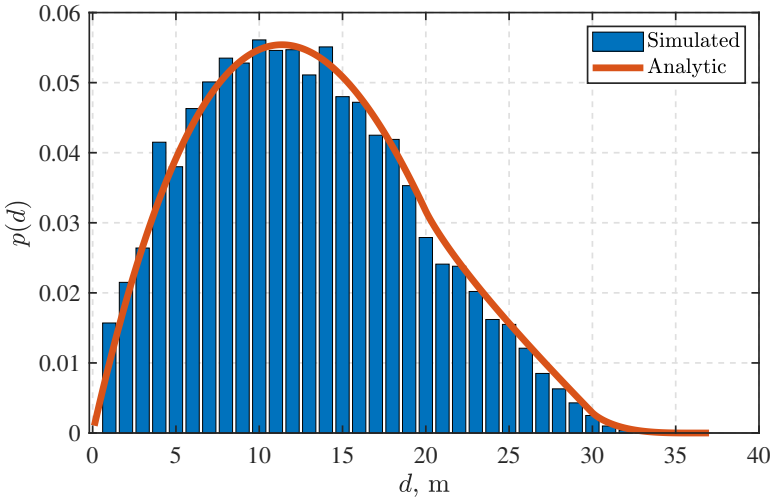

(a) PDF of d in a 3 by 2 scenario.

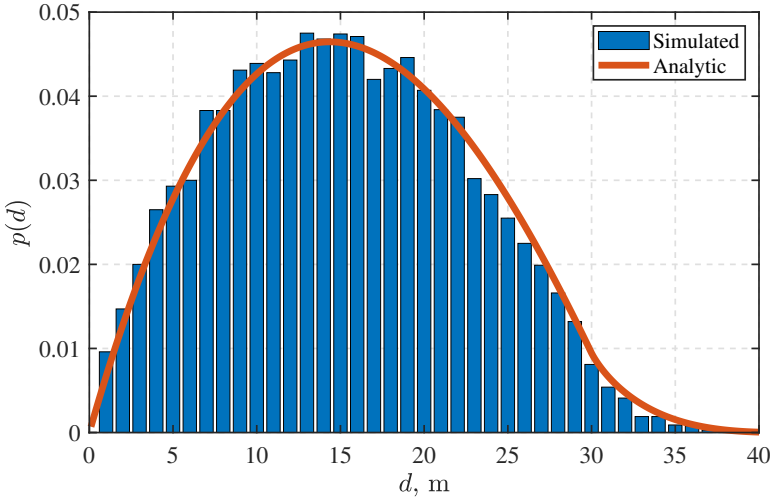

(b) PDF of d in a 3 by 3 scenario.

Fig. 3.5 PDF of d in 3 by 2 and 3 by 3 scenarios.

Fig. 3.5 illustrates the PDFs of d in 3 by 2 and 3 by 3 room layouts when the transmitter and receiver positions are randomly chosen. The statistical values are accurate when compared to the simulated results.

The τ_{I} values for all links simulated using the Monte-Carlo method are shown in Fig. 3.6 in comparison to the analytic solution of $f_{\tau_{\mathrm{I}}}(d)$. Fig. 3.6 also shows the expectation value of simulation results in τ-dimension with the interval of 2 m, represented by markers '$\triangle$'. Additionally, in Fig. 3.6, we display the $f_{\tau_{\mathrm{I}}}(d)$ values for these distances in an open environment. This picture confirms the accuracy of the proposed model and cross-validates

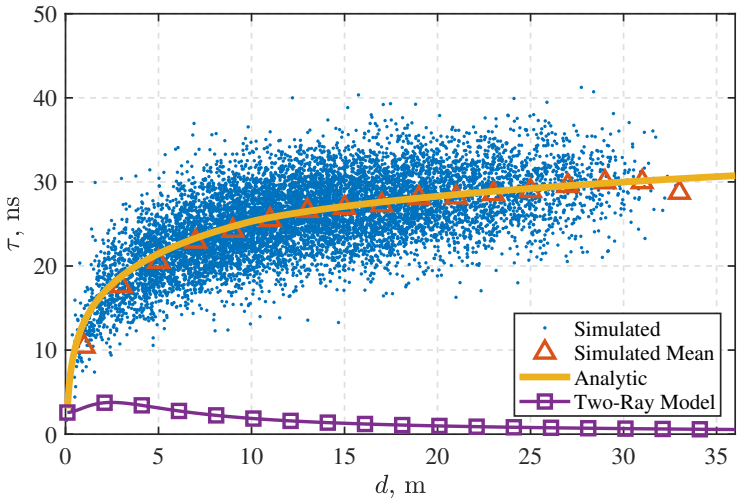

(a) Comparisons in a 3 by 2 scenario.

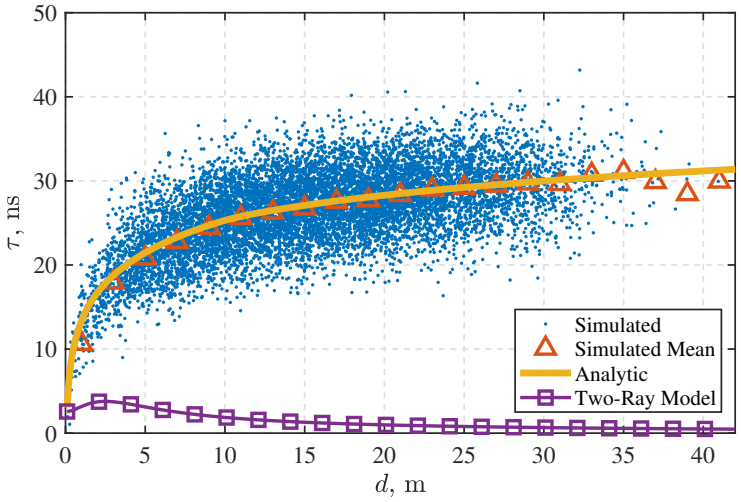

(b) Comparisons in a 3 by 3 scenario.

Fig. 3.6 The simulated values of τ_{I} are compared with the analytic value and the τ_{O} values for corresponding two-ray models.

the relationship between $f_{\tau_{\mathrm{I}}}(d)$ and distance d combined with Fig. 3.4. At shorter d, $f_{\tau_{\mathrm{I}}}(d)$ increases with d faster. This may be because the increase in d at this stage dramatically increases the complexity of the communication environment, i.e., a small increase in distance may cause the link to transform from LOS to NLOS. Furthermore, when d is excessively long, $f_{\tau_{\mathrm{I}}}(d)$ increases slowly with d. This is because the communication environment is already harsh: increasing the distance between nodes will merely result in path loss growth and will have little effect on the LOS/NLOS conditions. By contrast, the value of τ_{O} in an

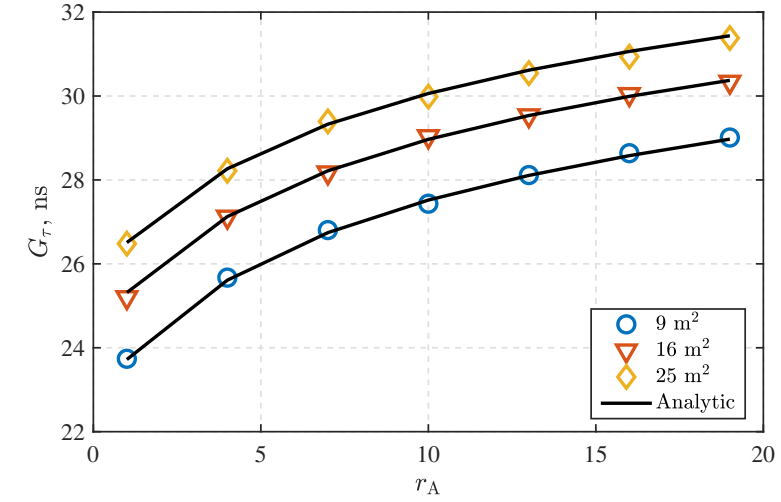

(a) Comparison in scenarios with different room areas.

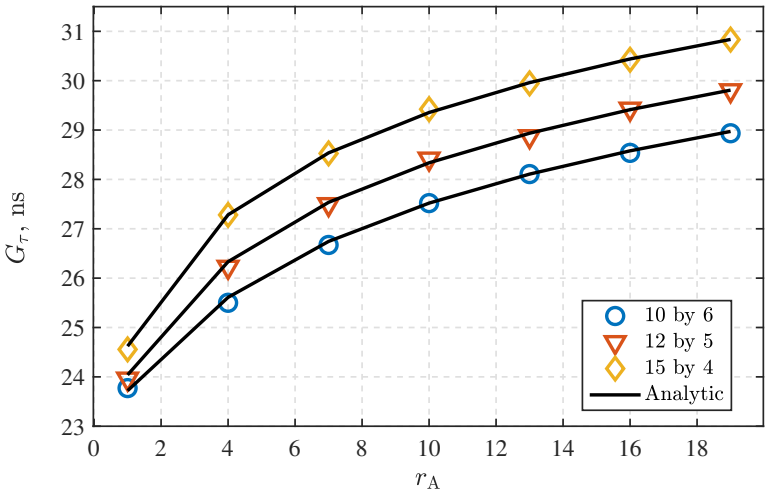

(b) Comparison in scenarios with different room layouts.

Fig. 3.7 Comparison of G_τ with different aspect ratio r_A in different scenarios.

ideal open area diminishes with increasing d because the distance gap between direct and reflected paths becomes less apparent.

Following that, we placed the single-type rooms in a number of layouts to demonstrate the model's universality and to make a preliminary summary of the effect of room layout on channel DS performance. The Figs. 3.7a and 3.7b illustrate the effect of room aspect ratios to G_τ when the unit rooms areas are fixed. In Fig. 3.7a, the same layouts of 10 by 6 rooms are employed, and the G_τ of identical aspect ratio r_A rooms with varying room sizes are also

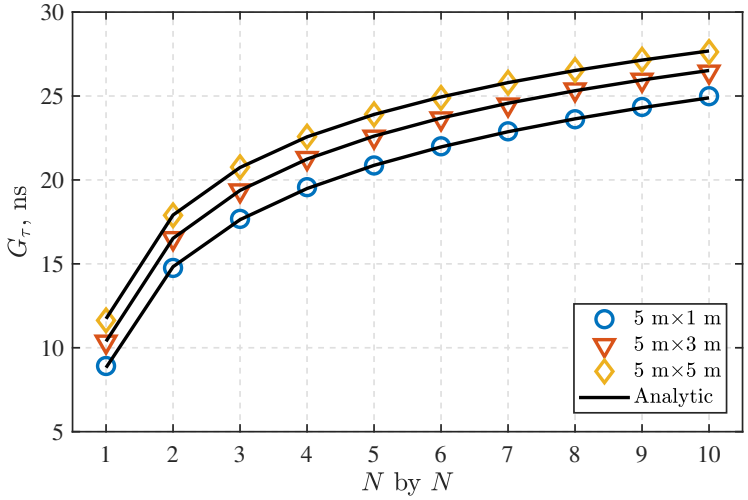

(a) Comparison in scenarios with different room areas.

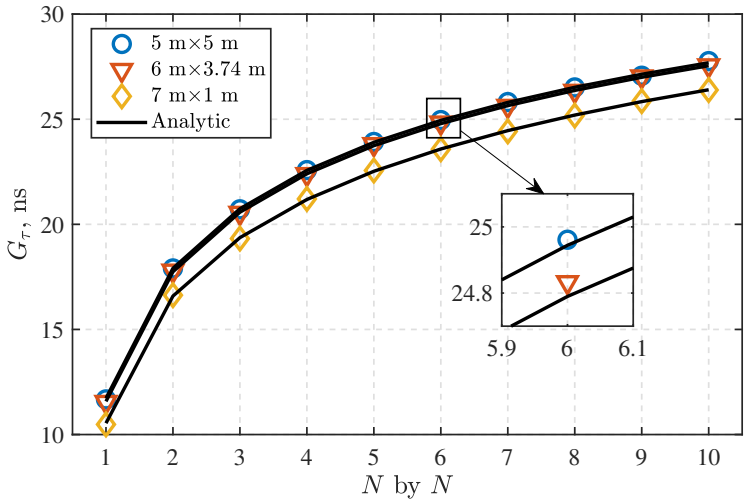

(b) Comparison in scenarios with same diagonal but different aspect ratio.

Fig. 3.8 Comparison of G_τ with different room layouts in different scenarios.

compared longitudinally. As shown, when the unit room area is fixed, G_τ increases as r_A grows. Additionally, when the r_A is fixed, the larger unit room area results in a larger G_τ.

In Fig. 3.7b, 60 same 9 m^2 rooms is employed, and the G_τ of identical aspect ratio r_A rooms with varying room layouts (15 by 4, 12 by 5 and 10 by 6) are also compared longitudinally. As shown, when both unit area and total area remain unchanged, room layouts will also affect G_τ, i.e., the floor with a bigger aspect ratio can cause a greater G_τ. What these two phenomena have in common is that a higher aspect ratio with the same room area or a larger room area with the same room layout can lead to a longer communication link within

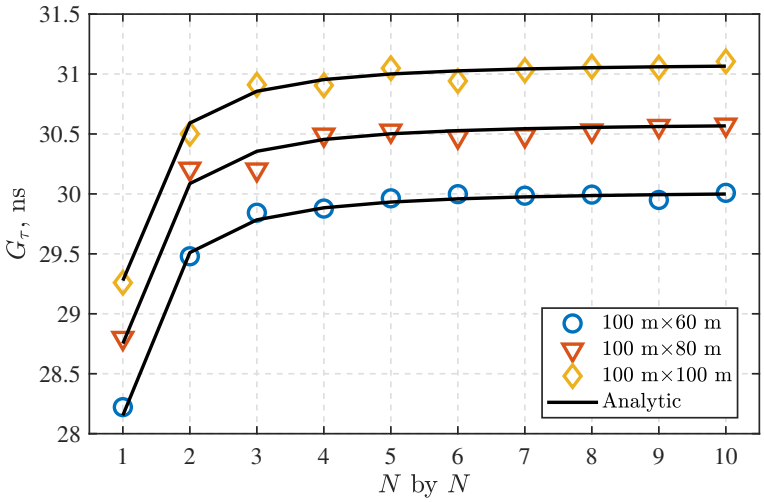

(a) Comparison in a floor with N by N room layouts.

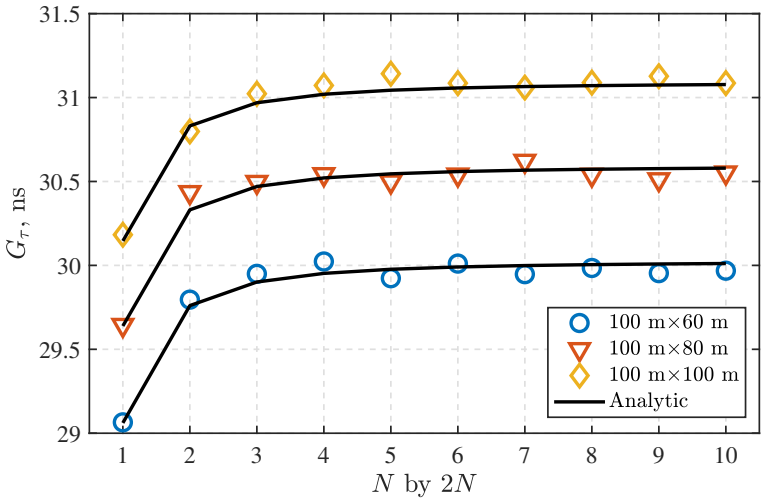

(b) Comparison in a floor with N by $2N$ room layouts.

Fig. 3.9 Comparison of G_τ with different room layouts within the same-sized floor

the building. Because the longer the distance, the bigger the RMS-DS, and hence the greater the RMS-DS expectation of the building in these instances. Fig.3.7b also demonstrates that as rooms are placed to make the building longer and narrower, the G_τ increases. This is also because a narrower building with the same area has a higher probability of having a longer transmission distance.

Similar influences apply to Fig. 3.8a. Fig. 3.8a illustrates the changes in G_τ induced by similar room arrangements with the varying number of rooms and vertically compares G_τ with the same room layouts but different unit room areas. Similarly, with a constant

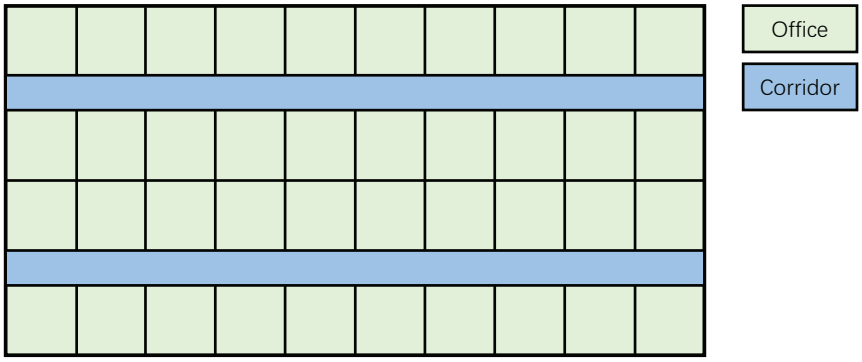

(a) The room layout in Winner II A1 scenario

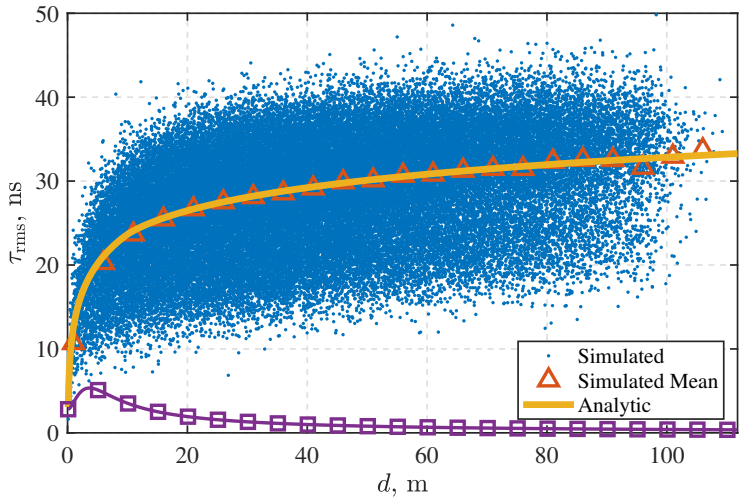

(b) Comparisons between the simulated results and the analytic value.

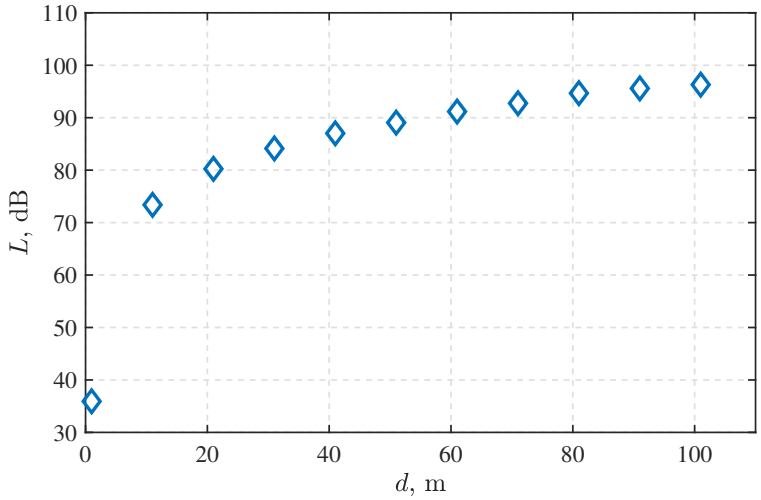

(c) The mean value of the path loss in different d in the BUD

Fig. 3.10 The simulated values of τ_{I} are compared with the analytic value of the Winner II A1 scenario and the τ_{O} values for corresponding two-ray models.

room area, adding more rooms increases G_τ substantially. On the one hand, the increase in room number, along with the increase in building area, results in an increase in the possible transmission distance. On the other hand, more rooms result in a greater probability of NLOS transmissions. Vertically comparing, increasing the room areas increases G_τ in this figure, which is also related to the increased maximum transceiver distance.

To shield the effect of varying maximum potential propagation lengths on G_τ, we fixed the diagonal lengths of the unit rooms and compared G_τ again, as shown in Fig. 3.8b. It shows that under the condition that the diagonal length, namely the maximum communication distance, is fixed, G_τ will still be affected by the building area – the smaller the building area, the better the building's wireless performance on G_τ.

Finally, we partitioned a fix-sized building into N by N and N by $2N$ same-sized rooms and compared their G_τ, as seen in Fig. 3.9a and Fig. 3.9b respectively. When a building follows a set contour, adding rooms results in a larger G_τ. This effect is more noticeable when there are fewer rooms and less noticeable when there are enough rooms because the majority of the building's links are NLOS at this stage, and thus adding rooms has little influence on the RMS-DS.

Combined with the above analysis, we discover that the maximum potential transceiver distance in a BUD and the area of the building are the primary determinants of the assessed building's G_τ. When a building has a longer diagonal length or a larger area, it will have a greater G_τ. When there are fewer rooms, the increase of walls substantially raises G_τ, but this element becomes insignificant when there are more rooms.

Finally, we validated the model by comparing the simulated and analytic values of G_τ for a real indoor scenario. This scenario is a 50 m $\times$ 100 m indoor scenario referred from Winner II A1 scenario [35], which consists of 40 identical 10 m $\times$ 10 m offices and two 5 m $\times$ 100 m corridors. The simulated result is $G_{\tau,\text{sim}} = 27.7866$ ns, and the analytical result is $G_{\tau,\text{ana}} = 27.7435$ ns. Detailed simulation results are shown in Fig. 3.10b. These results demonstrate that the proposed model can also accurately and quickly evaluate the actual complex building structures. Fig. 3.10c shows the average path loss for a randomly simulated transceiver link in the building and its relationship to distance. It presents a linear correlation

with in-building RMS-DS compared with Fig. 3.10b. When the transceiver link is too long, it is difficult for the link to realise effective communication with a significant path loss, and the RMS-DS of the transceiver link is also larger. Therefore, the proposed DS gap can also indirectly reflect the communication realisability of indoor wireless systems in the BUD.

3.5 Conclusions

In this chapter, the metric of DS gap was defined to build the BWP evaluation scheme of channel DS. The DS gap, G_τ, is the metric that is defined by comparing the expected RMS-DS within a building to the RMS-DS in an open space with the same topography. Firstly, the analytical probability distribution model of the RMS-DS of the entire building with the transceiver distance was derived by integrating the RMS-DS model of a single room with the room arrangement of a building. Then, the PDF of the transceiver distance within the building and the analytical solution for calculating G_τ were derived. A metric σ was also defined and derived to assess model reliability. Finally, G_τ values were obtained in various room layouts through simulation and were compared to those of the analytical model, demonstrating that the proposed model could accurately evaluate the channel DS performance of a building under design. The work in this chapter provides the channel DS evaluation guidelines for future building design, which is a critical aspect of the BWP evaluation framework. As the RMS-DS has a profound impact on wireless system design, the work is very relevant to future generations of wireless systems that need to support services with extreme requirements on latency, reliability and capacity.

Chapter 4

BWP Evaluation of Channel Hardening for Massive MIMO Systems

Overview

This chapter proposes the first building wireless performance evaluation scheme considering channel hardening for an indoor massive MIMO system. Firstly, a metric, CHO, is defined to describe the average channel hardening ratio of a BUD. Then, the analytic model and the approximation closed-form expression are derived for the defined metric. Finally, Monte-Carlo simulations are carried out to validate the proposed scheme under various indoor scenarios, indicating the correlation between the CHO and BUD's room layouts. The proposed evaluation scheme can be used to design new or retrofit existing buildings with adequate massive MIMO performance.

4.1 Introduction

4.1.1 Background and Motivations

In the 5G and 6G eras, more than 80% of wireless traffic is generated indoors [7]. For meeting the explosive indoor traffic demand, the massive MIMO system has become an important technology to improve the spectral efficiency of indoor wireless systems.

In a massive MIMO system, the channel gain becomes more stable to its mean with the BSs' antenna amounts increasing, which is called channel hardening [87]. Stable channels can guarantee the reliability of a communication system [30]. Channel hardening improves the signal quality by reducing the influence of the multipath effect. This enables the system to achieve higher data transfer rates in complex channel environments and provide more reliable communication. In addition, channel hardening can also extend the coverage of the system. Due to channel hardening, the system can achieve reliable transmission over a longer distance and improve the system's coverage. Therefore, the greater the degree of channel hardening, the higher the reliability of massive MIMO systems [113]. This phenomenon enables the system to provide more reliable and efficient wireless communication services in complex communication environments.

The complete convergence of channel hardening in the massive MIMO system with uncorrelated Rayleigh fading was proven in [114]. On this basis, researchers in [90] proposed the model of the channel hardening ratio of the Rayleigh channel in different communication scenarios, yet the spatial correlation has not been included. Then in [30], the authors presented a comprehensive model of channel hardening ratio for Ricean fading channels with LOS and NLOS components, including the spatial correlation.

The structure of a building has a significant impact on the channel hardening property of a massive MIMO system in the building. For example, in a Ricean channel, for different K factors, the same Tx and Rx configuration will lead to a different degree of channel hardening effect [30]. As a result, it is necessary to study how building structures affect the channel hardening of massive MIMO networks, which has been neglected by all existing research on massive MIMO channel hardening.

4.1.2 Contributions in This Chapter

In order to bridge the gap between the BWP evaluation and the channel hardening modelling of massive MIMO networks, this chapter proposes a new system-level evaluation method for channel hardening in indoor massive MIMO systems. Specifically, a novel BWP evaluation metric, CHO, is proposed to evaluate the influence of a BUD on channel hardening ratio. The

analytic model of the proposed evaluation metric is also given in detail to assist architects in quickly quantifying the impact of an architectural design on the performance of an indoor wireless network in terms of channel hardening.

4.2 Definition of the Metric to Evaluate Channel Hardening Ratio in BWP

Mathematically, defining $\mathbf{h}$ as the $M \times 1$ channel vector between the M-antenna Tx and the single-antenna Rx in the massive MIMO system, the channel $\mathbf{h}$ hardens when

$$\frac{\mathrm{Var}\{\|\mathbf{h}\|^2\}}{\mathrm{E}\{\|\mathbf{h}\|^2\}^2} \to 0, \text{ as } M \to \infty. \tag{4.1}$$

As described in the preceding sections, the higher the degree of channel hardening, the higher the system reliability. Researchers in [30, 89] defined the channel hardening ratio ξ to describe this proximity between channel $\mathbf{h}$ and the perfect channel hardening states:

$$\xi = \frac{\mathrm{Var}\{\|\mathbf{h}\|^2\}}{\mathrm{E}\{\|\mathbf{h}\|^2\}^2}. \tag{4.2}$$

The smaller the ξ, the higher the degree of channel hardening of $\mathbf{h}$, resulting in better network reliability.

According to the concept of ξ, we define a BWP evaluation metric, CHO, as O_{CH}, to describe the ratio of the expectation value of ξ in the BUD and the expectation value of ξ in the same-sized open space of the BUD as:

$$O_{\mathrm{CH}} = \frac{\mathrm{E}[\xi_{\mathrm{I}}]}{\mathrm{E}[\xi_{\mathrm{O}}]}, \tag{4.3}$$

where ξ_{I} is the channel hardening ratio for any possible channel in the BUD, ξ_{O} is the channel hardening ratio for any possible channel in the open space within the same size of the BUD, $\mathrm{E}[\xi_{\mathrm{I}}]$ denotes the expectation value of the channel hardening ratio for the assessed indoor

environment, and $\mathrm{E}[\xi_{\mathrm{O}}]$ denotes the expectation value of the channel hardening ratio for an open space with the same occupied area.

For a BUD, the larger the CHO, the more difficult it is to achieve channel hardening for the indoor massive MIMO system, and the worse the system's reliability will achieve.

According to [30], ξ depends on i) the distribution of the blockage condition κ between Tx and Rx, ii) antenna number M of the BS, iii) the function $\xi(d)$ of the distance d for a given Tx-Rx link with definite propagation conditions.

To decouple the BUD's inherent properties from specific deployments of indoor wireless devices, we assume that Tx and Rx are randomly distributed in the building, and thus the Tx-Rx distance d follows a specific random distribution, denoted as $p(d)$.

4.3 Analytical Model of the CHO

To quickly and accurately compute the CHO, this section provides the detailed deriving procedure and the final closed-form expression of O_{CH}. $\mathrm{E}[\xi_{\mathrm{I}}]$ and $\mathrm{E}[\xi_{\mathrm{O}}]$ are derived in the following subsections III-A and III-B. Table 4.1 describes the main notations that appear in this chapter.

4.3.1 Derivation of $\mathrm{E}[\xi_{\mathrm{I}}]$

Given the positions of BSs (denoted as Tx) and MUs (denoted as Rxs) in the BUD, the channel hardening ratios' sum of any Tx-Rx link is denoted as ξ_{I}. According to the definition of $\mathrm{E}[\xi_{\mathrm{I}}]$, the expectation value of all possible ξ_{I} can be expressed as:

$$\begin{aligned}\mathrm{E}[\xi_{\mathrm{I}}] &= \int_0^{+\infty} p(d)\xi_{\mathrm{I}}(d)\mathrm{d}d \\ &= \sum_n^{N_{\mathrm{r}}} \int_0^{+\infty} p(d)\xi_{\mathrm{I},n}(d)\mathrm{d}d.\end{aligned} \tag{4.4}$$

Table 4.1 Notation definition for Chapter 4

Notation	Description
$\mathbf{h}$	Channel vector
ξ	Channel hardening ratio
O_{CH}	Channel hardening obstruction
ξ_{I}	Channel hardening ratio sum for any possible channel in the BUD
ξ_{O}	Channel hardening ratio sum for any possible channel in the open space
d	Distance between Tx and Rx
$\mathscr{P}$	Probability of an event
p	PDF of d
κ	The set of blockage situation
υ_n	The event that the Tx is located at the n-th room
$\mathbf{r}$	The coordinates
$\mathbf{r}_{\mathrm{T}}$	The coordinates of Tx location
$\mathbf{r}_{\mathrm{R}}$	The coordinates of Rx location
$g_{\mathbf{r}_{\mathrm{T}}}$	PDF of Tx locating at a position
$g_{\mathbf{r}_{\mathrm{R}}}$	PDF of Rx locating at a position
N_{r}	The amount of rooms in the BUD
S	The size of a room
n	The room number of rooms in the BUD
V	The size of the BUD
m	The long edge of a room
l	The short edge of a room
X	The long edge of the BUD
Y	The short edge of the BUD
M	The number of antenna
ϕ	The angle of arrival
K	The K-factor of the Ricean fading channel
$\mathbf{R}$	The spatial correlation matrix
δ	The correlation coefficient of $\mathbf{R}$
$\mathscr{C}$	The set of coordinates
$J_0(z)$	The Bessel function of the first kind with zero order.

Within a BUD, $\xi_{\mathrm{I}}(d)$ can be calculated as:

$$\xi_{\mathrm{I}}(d) = \int_{\mathbf{r}} \sum_{\kappa} \xi_{\mathbf{r}_{\mathrm{T}}}(\kappa) \mathscr{P}_{\mathbf{r}_{\mathrm{T}}}(\kappa|d) g_{\mathrm{T}}(\mathbf{r}_{\mathrm{T}}) \mathrm{d}\mathbf{r}_{\mathrm{T}}, \tag{4.5}$$

where $\mathscr{P}(\cdot)$ denotes the probability of an event, $\kappa \in \{\mathrm{LOS}, \mathrm{NLOS}\}$ denotes the blockage condition of the Tx-Rx link, Tx locates at $\mathbf{r}_{\mathrm{T}} = (x_{\mathrm{T}}, y_{\mathrm{T}})$, $\mathbf{r}$ denotes all possible locations in the BUD, $g_{\mathrm{T}}(\mathbf{r}_{\mathrm{T}})$ denotes the probability that Tx is located at $\mathbf{r}_{\mathrm{T}}$.

Given that the BUD is composed of N_{r} rooms, and the n-th room is with an area of S_n. Then the total area of the entire building is denoted by V as

$$V = \sum_{n=1}^{N_{\mathrm{r}}} S_n. \tag{4.6}$$

This chapter aims to provide an analytical evaluation of the CHO for a BUD. To facilitate the derivation, we make the following assumptions:

- All rooms in the BUD are assumed to be rectangular. The size of the n-th room S_n can be calculated by $m_n \times l_n$, where m_n denotes the long edge and l_n denotes the short edge of the n-th room. The BUD is also assumed to be rectangular, with a size of $X \times Y$, where X denotes the long edge of the BUD, and Y denotes its short edge. We set the coordinate system on BUD, with the origin at the bottom left.

  The channel hardening ratio of the channel emanated from the n-th room can thus be expressed as $\xi_{\mathrm{I},n}(d)$, that can be derived from (4.5) and expressed as

  $$\xi_{\mathrm{I},n}(d) = \int_{\mathscr{C}_n} \sum_{\kappa} \xi_{\upsilon_n}(\kappa) \mathscr{P}_{\upsilon_n}(\kappa|d) g_{\mathrm{T}|\upsilon_n}(\mathbf{r}_{\mathrm{T}}) \mathscr{P}(\upsilon_n) \mathrm{d}\mathbf{r}_{\mathrm{T}}, \tag{4.7}$$

  where $\mathscr{C}_n$ denotes the set of coordinates occupied by the n-th room, and υ_n denotes the event that Tx is located at the n-th room.

- The Txs and the Rxs are assumed to be distributed uniformly in the BUD. Therefore,

  $$\mathscr{P}(\upsilon_n) = \frac{S_n}{V}. \tag{4.8}$$

Similarly, the conditional PDF of $\mathbf{r}_{\mathrm{T}}$ when Tx is located in the n-th room is defined as $g_{\mathrm{T}|\upsilon_n}(\mathbf{r}_{\mathrm{T}})$:

$$g_{\mathrm{T}|\upsilon_n}(\mathbf{r}_{\mathrm{T}}) = \begin{cases} \frac{1}{S_n} & \mathbf{r}_{\mathrm{T}} \in \mathscr{C}_n, \\ 0, & \text{else.} \end{cases} \tag{4.9}$$

Substituting (4.8) and (4.9) into (4.7), $\xi_{\mathrm{I},n}(d)$ could be simplified as

$$\xi_{\mathrm{I},n}(d) = \frac{S_n}{V} \xi_{\upsilon_n}(\kappa) \mathscr{P}_{\upsilon_n}(\kappa|d). \tag{4.10}$$

By substituting (4.10) into (4.4), $\mathrm{E}[\xi_{\mathrm{I}}]$ can be derived as

$$\mathrm{E}[\xi_{\mathrm{I}}] = \sum_{n}^{N_{\mathrm{r}}} \frac{S_n}{V} \int_0^{+\infty} p(d) \xi_{\upsilon_n}(\kappa) \mathscr{P}_{\upsilon_n}(\kappa|d) \mathrm{d}d. \tag{4.11}$$

- We assume the Tx is a ULA MIMO system with an M-antenna BS, while Rx is a single-antenna user. In the wireless system, the AOA is denoted by ϕ. We assume that the AOA between any Tx and Rx is random and the system is in perfect CSI case. We define $\mathbf{R}$ as a positive semi-definite matrix that denotes the spatial correlation between antennas, subjecting to $\mathbf{Tr}(\mathbf{R}) = M$ [92]. The coefficient between the i-th and the j-th antennas are defined as $e^{-\frac{|i-j|}{\delta}} (i \neq j, i \in M, j \in M)$, where δ denotes the correlation coefficient. For any channel $\mathbf{h}$, we characterise it as a Ricean fading channel with the K-factor, K, consisting of a LOS component on top of an NLOS Rayleigh distributed component.

  According to [30], the hardening ratio of the Tx-Rx channel can be expressed as

$$\xi_{\upsilon_n,\phi}(\kappa) = \frac{2K_{\upsilon_n}(\kappa)\overline{\mathbf{h}}^{\mathrm{H}}\mathbf{R}\overline{\mathbf{h}} + \mathbf{Tr}(\mathbf{R}^2)}{M^2(1+K_{\upsilon_n}(\kappa))^2}, \tag{4.12}$$

  where $K_{\upsilon_n}(\kappa) \geq 0$ ($K_{\upsilon_n} = 0$ only when $\kappa = \text{NLOS}$) and

$$\overline{\mathbf{h}} = \left[1, e^{j\pi\sin\phi}, ..., e^{j(M-1)\pi\sin\phi}\right]^T. \tag{4.13}$$

According to the practical experiment of the indoor scenario A1 from WINNER II [35], we assume that in the indoor scenario, K_{υ_i} is a constant K_{I} in the case of $\kappa = \mathrm{LOS}$, i.e.:

$$K_{\upsilon_i}(\kappa) = \begin{cases} K_{\mathrm{I}}, & \mathrm{LOS}, \\ 0, & \mathrm{NLOS}. \end{cases} \tag{4.14}$$

Then $\mathrm{E}[\xi_{\mathrm{I}}]$ can be further derived as

$$\mathrm{E}[\xi_{\mathrm{I}}] = \sum_{n}^{N_{\mathrm{r}}} \frac{S_n}{V} \int_0^{+\infty} \int_0^{2\pi} \frac{1}{2\pi} p(d) \xi_{\upsilon_n,\phi}(\kappa) \mathscr{P}_{\upsilon_n}(\kappa|d) \mathrm{d}\phi \mathrm{d}d. \tag{4.15}$$

As illustrated from (4.15), the analytical solution of $\mathrm{E}[\xi_{\mathrm{I}}]$ can be obtained as long as we obtain $p(d)$, $\xi_{\upsilon_n,\phi}(\kappa)$ and $\mathscr{P}_{\upsilon_n}(\kappa|d)$, where $\xi_{\upsilon_n,\phi}(\kappa)$ has been expressed as (4.12).

According to the previous work in Chapter 3, $\mathscr{P}_{\upsilon_n,\chi}(\kappa|d)$ can be calculated as

$$\mathscr{P}_{\upsilon_n,\chi}(\kappa|d) = \begin{cases} \frac{Z(d,l_n,m_n)}{Z(d,Y,X)}, & \mathrm{LOS}, \\ 1 - \frac{Z(d,l_n,m_n)}{Z(d,Y,X)}, & \mathrm{NLOS}, \end{cases} \tag{4.16}$$

where $Z(d,a,b), (0 < a \leq b)$ is

$$Z(d,a,b) = \begin{cases} \frac{d^2 - 2d(a+b) + ab\pi}{ab\pi}, & 0 < d \leq a, \\ \frac{-a^2 + 2db(\sqrt{1-\frac{a^2}{d^2}} - 1) + 2ab\arcsin\frac{a}{d}}{ab\pi}, & a < d \leq b, \\ -\frac{d^2 + a^2 + b^2 - 2d(b\sqrt{1-\frac{a^2}{d^2}} + a\sqrt{1-\frac{b^2}{d^2}}) + 2ab(\arccos\frac{a}{d} + \arccos\frac{b}{d} - \frac{\pi}{2})}{ab\pi}, & b < d \leq \sqrt{a^2+b^2}, \\ 0, & \sqrt{a^2+b^2} < d. \end{cases} \tag{4.17}$$

According to the previous work in Chapter 3, $p(d)$ can be calculated as

$$p(d) = \frac{2\pi d Z(d,Y,X)}{XY}, \tag{4.18}$$

where $Z(d)$ is shown in (4.17) as well.

Theorem 4.1. *The* $\mathrm{E}[\xi_{\mathrm{I}}]$ *can be derived as an analytical expression as:*

$$\mathrm{E}[\xi_{\mathrm{I}}] = \sum_{n}^{N_{\mathrm{r}}} \frac{S_n}{X^2 Y^2} \int_0^{2\pi} \left[\frac{2K_{\upsilon_n} \overline{\mathbf{h}}^{\mathrm{H}} \mathbf{R} \overline{\mathbf{h}} + \mathbf{Tr}(\mathbf{R}^2)}{M^2 (1+K_{\upsilon_n})^2} W(l_n, m_n) + \frac{\mathbf{Tr}(\mathbf{R}^2)}{M^2} \left(W(Y,X) - W(l_n,m_n) \right) \right] \mathrm{d}\phi, \tag{4.19}$$

where $\mathbf{h}$ *is expressed as* (4.13) *shows, and* $W(a,b), (0<a<b)$ *is*

$$W(a,b) = \frac{1}{2\pi} \left(ab - b^2\pi + 2b^2 \arccos\frac{a}{b} - 2(a^2+b^2) \arccos\frac{a}{\sqrt{a^2+b^2}} + 2b^2 \arcsin\frac{a}{b} + \left(2a^2+2b^2\right) \arcsin\frac{b}{\sqrt{a^2+b^2}} \right). \tag{4.20}$$

Proof. By substituting (4.12), (4.16) and (4.18) into (4.15), we have an analytical expression of $\mathrm{E}[\xi_{\mathrm{I}}]$ as:

$$\mathrm{E}[\xi_{\mathrm{I}}] = \sum_{n}^{N_{\mathrm{r}}} \frac{S_n}{X^2 Y^2} \int_0^{+\infty} \int_0^{2\pi} \left[\frac{2K_{\upsilon_n} \overline{\mathbf{h}}^{\mathrm{H}} \mathbf{R} \overline{\mathbf{h}} + \mathbf{Tr}(\mathbf{R}^2)}{M^2 (1+K_{\upsilon_n})^2} dZ(d, l_n, m_n) + \frac{\mathbf{Tr}(\mathbf{R}^2)}{M^2} \left(dZ(d,Y,X) - dZ(d,l_n,m_n) \right) \right] \mathrm{d}\phi \mathrm{d}d. \tag{4.21}$$

After exchanging the integral order and straightforward derivation, a more computationally tractable analytical solution can be obtained as (4.19) expresses.

□

4.3.2 Derivation of $\mathrm{E}[\xi_{\mathrm{O}}]$

With the same assumption in subsection 4.3.1, the channel hardening ratio of a channel in open space can be denoted as ξ_{O}. Similar to (4.12), ξ_{O} can be derived as

$$\xi_{\mathrm{O},\phi}(\kappa) = \frac{2K_{\mathrm{O}}(\kappa) \overline{\mathbf{h}}^{\mathrm{H}} \mathbf{R} \overline{\mathbf{h}} + \mathbf{Tr}(\mathbf{R}^2)}{M^2 (1+K_{\mathrm{O}}(\kappa))^2}, \tag{4.22}$$

where $\kappa = \mathrm{LOS}$ is always true in open space. According to the practical experiment of the outdoor scenario B5a from WINNER II, which can be approximated as the measurement of

a scenario in open space [35], we assume that in the open space, $K_{\mathrm{O}}(\mathrm{LOS}) = K_{\mathrm{O}}$ is constant in all cases. Thus, $\xi_{\mathrm{O},\phi}(\kappa)$ can be simplified to $\xi_{\mathrm{O},\phi}$ as

$$\xi_{\mathrm{O},\phi} = \frac{2K_{\mathrm{O}}\bar{\mathbf{h}}^{\mathrm{H}}\mathbf{R}\bar{\mathbf{h}} + \mathbf{Tr}(\mathbf{R}^2)}{M^2(1+K_{\mathrm{O}})^2}. \tag{4.23}$$

As ξ_{O} varies with ϕ, $\mathrm{E}[\xi_{\mathrm{O}}]$ can be further derived as

$$\mathrm{E}[\xi_{\mathrm{O}}] = \int_0^{2\pi} \frac{1}{2\pi}\xi_{\mathrm{O},\phi}(\kappa)\mathrm{d}\phi. \tag{4.24}$$

Theorem 4.2. *The* $\mathrm{E}[\xi_{\mathrm{O}}]$ *can be derived as an analytical expression as*

$$\mathrm{E}[\xi_{\mathrm{O}}] = \frac{1}{2\pi}\int_0^{2\pi} \frac{2K_{\mathrm{O}}\bar{\mathbf{h}}^{\mathrm{H}}\mathbf{R}\bar{\mathbf{h}} + \mathbf{Tr}(\mathbf{R}^2)}{M^2(1+K_{\mathrm{O}})^2}\mathrm{d}\phi. \tag{4.25}$$

Proof. By substituting (4.23) into (4.24), we have an analytical expression of $\mathrm{E}[\xi_{\mathrm{O}}]$ as (4.25) via straightforward derivations. □

4.3.3 Derivation of O_{CH}

Based on Theorems 1 and 2, we can derive the analytic expression of O_{CH} as follows.

By substituting (4.19) and (4.25) into (4.3), O_{CH} can be expressed as:

$$O_{\mathrm{CH}} = \frac{\sum_n^{N_{\mathrm{r}}} \frac{S_n}{X^2Y^2}\int_0^{2\pi}\left[\frac{2K_{\upsilon_n}\bar{\mathbf{h}}^{\mathrm{H}}\mathbf{R}\bar{\mathbf{h}}+\mathbf{Tr}(\mathbf{R}^2)}{M^2(1+K_{\upsilon_i})^2}W(l_n,m_n) + \frac{\mathbf{Tr}(\mathbf{R}^2)}{M^2}\left(W(Y,X)-W(l_n,m_n)\right)\right]\mathrm{d}\phi}{\frac{1}{2\pi}\int_0^{2\pi}\frac{2K_{\mathrm{O}}\bar{\mathbf{h}}^{\mathrm{H}}\mathbf{R}\bar{\mathbf{h}}+\mathbf{Tr}(\mathbf{R}^2)}{M^2(1+K_{\mathrm{O}})^2}\mathrm{d}\phi}. \tag{4.26}$$

After some straightforward derivation, we obtain the closed-form expression of O_{CH} as:

$$O_{\mathrm{CH}} = \frac{(1+K_{\mathrm{O}})^2}{2K_{\mathrm{O}}\hat{f}+1}\sum_n^{N_{\mathrm{r}}}\frac{S_n 2\pi}{X^2Y^2}\left[\frac{W(l_n,m_n)}{(1+K_{\upsilon_n})^2}(2K_{\upsilon_n}\hat{f}+1) + (W(Y,X)-W(l_n,m_n))\right], \tag{4.27}$$

where $W(a,b),(0<a<b)$ is expressed as(4.20), and $\hat{f}$ is a function of M and δ:

$$\hat{f}=\frac{M+\sum_{a=1}^{M-1}\left(2(M-a)e^{-\frac{a}{\delta}}J_0(a\pi)\right)}{M+\sum_{a=1}^{M-1}2ae^{-\frac{2(M-a)}{\delta}}}, \tag{4.28}$$

where $J_0(z)$ denotes the Bessel function of the first kind with zero order.

This chapter aims to evaluate the BUD's inherent properties, so the expression of the evaluation metric O_{CH} decoupled from the antenna number M is needed. Since we are studying the effect of the building on the Massive MIMO system, in some cases, M can be regarded as approaching infinity, then the expression of O_{CH} can still be expressed as (4.27), but with $\hat{f}$ decoupled from M as:

$$\hat{f}\to\frac{1+\sum_{a=1}^{+\infty}2e^{-\frac{a}{\delta}}J_0(a\pi)}{\coth\frac{1}{\delta}},\text{as } M\to\infty. \tag{4.29}$$

4.4 Numerical Results

For validating the model's reliability, the Monte-Carlo simulations are first performed in the single-type room layouts of N_m by N_l, where N_m by N_l denotes a room layout consisting of N_m rows and N_l columns. According to the measurement in WINNER II, K_{I} is set as 5 and K_{O} is set as 10 in all simulations and analytic calculations [35]. When spatial correlation is included, δ is set as 1, otherwise, δ is set as 0. The model is then verified in different scenarios with different parameters varying.

In every Monte-Carlo simulation, we randomly picked 10000 positions in the scene to position Txs and Rxs, respectively, and then established one-to-one communication links for them.

Fig. 4.1 shows the O_{CH} values which are associated with the number of antennas M (solid lines) and which with M tending to infinity (dashed lines), respectively, and compares them with the simulated values (scattered points) with corresponding parameter configurations.

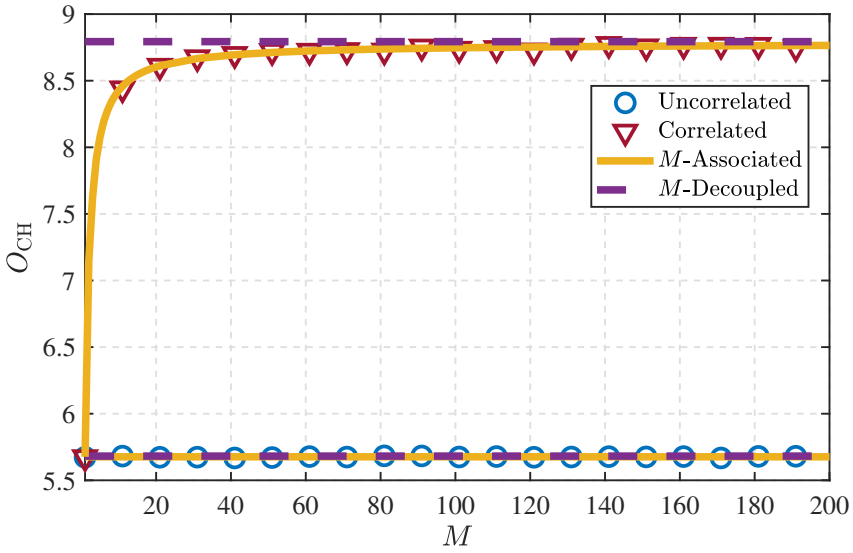

Fig. 4.1 Comparison of O_{CH} in different number of antennas M.

Firstly, the simulated values perfectly match the M-associated closed-form results. Secondly, the O_{CH} is independent of M without the inclusion of spatial correlation, regardless M taking any value. In contrast, with the inclusion of spatial correlation, the M-associated O_{CH} increases with M and begins to converge toward the M-decoupled O_{CH} value as M exceeds 150.

Figs.4.2 - 4.5 display O_{CH} in BUDs with different room layouts to verify the model in different building structures and observe the impact rule of building structures on CHO. In these simulations, the Tx antenna number M is set at 16 and 64 for comparing the relationship between M-associated O_{CH} of the different massive MIMO systems with the M-decoupled O_{CH} results.

In Fig. 4.2, the unit room shape and size are fixed (i.e., m and l are fixed as $m = 10$ m and $l = 10$ m), and the O_{CH} of BUDs with different room numbers are compared. It is obvious that when unit rooms are fixed, the number of rooms will significantly increase the O_{CH} of the BUD, and this effect is more dramatic when the spatial correlation is considered. The increase in the number of rooms significantly intensifies the NLOS probability of the channel within the BUD, so the probability that the channel behaves Rayleigh fading significantly increases, which greatly increases the randomness of the channel. In addition, the inclusion

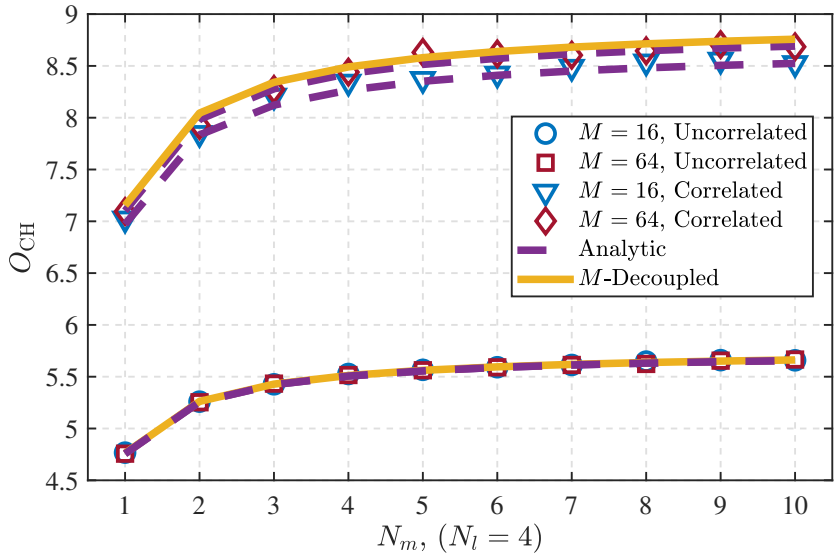

(a) Comparison of O_{CH} in scenarios with same unit room but different N_m.

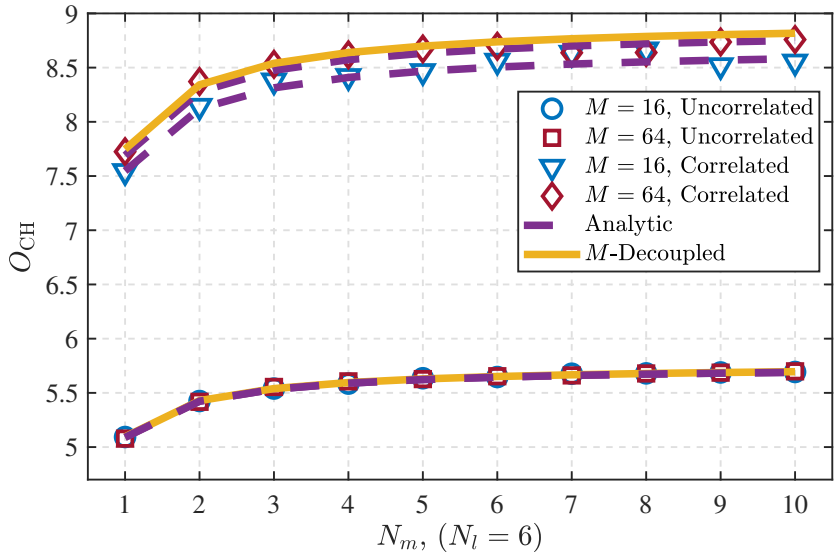

(b) Comparison of O_{CH} in scenarios with same unit room but different N_m.

Fig. 4.2 Comparison of O_{CH} in BUDs with the same unit room but different room layouts and different number of antennas M.

of spatial correlation also increases the uncertainty of the channel. Rayleigh fading channel intensifies the channel gain uncertainty caused by spatial correlation, thus making the CHO of multi-room buildings affected by the spatial correlation. Noting that different N_m and N_l may constitute the same room amounts. When comparing O_{CH} of the BUD consisting of the

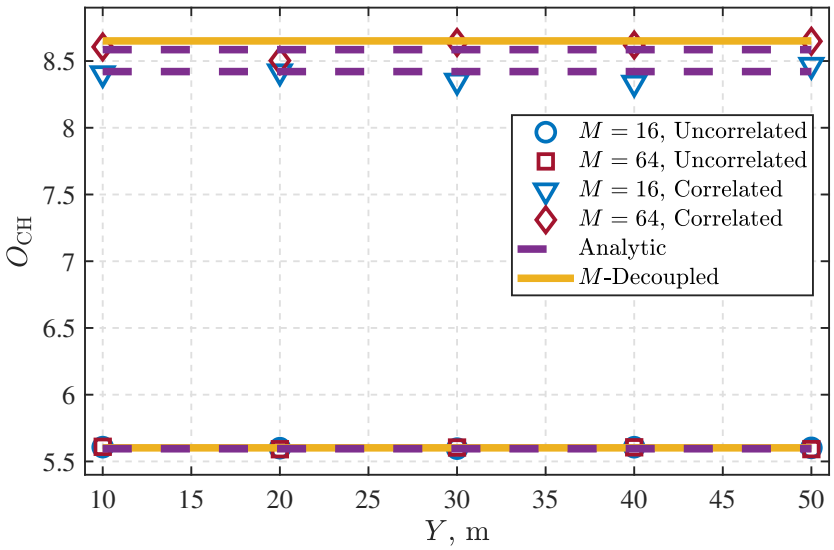

Fig. 4.3 Comparison of O_{CH} in BUDs with the same room layout but different shapes and different number of antennas M.

same number of unit rooms in different arrangements in Figs. 4.2a and 4.2b, the same O_{CH} results indicate that the room amount's influence on the CHO is not affected by the room arrangement when the unit room is fixed.

Fig. 4.3, compares CHO of scenarios with more room layout possibilities. We set the room column number $N_m = 5$, and the long side of the building $X = 100$ m. By changing the short side of the building Y, we can observe whether the shape and size of the unit rooms have an effect on the CHO when the room amount is unchanged. In Fig. 4.3, different Y leads to the same O_{CH} when other parameters remain constant. This indicates that in a single-room type building, CHO is not affected by the size and shape of the unit room, and correspondingly, BUD's size and shape, when the room arrangement (i.e., N_m and N_l) is unchanged. Figs. 4.2 and 4.3 together confirm that no matter whether the shape of the BUD changes or not, its CHO follows the changing rule with the room amount.

To explore whether the above rules can be extended to buildings with multi-type rooms, we apply the model to an indoor scenario in WINNER II A1 channel measurement and adjust the shape and size of different types of rooms. As shown in Fig. 4.4, there are two room types in the building. There are 40 rooms of type 1, whose long side is defined as m_1 and

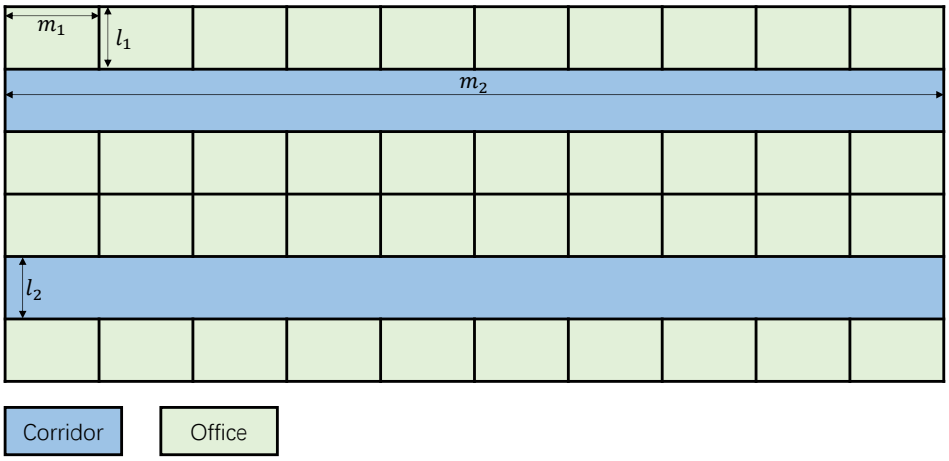

Fig. 4.4 Room layout in WINNER II indoor scenario.

the short side is defined as l_1, and 2 rooms of type 2, with the long side, defined as m_2 and the short side defined as l_2. The room arrangement mode is fixed, i.e., $m_2 = 10m_1$ is always true. In Fig. 4.5a, we fixed the length of l_1 and l_2, and compared the CHO of the building with different m_1. The figure shows that different m_1 does not affect CHO. In Figs. 4.5b and 4.5c, m_1 is fixed, and l_1 and l_2 are varying. CHO decreases with the increased l_2, but increases with the increase of l_1. Since m_2 constantly changes with m_1, different m_1 lead to the number and area ratio of type 1 and 2 rooms remaining unchanged, so CHO does not change. When m_1 is fixed and l_1 and l_2 change, the area ratio of type 1 and 2 rooms changes. Since the number of type 1 rooms is larger, CHO increases when the area proportion of type 1 rooms is larger (i.e., l_1 increases). Conversely, since there are fewer type 2 rooms, CHO decreases as type 2 rooms take up a larger area proportion (i.e., l_2 increases).

The number of antennas in current practical indoor massive MIMO systems is often limited to 4 to 128 [115]. The evaluation index CHO proposed in this chapter can evaluate the influence of buildings on the channel hardening degree of massive MIMO systems with different numbers of antennas M. In Figs.4.2 - 4.5, both M-associated O_{CH} and M-decoupled O_{CH} were calculated and compared. It can be observed that when $M = 64$, the M-associated O_{CH} values are close to the M-decoupled O_{CH} values, when $M = 16$, the M-associated O_{CH} values are lower, which is consistent with the pattern found in Fig. 4.1. Nevertheless, the numerical results in Figs.4.2 - 4.5 show that the channel hardening influence of buildings on

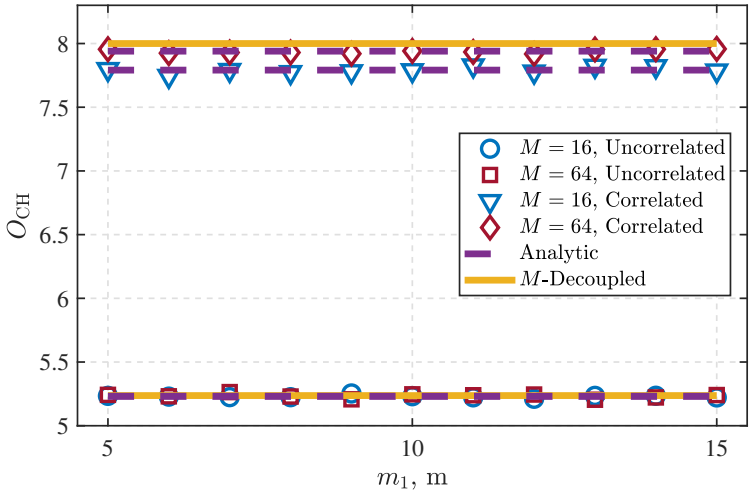

(a) Comparison of ξ in WINNER II room layout but with different m_1.

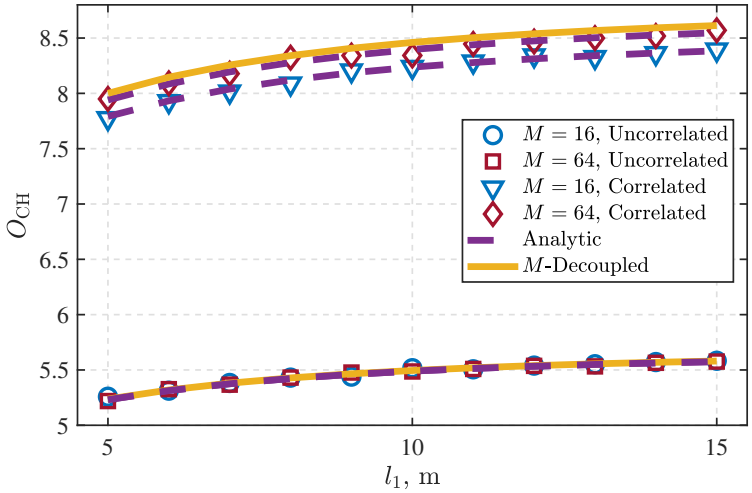

(b) Comparison of ξ in WINNER II room layout but with different l_1.

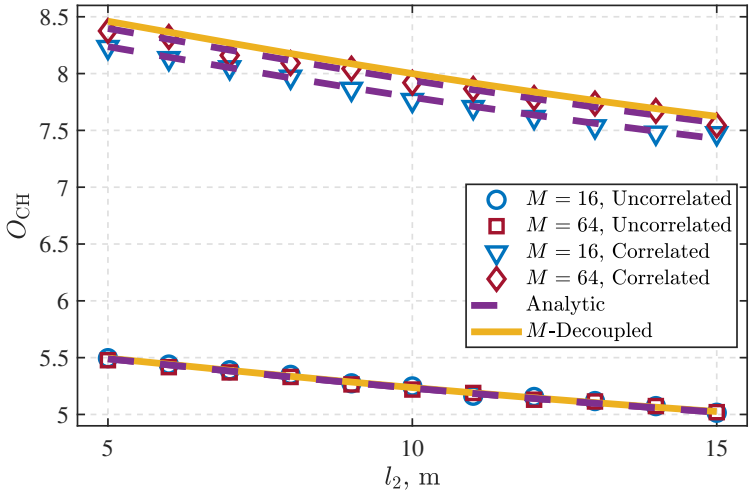

(c) Comparison of ξ in WINNER II room layout but with different l_2.

Fig. 4.5 Comparison of O_{CH} in WINNER II indoor scenarios with different number of antennas M.

massive MIMO systems with different antenna numbers shows a consistent trend. Therefore, for quickly assessing the impact of buildings on channel hardening, the M-decoupled O_{CH} expressions are more recommended in the practical application. Moreover, M-decoupled O_{CH} expressions can better reflect the BUD's inherent properties since the number of antenna M is no longer an influence factor.

Combined with the above analysis, we discover that when the building is made up of different rooms, occupying a larger floor area by the room types with fewer amounts allows the building to obtain a smaller CHO.

4.5 Conclusions

In this chapter, a novel BWP metric, CHO, was defined to help architects assess the friendliness of BUD to the channel hardening of indoor massive MIMO systems. The metric, CHO, is determined by the ratio of the average channel hardening ratios of all possible channels in the BUD, and the average channel hardening ratios of all possible channels in the same-sized open space. The analytic expression and approximation closed-form expression of the CHO were derived. The model was verified in buildings with different room arrangements. During the verification, the characteristics of building designs that are more conducive to channel hardening were summarised. The proposed BWP metric CHO will help architects design wireless-friendly buildings to enhance the reliability of the future indoor massive MIMO systems.

Chapter 5

A General BWP Evaluation Scheme for Buildings with Complex Structures

Overview

The building's interior structure is becoming the bottleneck of indoor wireless system performance as indoor wireless demand continuously increases. Quantitatively expressing how a building's interior structure impacts indoor wireless performance is vital for improving the performance of indoor wireless systems in the future. This chapter systematically presents a general BWP evaluation scheme for evaluating the influence of a building's interior layout on various wireless performance indicators. For any wireless performance indicator related to propagation distance and environment, this chapter proposes mathematical models of statistical analysis in the BUD and the same-sized open space, respectively. Furthermore, this chapter presents a fitting method for batch evaluation of buildings with irregular room shapes. The accuracy and effectiveness of the proposed scheme for different performance indicators are verified in a complex building structure. With the proposed scheme's help, architects can quickly quantify the wireless performance of their architectural designs at the designing stage, and finally, indoor wireless performance can be further improved from the perspective of architectural design.

5.1 Introduction

5.1.1 Background and Motivations

As the demand for indoor communication increases in the 5G and coming 6G era, more wireless communication technologies are introduced into indoor wireless systems to increase their capacity and reliability [7, 116–118]. However, even with the introduction of new technologies, indoor wireless performance will always be limited by other factors, among which the building structure plays a major role.

Building structures limit both the capacity and reliability of a wireless system. Compared to the outdoor wireless system, a more complex propagation environment affects signal propagation in an indoor wireless system due to the building structure [23, 67, 68, 119]. On the one hand, more blockages brought by the built environment greatly aggravate the attenuation in the signal propagation, thus reducing the SINR and the system capacity. On the other hand, indoor communications are impacted by more serious multi-path effects, resulting in larger channel DS, and leading to the reduction of coherence bandwidth and the increase of ISI, which has a negative impact on both the capacity and reliability of the wireless communication system [31, 34, 100].

The BWP evaluation has the potential to further improve indoor wireless systems' performance. The current indoor wireless system design is independent of building design, only improving the wireless system's performance in the constructed buildings [9, 31]. However, adjusting the building structure to make it more friendly to the indoor wireless system is ignored by wireless communication researchers. An intuitive and novice-friendly BWP evaluation method is urgently needed to help architects quickly assess the building design's impact on the wireless system performance at the building design stage.

5.1.2 Contributions in This Chapter

The performance indicators can affect the performance of wireless systems from various aspects but have some common characteristics, i.e., the channel hardening ratio is affected by the blockage conditions, the RSS is affected by the distance and blockage conditions

between Tx and Rx, and RMS-DS is affected not only by distance and blockage conditions, but also by the multi-path effect caused by the propagation environment.

In this chapter, the characteristics of the above performance indicators are integrated, and a more general evaluation scheme is provided for various wireless performance indicators. The proposed evaluation scheme can evaluate the BWP of building designs in terms of various wireless performance indicators. Moreover, the proposed scheme can be applied to complex building structures with rooms in irregular shapes, which is different from the assumption in the previous works in Chapters 3 and 4 that both buildings and rooms are rectangular.

5.2 General BWP Evaluation Scheme

In this section, we propose a numerical metric that can visually quantify the influence of a building structure on any performance indicator of an indoor wireless system, as long as the assessed indicator is related to Tx-Rx communication distance and propagation environments. Table 5.1 describes the main notations in this chapter.

We define the assessed indoor wireless performance indicator as x, the Tx-Rx communication distance as d, and assume that the propagation environments can be sorted into the link blockage condition as κ and the propagation condition that varies with Tx-Rx locations as η.

In order to evaluate the impact of the BUD on indicator x, we need to calculate the change of expectation value of x in the target area before and after the building is constructed. Therefore, the BWP evaluation metric of the evaluated performance indicator x can be expressed mathematically as:

$$\mathscr{X} = f(\mathrm{E}[x_{\mathrm{I}}], \mathrm{E}[x_{\mathrm{O}}]), \tag{5.1}$$

where x_{I} is the x value for any possible Tx-Rx link in the BUD, x_{O} is the x value for any possible Tx-Rx link in the open space within the same size of the BUD, and $\mathscr{X}$ is the proposed BWP evaluation metric that describe the impact of a BUD on the wireless performance indicator x. The function $f(\cdot)$ is adjustable according to the indicators. When

Table 5.1 Notation definition for Chapter 5

Notation	Description
x	The evaluated performance indicator
x_{I}	The value of x for any possible Tx-Rx link in the BUD
x_{O}	The value of x for any possible Tx-Rx link in the open space
$\mathscr{X}$	The BWP evaluation metric describing the impact of a BUD on the indicator x
P	The RSS
P_{I}	The value of P for any possible Tx-Rx link in the BUD
P_{O}	The value of P for any possible Tx-Rx link in the open space
G_P	The BWP evaluation metric PG describing the impact of a BUD on the indicator P
τ	The RMS-DS
τ_{I}	The value of τ for any possible Tx-Rx link in the BUD
τ_{O}	The value of τ for any possible Tx-Rx link in the open space
G_τ	The BWP evaluation metric DS gap describing the impact of a BUD on the indicator τ
ξ	The channel hardening ratio
ξ_{I}	Channel hardening ratio for any possible channel in the BUD
ξ_{O}	Channel hardening ratio for any possible channel in the open space
O_{CH}	The BWP evaluation metric CHO describing the impact of a BUD on the indicator ξ
d	Distance between Tx and Rx
$\mathscr{P}$	Probability of an event
p	PDF of d
p_{L}	The LOS probability of any Tx-Rx link when Tx is in the assessed region
p_{s}	The same-building probability of any Tx-Rx link when Tx is in the assessed region
κ	The set of blockage situation
η	The Tx-Rx propagation condition
υ_n	The event that the Tx is located at the n-th room
N_{r}	The amount of rooms in the BUD
S	The size of a room
n	The room number of rooms in the BUD
V	The size of the BUD
M	The number of antenna
ϕ	The angle of arrival
$\mathbf{h}$	Channel vector
K	The K-factor of the Ricean fading channel
$\mathbf{R}$	The spatial correlation matrix
δ	The correlation coefficient of $\mathbf{R}$
$\mathscr{C}$	The set of coordinates

evaluating the RSS P of the BWP, the $\mathscr{X}$ is defined as the power gain, G_P, as [31] expressed:

$$G_P = \frac{\mathrm{E}[P_\mathrm{I}]}{\mathrm{E}[P_\mathrm{O}]}. \tag{5.2}$$

When evaluating the RMS-DS of the BWP, the $\mathscr{X}$ is defined as the DS gap, G_τ, as Chapter 3 expressed:

$$G_\tau = \mathrm{E}[\tau_\mathrm{I}] - \mathrm{E}[\tau_\mathrm{O}]. \tag{5.3}$$

When evaluating the channel hardening ratio of the BWP, the $\mathscr{X}$ is defined as the CHO, O_CH, as Chapter 4 expressed:

$$O_\mathrm{CH} = \frac{\mathrm{E}[\xi_\mathrm{I}]}{\mathrm{E}[\xi_\mathrm{O}]}. \tag{5.4}$$

Considering the versatility of the proposed scheme, x depends on i) the distribution of the propagation environment between Tx and Rx, in terms of the blockage effect κ and the Tx-Rx propagation condition η, ii) the function $x(d)$ of the distance d for a given Tx-Rx link with definite channel conditions, and iii) the distribution of Tx-Rx distance d in the target area.

To decouple the BUD's inherent properties from specific deployments of indoor wireless devices, we assume that Tx and Rx are randomly distributed in the building, and thus the Tx-Rx distance d follows a specific random distribution, denoted as $p(d)$. Moreover, we assume that the propagation condition η of any Tx-Rx link only depends on the type of room in which the Tx is located, denoted as υ.

5.2.1 Mathematical Model for $\mathrm{E}[x_\mathrm{I}]$

According to the previous works in Chapters 3 and 4, $\mathrm{E}[x_\mathrm{I}]$ can be expressed as

$$\mathrm{E}[x_\mathrm{I}] = \sum_{n}^{N_\mathrm{r}} \frac{S_n}{V} \sum_{\kappa} \int_0^{+\infty} p(d) x_{\upsilon_n,\kappa}(d) \mathscr{P}_{\upsilon_n}(\kappa|d) \mathrm{d}d, \tag{5.5}$$

where $\mathscr{P}(\cdot)$ denotes the probability of an event, $\kappa \in \{\text{LOS}, \text{NLOS}\}$ denotes the blockage condition, υ_n denotes the room type of the n-th room that Tx locates in the BUD, S_n denotes the area of the n-th room in the BUD and V denotes the total area of the BUD.

For different wireless performance indicator x, we can obtain different expressions of $x_{\upsilon_n,\kappa}(d)$. As illustrated from (5.5), the analytical solution of $\mathrm{E}[x_{\mathrm{I}}]$ can then be obtained as long as we obtain of $p(d)$ and $\mathscr{P}_{\upsilon_n}(\kappa|d)$.

In the previous works in Chapters 3 and 4, $\mathscr{P}_{\upsilon_n,\chi}(\kappa|d)$ and $p(d)$ have been derived in the rectangular room and BUD, which will be extended to any arbitrary shape in this chapter. For a room n whose floor projection is in arbitrary shape in a BUD whose floor projection is another arbitrary shape, it has $\mathscr{P}_{\upsilon_n,d}(\kappa|\chi)$ as

$$\mathscr{P}_{\upsilon_n,\chi}(\kappa|d) = \begin{cases} \frac{p_{\mathrm{L},n}(d)}{p_{\mathrm{s,BUD}}(d)}, & \text{LOS}, \\ 1 - \frac{p_{\mathrm{L},n}(d)}{p_{\mathrm{s,BUD}}(d)}, & \text{NLOS}, \end{cases} \tag{5.6}$$

where $p_{\mathrm{L},n}(d)$ denotes the LOS probability of any Tx-Rx link, when Tx is in the room n and the Tx-Rx distance is d; and $p_{\mathrm{s,BUD}}(d)$ denotes the same-building probability of any Tx-Rx link, when Tx is in the BUD and the Tx-Rx distance is d.

For the BUD whose floor projection is any arbitrary shape, the Tx-Rx distance distribution in the BUD $p(d)$ can be calculated as

$$p(d) = \frac{2\pi d p_{\mathrm{s,BUD}}(d)}{V}. \tag{5.7}$$

By substituting (5.6) and (5.7) into (5.5), the final analytical expression of $\mathrm{E}[x_{\mathrm{I}}]$ can be derived as:

$$\mathrm{E}[x_{\mathrm{I}}] = \sum_{n}^{N_{\mathrm{r}}} \frac{2\pi d S_n}{V^2} \int_0^{+\infty} (x_{\upsilon_n,\mathrm{LOS}}(d) p_{\mathrm{L},n}(d) + x_{\upsilon_n,\mathrm{NLOS}}(d) p_{\mathrm{s,BUD}}(d) - x_{\upsilon_n,\mathrm{NLOS}} p_{\mathrm{L},n}(d)) \mathrm{d}d. \tag{5.8}$$

5.2.2 Mathematical Model for $\mathrm{E}[x_{\mathrm{O}}]$

Similar to the derivation of $\mathrm{E}[x_{\mathrm{I}}]$, $\mathrm{E}[x_{\mathrm{O}}]$ can be expressed as

$$\mathrm{E}[x_{\mathrm{O}}] = \int_0^{+\infty} p(d) x_{\mathrm{O,LOS}}(d) \mathrm{d}d. \tag{5.9}$$

By substituting (3.23) into (5.9), the final analytical expression of $\mathrm{E}[x_{\mathrm{O}}]$ can be derived as

$$\mathrm{E}[x_{\mathrm{O}}] = \frac{2\pi}{V} \int_0^{+\infty} d p_{\mathrm{s,BUD}}(d) x_{\mathrm{O,LOS}}(d) \mathrm{d}d. \tag{5.10}$$

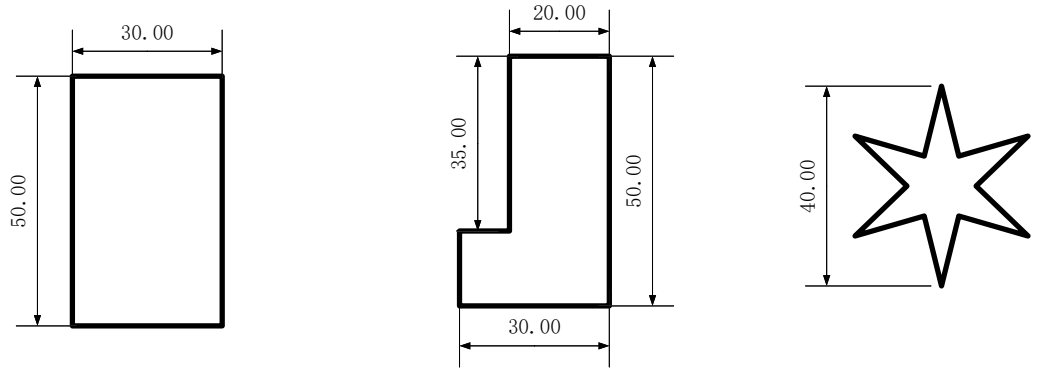

(a) A rectangular room A. (b) A corner room B. (c) A hexagonal star room C.

Fig. 5.1 Rooms with different irregular shapes (unit: m).

5.3 Approximation for Rooms and BUD in Arbitrary Shapes

For any arbitrary shape, we can find functions $p_{\mathrm{L}}(d)$ or $p_{\mathrm{s}}(d)$ of the room/BUD via the polynomial fitting method. First, we use the Monte-Carlo method to simulate $p_{\mathrm{L},0}(d)$ and $p_{\mathrm{s},0}(d)$ of different d for Tx at any random location in a reference room/BUD with the target shape. $p_{\mathrm{L}}(d)$ or $p_{\mathrm{s}}(d)$ are in the range of $[0,1]$, but using polynomial fitting does not guarantee that the fitted function will always be no less than 0. Therefore, we polynomial fit the logarithm of $p_{\mathrm{L},0}(d)$ and $p_{\mathrm{s},0}(d)$ to ensure the non-negative of the fitting function.

When using polynomial fitting, the higher the degree of the polynomial, the higher the accuracy of the fitted function. As the degree increases, the RMSE decreases, while the time

required for polynomial fitting does not significantly increase with higher degrees. Therefore, using a higher number of terms for polynomial fitting can effectively ensure accuracy as long as the polynomial coefficients can be stored. Consequently, this chapter uses the maximum degree of 9 for polynomial fitting, for it is the maximum degree used in MATLAB's fast polynomial fitting function.

Therefore, $p_{\mathrm{L},0}(d)$ and $p_{\mathrm{s},0}(d)$ can be polynomially fitted as:

$$\ln(p_{\mathrm{L},0}(d)) = \begin{cases} \sum_{m=0}^{9} a_m d^m, & 0 < d \leq d_{\max}, \\ -\infty, & d > d_{\max}, \end{cases} \tag{5.11}$$

and

$$\ln(p_{\mathrm{s},0}(d)) = \begin{cases} \sum_{m=0}^{9} b_m d^m, & 0 < d \leq d_{\max}, \\ -\infty, & d > d_{\max}, \end{cases} \tag{5.12}$$

where $d_{\max}$ denotes the maximum possible distance of the Tx-Rx link when Tx and Rx are both located in the target room/BUD. Therefore, the fitting function of $p_{\mathrm{L}}(d)$ or $p_{\mathrm{s}}(d)$ can be expressed as:

$$\tilde{p_{\mathrm{L}}}(d) = \begin{cases} \exp(\sum_{m=0}^{9} a_m d^m), & 0 < d \leq d_{\max}, \\ 0, & d > d_{\max}, \end{cases} \tag{5.13}$$

and

$$\tilde{p_{\mathrm{s}}}(d) = \begin{cases} \exp(\sum_{m=0}^{9} b_m d^m), & 0 < d \leq d_{\max}, \\ 0, & d > d_{\max}. \end{cases} \tag{5.14}$$

In a room with a fully convex shape, the link between a randomly locating Tx and a randomly locating Rx is always LOS, i.e.,

$$p_{\mathrm{L}}(d) = p_{\mathrm{s}}(d). \tag{5.15}$$

To further simplify the computation, we simplify the derivation of $p_{\mathrm{L}}(d)$ and $p_{\mathrm{s}}(d)$ functions for rooms with the same shape but different sizes. For a room n whose size and shape are given and whose $\tilde{p}_{\mathrm{L},n}(d)$ or $\tilde{p}_{\mathrm{s},n}(d)$ has been derived, the $\tilde{p}_{\mathrm{L},m}(d)$ or $\tilde{p}_{\mathrm{s},m}(d)$ of a room m whose shape is the same as the room n and room area is k times of the room n can be directly expressed as:

$$\tilde{p}_{\mathrm{L},m}(d) = \tilde{p}_{\mathrm{L},n}(d\sqrt{k}), \tag{5.16}$$

$$\tilde{p}_{\mathrm{s},m}(d) = \tilde{p}_{\mathrm{s},n}(d\sqrt{k}). \tag{5.17}$$

5.4 Verification

In order to verify the accuracy of the polynomial fitting, $p_{\mathrm{L}}(d)$ and $p_{\mathrm{s}}(d)$ are simulated and fitted in rooms with rectangular, corner, and hexagonal star shapes respectively. The shapes and sizes of the target rooms are shown in Figs. 5.1a,5.1b, and 5.1c, and hereinafter the rooms are referred to as room A, B and C, respectively. In the simulation, for any Tx-Rx distance d, ($d \in [0, d_{\max}]$), we randomly select a position in the room as Tx and randomly select an angel θ, ($\theta \in [0, 2\pi]$), to locate the Rx that is d far from Tx via its polar coordination. The fitting parameters of $\tilde{p}_{\mathrm{L},R}(d)$ and $\tilde{p}_{\mathrm{s},R}(d)$ ($R \in \{\mathrm{A}, \mathrm{B}, \mathrm{C}\}$) for room A, B, and C are listed in Tables 5.2 and 5.3.

In Fig. 5.2, we compare $p_{\mathrm{L},R,0}(d)$ and $p_{\mathrm{s},R,0}(d)$ and their fitting functions $\tilde{p}_{\mathrm{L},R}(d)$ and $\tilde{p}_{\mathrm{s},R}(d)$ in the target rooms. Moreover, we simulate and fit $\tilde{p}_{\mathrm{L},r}(d)$ and $\tilde{p}_{\mathrm{s},r}(d)$ ($r \in \{\mathrm{a}, \mathrm{b}, \mathrm{c}\}$) in rooms with the same shape but 0.25 times area of the original room A, B and C, denoted as room a, b and c, and compare the difference between $\tilde{p}_{\mathrm{L},R}(d)$, $\tilde{p}_{\mathrm{s},R}(d)$, $\tilde{p}_{\mathrm{L},r}(d/2)$ and $\tilde{p}_{\mathrm{s},r}(d/2)$.

It can be seen in Fig. 5.2a that for room A, as a convex rectangular room, the simulation values of $p_{\mathrm{L,A},0}(d)$ and $p_{\mathrm{s,A},0}(d)$ are constantly equal. Moreover, the fitting function $\tilde{p}_{\mathrm{L},A}(d)$ fits the simulation value $p_{\mathrm{L,A},0}(d)$ perfectly, and shows no different from the analytical Z function that referred from [67]. This figure shows that the accuracy of the fitting functions derived by the polynomial fitting method is sufficient for the analytical solutions. Moreover,

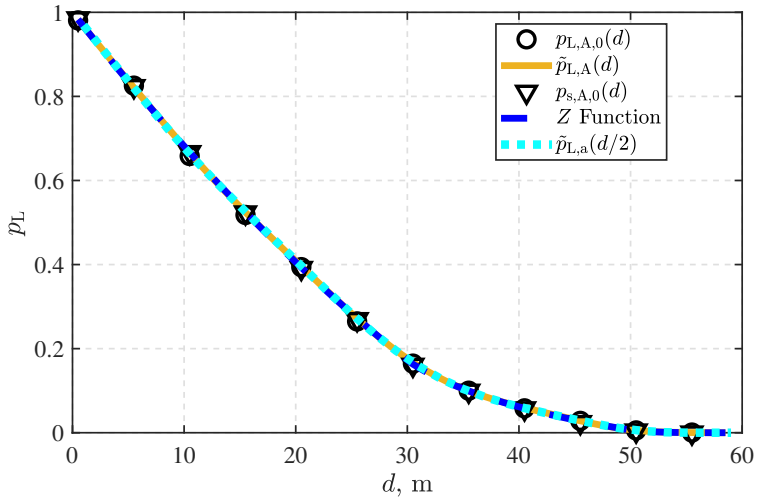

(a) Comparison of p_{L} and p_{s} and $Z(d,50,30)$ in room A.

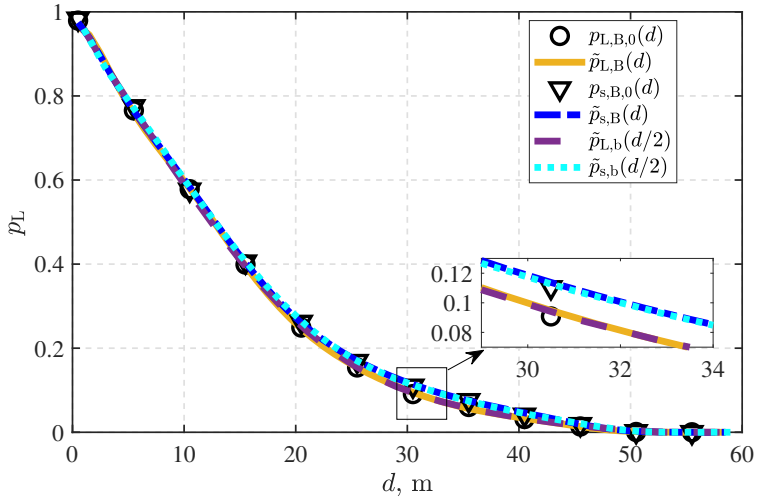

(b) Comparison of p_{L} and p_{s} in room B.

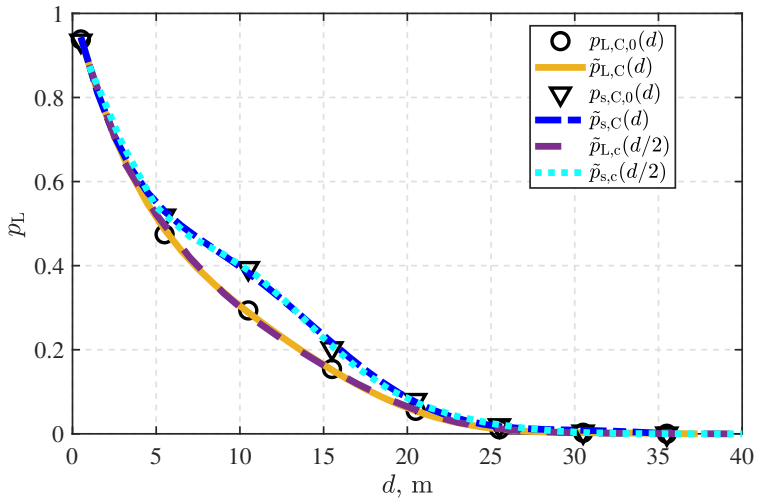

(c) Comparison of p_{L} and p_{s} in room C.

Fig. 5.2 Comparison of p_{L} and p_{s} in rooms with different shapes.

Table 5.2 Fitting Parameters for p_{L}

p_{L}	A	B	C
a_9	2.33×10^{-13}	7.15×10^{-13}	8.31×10^{-12}
a_8	-5.25×10^{-11}	-1.58×10^{-10}	-1.88×10^{-9}
a_7	4.72×10^{-9}	1.45×10^{-8}	1.56×10^{-7}
a_6	-2.26×10^{-7}	-7.23×10^{-7}	-6.56×10^{-6}
a_5	6.36×10^{-6}	2.11×10^{-5}	1.55×10^{-4}
a_4	-1.09×10^{-4}	-3.62×10^{-4}	-2.11×10^{-3}
a_3	1.08×10^{-3}	3.50×10^{-3}	1.60×10^{-2}
a_2	-6.17×10^{-3}	-1.82×10^{-2}	-5.72×10^{-2}
a_1	-2.06×10^{-2}	-6.10×10^{-3}	-5.49×10^{-2}
a_0	-7.78×10^{-3}	-1.94×10^{-2}	-2.75×10^{-2}

Table 5.3 Fitting Parameters for p_{s}

p_{s}	A	B	C
b_9	2.33×10^{-13}	8.86×10^{-13}	-1.74×10^{-11}
b_8	-5.25×10^{-11}	-2.03×10^{-10}	2.30×10^{-9}
b_7	4.72×10^{-9}	1.94×10^{-8}	-1.15×10^{-7}
b_6	-2.26×10^{-7}	-1.00×10^{-6}	2.39×10^{-6}
b_5	6.36×10^{-6}	3.03×10^{-5}	-5.48×10^{-6}
b_4	-1.09×10^{-4}	-5.39×10^{-4}	-5.92×10^{-4}
b_3	1.08×10^{-3}	5.43×10^{-3}	8.87×10^{-3}
b_2	-6.17×10^{-3}	-2.91×10^{-2}	-4.11×10^{-2}
b_1	-2.06×10^{-2}	1.99×10^{-2}	-6.11×10^{-2}
b_0	-7.78×10^{-3}	-3.67×10^{-2}	-3.03×10^{-2}

the matching of $\tilde{p}_{\mathrm{L},A}(d)$ and $\tilde{p}_{\mathrm{L},a}(d/2)$ proves that by simple function transformation, we can obtain the $\tilde{p}_{\mathrm{L}}(d)$ of rooms with the same shape but different scaling ratio by simulating and fitting one typical room.

In Fig. 5.2b and Fig. 5.2c, rooms B and C, whose shapes are irregular and analytical solutions of $p_{\mathrm{L}}(d)$ or $p_{\mathrm{s}}(d)$ are hard to be derived, are simulated. Moreover, their fitting functions of $\tilde{p}_{\mathrm{L},R}(d)$ and $\tilde{p}_{\mathrm{s},R}(d)$ are derived and compared with $\tilde{p}_{\mathrm{L},r}(d/2)$ and $\tilde{p}_{\mathrm{s},r}(d/2)$. These two figures show that for any arbitrary shape, the $\tilde{p_{\mathrm{L}}}(d)$ and $\tilde{p_{\mathrm{s}}}(d)$ derived via the polynomial fitting method can perfectly match the simulation results. The difference between $\tilde{p_{\mathrm{L}}}(d)$ and $\tilde{p_{\mathrm{s}}}(d)$ proves that for non-convex shaped rooms, $\tilde{p_{\mathrm{L}}}(d)$ and $\tilde{p_{\mathrm{s}}}(d)$ need to be

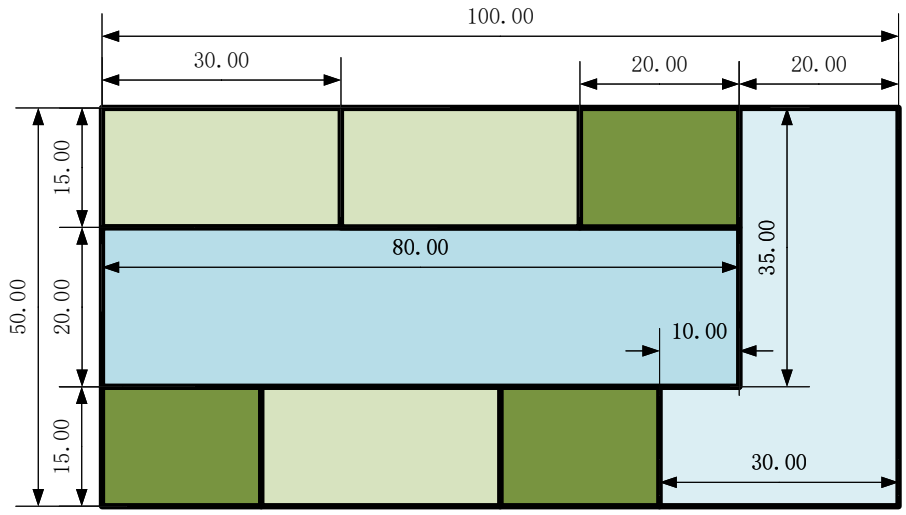

Fig. 5.3 A BUD with rectangular offices (in green), a rectangular corridor and a corner corridor (in blue) (unit: m).

derived separately, and $\tilde{p_s}(d)$ is never less than $\tilde{p_s}(d)$. The more concave the shape of a room (such as room C), the greater the gap between $\tilde{p_L}(d)$ and $\tilde{p_s}(d)$. The perfect match between $\tilde{p}_{L,R}(d)$ and $\tilde{p}_{L,r}(d/2)$, $\tilde{p}_{s,R}(d)$ and $\tilde{p}_{s,r}(d/2)$, shows that for any room shape, the $\tilde{p_L}(d)$ and $\tilde{p_s}(d)$ of its scaled room can be quickly obtained via a simple function transformation.

To verify the universality of the evaluation system, we use the Monte-Carlo method to simulate the RSS P, RMS-DS τ_{rms} and the channel hardening ratio ξ of Tx-Rx links in a BUD of a room layout with an irregularly shaped room, and apply the proposed scheme for quick calculation of G_P, $G_{\tau_{\text{rms}}}$ and O_{CH} as the corresponding BWP metrics.

$P_{\upsilon_n,\kappa}(d)$ and $P_{\text{O}}(d)$ can be modelled according to the practical measurements in WINNER II [35] as

$$P_{\upsilon_n,\kappa}(d) = 10^{\frac{P_\Gamma(\text{dB}) - A_{\upsilon_n,\kappa}\log_{10}(d) - B_{\upsilon_n,\kappa} - C_{\upsilon_n,\kappa}\log_{10}(\frac{f_c(\text{GHz})}{5}) - X_{\upsilon_n,\kappa}}{10}}, \tag{5.18}$$

$$P_{\text{O}}(d) = 10^{\frac{P_\Gamma(\text{dB})}{10} - 2\log_{10}(d) - 4.64 - 2\log_{10}(\frac{f_c(\text{GHz})}{5})}, \tag{5.19}$$

where f_c denotes the carrier frequency, and values of parameters $A_{\upsilon_n,\kappa}$, $B_{\upsilon_n,\kappa}$, $C_{\upsilon_n,\kappa}$ and $X_{\upsilon_n,\kappa}$ vary according to the κ and υ_n. In this chapter, the parameter values for different κ and υ_n in [35] are employed. Then by substituting (5.19) an (5.18) as the target evaluation indicator x_{I}

and x_{O} into (5.8), (5.10), and (5.2), the G_P as the metric for evaluating the BWP in terms of the received power strength of the whole BUD can be derived.

According to the previous work in Chapter 3, $\tau_{\upsilon_n,\kappa}(d)$ show further randomness. Therefore, we need to calculate the expectation values of RMS-DS of links with different distances and transmission conditions as $\mu_{\tau,\upsilon_n,\kappa}$, i.e.:

$$\mu_{\tau,\upsilon_n,\kappa}(d)=\int_0^{+\infty}\tau_{\mathrm{I}}\frac{\exp\left(-\frac{1}{2}\left(\frac{\tau_{\mathrm{I}}-\mu_{\kappa_n,\upsilon,\tau_{\mathrm{I}}}(d)}{\sigma_{\kappa_n,\upsilon,\tau_{\mathrm{I}}}}\right)^2\right)}{\sqrt{2\pi}\sigma_{\kappa_n,\upsilon,\tau_{\mathrm{I}}}}\mathrm{d}\tau_{\mathrm{I}}, \tag{5.20}$$

while the $\tau_{\mathrm{O}}(d)$ calculated in the two-ray model does not exhibit this randomness, therefore $\mu_{\tau,\mathrm{O}}(d)$ is the same as $\tau_{\mathrm{O}}(d)$:

$$\begin{aligned}\mu_{\tau,\mathrm{O}}(d)=&\tau_{\mathrm{O}}(d)=\frac{\sqrt{d^2+(h_{\mathrm{T}}-h_{\mathrm{R}})^2}\left(\sqrt{\frac{d^2h_{\mathrm{R}}^2}{(h_{\mathrm{R}}+h_{\mathrm{T}})^2}+h_{\mathrm{R}}^2}+\sqrt{\frac{d^2h_{\mathrm{T}}^2}{(h_{\mathrm{R}}+h_{\mathrm{T}})^2}+h_{\mathrm{T}}^2}\right)}{c\left(\left(\sqrt{\frac{d^2h_{\mathrm{R}}^2}{(h_{\mathrm{R}}+h_{\mathrm{T}})^2}+h_{\mathrm{R}}^2}+\sqrt{\frac{d^2h_{\mathrm{T}}^2}{(h_{\mathrm{R}}+h_{\mathrm{T}})^2}+h_{\mathrm{T}}^2}\right)^2+d^2+(h_{\mathrm{T}}-h_{\mathrm{R}})^2\right)}\\&\times\left(\sqrt{\frac{d^2h_{\mathrm{R}}^2}{(h_{\mathrm{R}}+h_{\mathrm{T}})^2}+h_{\mathrm{R}}^2}+\sqrt{\frac{d^2h_{\mathrm{T}}^2}{(h_{\mathrm{R}}+h_{\mathrm{T}})^2}+h_{\mathrm{T}}^2}-\sqrt{d^2+(h_{\mathrm{T}}-h_{\mathrm{R}})^2}\right).\end{aligned} \tag{5.21}$$

Then by substituting $\mu_{\tau,\upsilon_n,\kappa}$ and $\mu_{\tau,\mathrm{O}}$ as the target evaluation indicator x to (5.8), (5.10) and (5.3), the G_τ as the metric for evaluating the BWP in terms of the RMS-DS of the whole BUD can be derived.

According to the previous work in Chapter 4, the channel hardening ratio varies with the blockage condition and the propagation environment. Using the same configuration as Chapter 4, the $\xi_I(\kappa)$ and ξ_O can be calculated according to (4.12) and (4.22):

$$\xi_{\upsilon_n}(\kappa)=\int_0^{2\pi}\frac{2K_{\upsilon_n}(\kappa)\bar{\mathbf{h}}^{\mathrm{H}}\mathbf{R}\bar{\mathbf{h}}+\mathbf{Tr}(\mathbf{R}^2)}{2\pi M^2(1+K_{\upsilon_n}(\kappa))^2}\mathrm{d}\phi, \tag{5.22}$$

$$\xi_{\mathrm{O}}=\int_0^{2\pi}\frac{2K_{\mathrm{O}}\bar{\mathbf{h}}^{\mathrm{H}}\mathbf{R}\bar{\mathbf{h}}+\mathbf{Tr}(\mathbf{R}^2)}{2\pi M^2(1+K_{\mathrm{O}})^2}\mathrm{d}\phi, \tag{5.23}$$

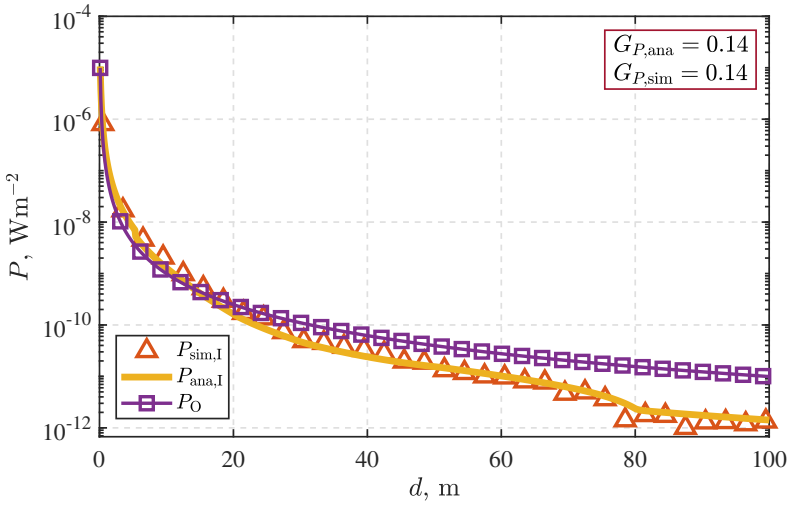

(a) Comparison of the simulated and analytic P at different d in the BUD.

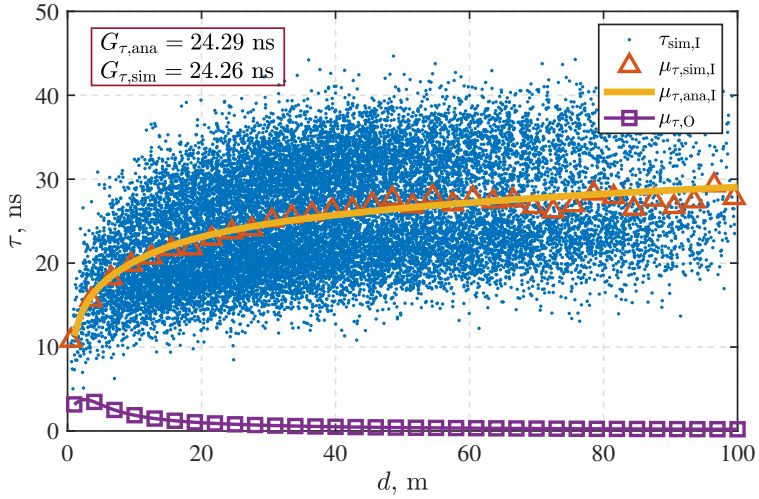

(b) Comparison of the simulated and analytic τ_{rms} at different d in the BUD.

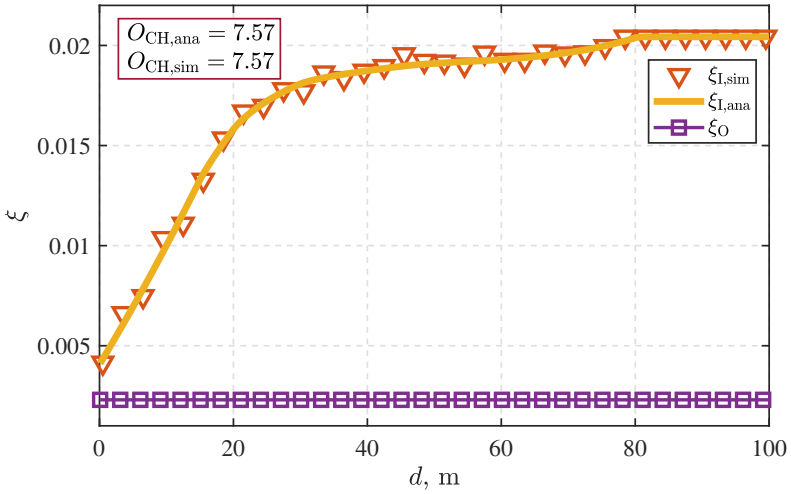

(c) Comparison of the simulated and analytic ξ at different d in the BUD.

Fig. 5.4 Examples for BWP evaluation of different indicators in a complex building structure. The final simulation and analytic results of BWP metrics G_P, G_τ and O_{CH} are shown and compared in the red box in each figure.

where

$$\overline{\mathbf{h}} = \left[1, e^{j\pi\sin\phi}, ..., e^{j(M-1)\pi\sin\phi}\right]^T, \tag{5.24}$$

and the semi-definite matrix $\mathbf{R}$ and values of parameter $K_{\upsilon_n}(\kappa)$ and K_{O} is set as the same as in Chapter 4. Then by substituting (5.22) and (5.23) as the target evaluation indicator x_{I} and x_{O} into (5.8), (5.10), and (5.4), the O_{CH} as the metric for evaluating the BWP in terms of the channel hardening ratio of the whole BUD can be derived.

Fig. 5.3 shows the layout and size of the simulated BUD. The simulated BUD has two room types: office and corridor, marked in green and blue. The colours for different sizes of rooms differ. One of the corridors has an irregular shape, whose shape and size are the same as room B in Fig. 5.1b. Therefore, $\tilde{p}_{\mathrm{L},B}(d)$ is substituted as its fitting function of p_{L} to calculate the analytical result of G_P, G_τ and O_{CH}.

Fig. 5.4 compares the simulated and analytic results of target indicators in the BUD. In the simulation, 20000 positions of Tx and Rx are randomly generated in the BUD and the same-sized open space. Moreover, P, τ and ξ of every link are simulated individually, denoted as $P_{\mathrm{sim,I}}$, $\tau_{\mathrm{sim,I}}$ and $\xi_{\mathrm{sim,I}}$ for indoor scenarios, and $P_{\mathrm{sim,O}}$, $\tau_{\mathrm{sim,O}}$ and $\xi_{\mathrm{sim,O}}$ for outdoor scenarios. When simulating $P_{\mathrm{sim,I}}$ and $P_{\mathrm{sim,O}}$, the transmitting power is set as -30 dBWm^{-2} and the carrier frequency is set as 2.4 GHz.

In Fig. 5.4a, $P_{\mathrm{sim,I}}$ is compared with the analytical results $P_{\mathrm{ana,I}}$. At the same time, the variation of P_{O} is plotted as the reference. The simulated result and the analytic result of G_P are also computed and shown in Fig. 5.4a.

In Fig. 5.4b, to summarise the statistical characteristics of $\tau_{\mathrm{sim,I}}$, the expectation value of $\tau_{\mathrm{sim,I}}$ at different d is statistically analysed, denoted as $\mu_{\tau,\mathrm{I}}$ and is compared with the analytical results $\mu_{\tau,\mathrm{ana,I}}$. In addition, a 2-ray model was utilised to evaluate the RMS-DS performance of the open space as the reference, whose variation with distance d was expressed by τ_{O} in Fig. 5.4b. Finally, the simulated result and the analytic result of G_τ are also computed and shown in Fig. 5.4b.

In Fig. 5.4c, $\xi_{\mathrm{sim,I}}$ is compared with the analytical results $\xi_{\mathrm{ana,I}}$. At the same time, the variation of ξ_{O} is plotted as the reference. The simulated result and the analytic result of O_{CH} are also computed and shown in Fig. 5.4c.

In Fig. 5.4, the high consistency between the analytical results and the simulation results of different BWP metrics validates the accuracy of the proposed BWP evaluation scheme. Moreover, in the validation, obtaining $G_{P,\mathrm{sim}}$ took 0.50 s, obtaining $G_{\tau,\mathrm{sim}}$ took 0.43 s, and obtaining $O_{\mathrm{CH,sim}}$ took 0.35 s, while calculating $G_{P,\mathrm{ana}}$, $G_{\tau,\mathrm{ana}}$ and $O_{\mathrm{CH,ana}}$ only took 0.01 s respectively. Comparing the simulation with analytical results, by simulating and function fitting for a single irregular room, the wireless performance of a building can be evaluated more quickly, and the random deviation caused by the Monte-Carlo method can also be eliminated. At the same time, the fitted p_{L} and p_{s} functions of a single irregularly shaped room can be reused without re-simulation, further simplifying the computational effort of evaluating a large amount of complex BUD.

5.5 Conclusions

This chapter proposed a general BWP evaluation model for more complex architectural structures to statistically evaluate building structures' impact on various indoor wireless systems' performance indicators. Firstly, the general statistical functions of wireless system performance indicators in a BUD and same-sized open space were derived, respectively, and the mathematical models of BWP evaluation metrics were defined. Secondly, a fitting method and fitting functions were proposed for the LOS probability and same-building probability of Tx-Rx links in complex building structures with irregularly shaped rooms. Finally, simulating the RSS, RMS-DS and channel hardening ratio as examples of different performance indicators for an architectural design with irregular rooms verified the accuracy and effectiveness of the proposed scheme. Introducing this scheme into construction practices can effectively help architects quickly evaluate different wireless performance indicators of building design to improve the performance of future indoor wireless systems.

Chapter 6

Conclusions and Future Works

6.1 Conclusions

This thesis focused on improving indoor wireless systems' performance from the architectural design perspective. This thesis considered the impact of building structures on indoor wireless system performance and defines the impact on different wireless performance indicators as different BWP metrics. To assist the architects in designing a multi-factorial balanced building that considers but is not limited to wireless performance, the wireless performance of the building should be described as statistically and intuitively as possible. Therefore, this thesis aimed to establish a BWP evaluation system in which each defined BWP metric can describe the statistical value of one wireless performance indicator of a building design. Using this evaluation scheme, architects can determine the direction of improvement of their building design based on simple changes in metric values without comprehending the actual wireless system performance.

Complex indoor building structures can cause different multipath effects on communication links, thus affecting system capacity and stability, which has yet to be mentioned in BWP studies. As performance indicators reflecting the multipath effect, the delay spread and channel hardening are related to the actual wireless systems performance. A larger RMS-DS will increase ISI and BER, while a higher channel hardening ratio can reduce ISI and improve system reliability. Therefore, in the design of the indoor wireless system, factors such as

delay spread and channel hardening should be considered comprehensively to optimise the system's performance.

This thesis selects RMS-DS and channel hardening ratio as the wireless performance indicators to be evaluated. In Chapter 3 and Chapter 4, the influence of rectangular single-storey buildings with rectangular rooms on the target wireless performance indicators is discussed respectively. The corresponding BWP evaluation indexes DS gap and CHO are proposed, and the corresponding evaluation methods are also detailed. Comparing the DS gap and CHO values of different architectural designs proves that different architectural designs have different wireless friendliness. The evaluation system is expanded and improved in Chapter 5. The evaluation system can introduce any wireless performance indicator affected by the communication environment. The buildings to be evaluated are also expanded from rectangular buildings with rectangular rooms to single-storey buildings with arbitrary shapes.

The research in this thesis greatly expands the potential application scenarios of building wireless performance evaluation. The research results and methods in this thesis provide an essential foundation for architects and engineers to improve the performance of indoor wireless systems in the next generation of intelligent buildings. Considering factors such as the multipath effect and system reliability in BWP evaluation, the BWP evaluation system developed in this thesis can help architects make wise decisions in building design. The insights gained from this thesis contribute to the advancement of wireless communication in indoor environments, helping to overcome the challenges posed by building structures and improving the overall performance of wireless systems. This thesis sets the stage for future developments in wireless communication. It lays a solid groundwork for designing and optimising 6G smart buildings, leading to enhanced user experiences and seamless connectivity in the era of advanced wireless technologies.

6.2 Future Works

This thesis introduces a systematic BWP metric definition framework that can incorporate wireless performance indicators into architectural design evaluation. Some open issues remain in the proposed BWP evaluation system for future studies.

First, the current estimation of BWP metrics is based on a combination of empirical and statistical models, which can help architects quickly determine the friendliness of building structures to indoor wireless system performance. However, using these indicators to predict the specific performance of indoor wireless communication systems remains to be realised. In future work, specific indoor communication networks will be built in various building structures to collect data on network performance indicators in these buildings, such as inter-symbol interference (ISI), bit error rate (BER), signal strength, and throughput. The BWP indicators of these building structures will also be evaluated. The relationship between the corresponding BWP evaluation indicators and actual wireless performance will be mapped and studied.

Second, the proposed BWP evaluation models in the thesis are for evaluating single-layer BWP. It will be extended to a three-dimensional BWP evaluation model in the future, taking the impact of floor on system performance into account. In addition, the effect of multiple walls on wireless propagations will also be included in the evaluation scheme and distinguished from the effect of the single wall. Further, the materials of the walls and floors will also be introduced as variables in the BWP evaluation scheme.

Third, in addition to receiving signals from indoor wireless systems, indoor mobile communication also relies on services from outdoor macrocell BSs, from which the signal transmission is also affected by building structures. The current BWP evaluation gives priority to how indoor wireless systems are influenced by building structures. Future BWP evaluations require a similar evaluation framework to evaluate the architectural impact on various indicators of indoor wireless performance generated by outdoor wireless networks.

References

[1] Huawei, “The future of mobile broadband - industry insight in Huawei,” Mar. 2017. [Online]. Available: https://www.huawei.com/en/huaweitech/industry-insights/outlook/mobile-broadband/insights-reports/the-future-of-mobile-broadband

[2] Oculus, “Virtual reality set to make mainstream breakthrough,” Mar. 2016. [Online]. Available: https://www.cbsnews.com/sanfrancisco/news/virtual-reality-set-to-make-mainstream-breakthrough/

[3] Huawei, “Huawei releases AR white paper and elaborates on benefits of 5G + AR,” Jun. 2021. [Online]. Available: https://www.huawei.com/en/news/2021/6/5g-ar-huawei

[4] Qualcomm, “The mobile future of extended reality - Qualcomm,” Mar. 2017. [Online]. Available: https://www.qualcomm.com/content/dam/qcomm-martech/dm-assets/documents/awe_2017_-_the_mobile_future_of_extended_reality_-for_pdf_1.pdf

[5] Ericsson, “Ericsson mobility report november 2022,” Jan. 2023. [Online]. Available: https://www.ericsson.com/en/reports-and-papers/mobility-report/reports/november-2022

[6] Cisco, “Cisco vision: 5G whitepaper summary.” [Online]. Available: https://www.cisco.com/c/dam/en/us/solutions/collateral/service-provider/ultra-services-platform/5g-ran-indoor.pdf

[7] X. Ge, S. Tu, G. Mao, C.-X. Wang, and T. Han, “5G ultra-dense cellular networks,” *IEEE Wireless Commun.*, vol. 23, no. 1, pp. 72–79, Feb. 2016.

[8] H. Jiang, C. Cai, X. Ma, Y. Yang, and J. Liu, "Smart home based on WiFi sensing: A survey," *IEEE Access*, vol. 6, pp. 13 317–13 325, Mar. 2018.

[9] T. Nam and T. A. Pardo, "Conceptualizing smart city with dimensions of technology, people, and institutions," in *Proceedings of the 12th annual international digital government research conference: digital government innovation in challenging times*, Jun. 2011, pp. 282–291.

[10] J. G. Andrews, S. Buzzi, W. Choi, S. V. Hanly, A. Lozano, A. C. Soong, and J. C. Zhang, "What will 5G be?" *IEEE J. Sel. Areas Commun.*, vol. 32, no. 6, pp. 1065–1082, Jun. 2014.

[11] 3GPP TS 23.501 v 16.5.0, "5G; System architecture for the 5G system (5GS)," Jul. 2020.

[12] BuildWise, "Project: The development of a software tool to design buildings with tailored wireless performance," 2017. [Online]. Available: https://www.era-learn.eu/network-information/networks/eurostars-2/eurostars-2-cut-off-6/the-development-of-a-software-tool-to-design-buildings-with-tailored-wireless-performance

[13] NGMN, "5G E2E technology to support verticals URLLC requirements," Jun. 2021. [Online]. Available: https://www.ngmn.org/publications/5g-e2e-technology-to-support-verticals-urllc-requirements.html

[14] P. Schulz, M. Matthe, H. Klessig, M. Simsek, G. Fettweis, J. Ansari, S. A. Ashraf, B. Almeroth, J. Voigt, I. Riedel *et al.*, "Latency critical iot applications in 5G: Perspective on the design of radio interface and network architecture," *IEEE Commun. Mag.*, vol. 55, no. 2, pp. 70–78, Feb. 2017.

[15] L. Wang, K.-K. Wong, R. W. Heath, and J. Yuan, "Wireless powered dense cellular networks: How many small cells do we need?" *IEEE J. Sel. Areas Commun.*, vol. 35, no. 9, pp. 2010–2024, Jun. 2017.

[16] 3GPP TR 38.901 v 16.1.0, "Study on Channel Model for Frequencies From 0.5 to 100 GHz," Nov. 2020.

[17] C. Gabriel, "Distributed massive MIMO is a breakthrough in delivering a high-quality 5G experience indoors," Mar. 2021. [Online]. Available: https://www.analysysmason.com/contentassets/fc65541db6c4489cabe0e7e30bf5b761/analysys_mason_distributed_massive_mimo_mar2021_rma18.pdf

[18] D. Gesbert, M. Kountouris, R. W. Heath, C.-B. Chae, and T. Salzer, "Shifting the mimo paradigm," *IEEE signal processing magazine*, vol. 24, no. 5, pp. 36–46, Sep. 2007.

[19] H. Q. Ngo, E. G. Larsson, and T. L. Marzetta, "Energy and spectral efficiency of very large multiuser mimo systems," *IEEE Transactions on Communications*, vol. 61, no. 4, pp. 1436–1449, Feb. 2013.

[20] F. Rusek, D. Persson, B. K. Lau, E. G. Larsson, T. L. Marzetta, O. Edfors, and F. Tufvesson, "Scaling up mimo: Opportunities and challenges with very large arrays," *IEEE signal processing magazine*, vol. 30, no. 1, pp. 40–60, Dec. 2012.

[21] V. Nurmela, A. Karttunen, A. Roivainen, L. Raschkowski, V. Hovinen, J. Y. EB, N. Omaki, K. Kusume, A. Hekkala, R. Weiler *et al.*, "Deliverable d1. 4 metis channel models," *Proc. Mobile Wireless Commun. Enablers Inf. Soc.(METIS)*, vol. 1, Feb. 2015.

[22] L. Zhou, D. Wu, J. Chen, and Z. Dong, "Greening the smart cities: Energy-efficient massive content delivery via d2d communications," *IEEE Trans. Industr. Inform.*, vol. 14, no. 4, pp. 1626–1634, Dec. 2017.

[23] G. De la Roche, A. Alayón-Glazunov, and B. Allen, *LTE-advanced and next generation wireless networks: channel modelling and propagation*. John Wiley & Sons, Nov. 2012.

[24] M. K. Müller, M. Taranetz, and M. Rupp, "Analyzing wireless indoor communications by blockage models," *IEEE Access*, vol. 5, pp. 2172–2186, Dec. 2016.

[25] W. C. Jakes and D. C. Cox, *Microwave mobile communications*. Wiley-IEEE press, Sep. 1994.

[26] M. J. Gans, "A power-spectral theory of propagation in the mobile-radio environment," *IEEE Trans. Veh. Technol.*, vol. 21, no. 1, pp. 27–38, Feb. 1972.

[27] T. A. Sexton and K. Pahlavan, "Channel modeling and adaptive equalization of indoor radio channels," *IEEE J. Sel. Areas Commun.*, vol. 7, no. 1, pp. 114–121, Jan. 1989.

[28] S. Howard and K. Pahlavan, "Performance of a DFE modem evaluated from measured indoor radio multipath profiles," in *IEEE International Conference on Communications, Including Supercomm Technical Sessions*. IEEE, Apr. 1990, pp. 1341–1345.

[29] B. Ai, K. Guan, R. He, J. Li, G. Li, D. He, Z. Zhong, and K. M. S. Huq, "On indoor millimeter wave massive MIMO channels: Measurement and simulation," *IEEE J. Sel. Areas Commun. in communications*, vol. 35, no. 7, pp. 1678–1690, Apr. 2017.

[30] A. Á. Polegre, F. Riera-Palou, G. Femenias, and A. G. Armada, "Channel hardening in cell-free and user-centric massive MIMO networks with spatially correlated Ricean fading," *IEEE Access*, vol. 8, pp. 139 827–139 845, Jul. 2020.

[31] J. Zhang, A. A. Glazunov, W. Yang, and J. Zhang, "Fundamental wireless performance of a building," *IEEE Wireless Commun.*, vol. 29, no. 1, pp. 186–193, Apr. 2021.

[32] J. Zhang, A. A. Glazunov, and J. Zhang, "Wireless performance evaluation of building layouts: Closed-form computation of figures of merit," *IEEE Trans. Commun.*, vol. 69, no. 7, pp. 4890–4906, Apr. 2021.

[33] ——, "Wireless energy efficiency evaluation for buildings under design based on analysis of interference gain," *IEEE Trans. Veh. Technol.*, vol. 69, no. 6, pp. 6310–6324, 2020.

[34] Y. Yu, Y. Liu, W.-J. Lu, and H.-B. Zhu, "Measurement and empirical modelling of root mean square delay spread in indoor femtocells scenarios," *IET Commun.*, vol. 11, no. 13, pp. 2125–2131, Sep. 2017.

[35] J. Meinilä, P. Kyösti, T. Jämsä, and L. Hentilä, "Winner II channel models," in *Radio Technologies and Concepts for IMT-Advanced*, Apr. 2008.

[36] ITU, "IMT Vision – Framework and overall objectives of the future development of IMT for 2020 and beyond," Sep. 2015. [Online]. Available: https://www.itu.int/dms_pubrec/itu-r/rec/m/R-REC-M.2083-0-201509-I!!PDF-E.pdf

[37] A. Aragón-Zavala, *Indoor wireless communications: From theory to implementation*. John Wiley & Sons, Sep. 2017.

[38] J. M. Keenan and A. J. Motley, "Radio coverage in buildings," *Brit Telecom Technol. J.*, vol. 8, no. 1, pp. 19–24, 1990.

[39] P. Series, "Propagation data and prediction methods for the planning of indoor radio-communication systems and radio local area networks in the frequency range 900 MHz to 100 GHz," *Recommendation ITU-R*, pp. 1238–7, Feb. 2012.

[40] D. Akerberg, "Properties of a TDMA pico cellular office communication system," in *IEEE 39th Vehicular Technology Conference*. IEEE, May 1989, pp. 186–191.

[41] S.-C. Tuan, J.-C. Chen, H.-T. Chou, and H.-H. Chou, "Optimization of propagation models for the radio performance evaluation of wireless local area network," in *IEEE Antennas and Propagation Society International Symposium. Digest.*, vol. 2. IEEE, Jun. 2003, pp. 146–149.

[42] W. Honcharenko, H. L. Bertoni, J. L. Dailing, J. Qian, and H. Yee, "Mechanisms governing UHF propagation on single floors in modern office buildings," *IEEE Trans. Veh. Technol.*, vol. 41, no. 4, pp. 496–504, Nov. 1992.

[43] Remcom, "Electromagnetic simulation software," 2016. [Online]. Available: http://www.remcom.com/

[44] G. Wolfle, B. Gschwendtner, and F. Landstorfer, "Intelligent ray tracing-a new approach for field strength prediction in microcells," in *1997 IEEE 47th Vehicular Technology Conference. Technology in Motion*, vol. 2. IEEE, May 1997, pp. 790–794.

[45] K.-W. Cheung, J.-M. Sau, and R. D. Murch, "A new empirical model for indoor propagation prediction," *IEEE Trans. Veh. Technol.*, vol. 47, no. 3, pp. 996–1001, Aug. 1998.

[46] A. Aragon-Zavala, B. Belloul, V. Nikolopoulos, and S. Saunders, "Accuracy evaluation analysis for indoor measurement-based radio-wave-propagation predictions," *IEE Proceedings-Microwaves, Antennas and Propagation*, vol. 153, no. 1, pp. 67–74, Feb. 2006.

[47] A. D. Wyner, "Shannon-theoretic approach to a Gaussian cellular multiple-access channel," *IEEE Trans. Inf. Theory*, vol. 40, no. 6, pp. 1713–1727, Nov. 1994.

[48] S. Shamai and A. D. Wyner, "Information-theoretic considerations for symmetric, cellular, multiple-access fading channels. i," *IEEE Trans. Inf. Theory*, vol. 43, no. 6, pp. 1877–1894, Nov. 1997.

[49] ——, "Information-theoretic considerations for symmetric, cellular, multiple-access fading channels. II," *IEEE Trans. Inf. Theory*, vol. 43, no. 6, pp. 1895–1911, Nov. 1997.

[50] S. Musa and W. Wasylkiwskyj, "Co-channel interference of spread spectrum systems in a multiple user environment," *IEEE Trans. Commun.*, vol. 26, no. 10, pp. 1405–1413, Oct. 1978.

[51] D. Stoyan, W. S. Kendall, S. N. Chiu, and J. Mecke, *Stochastic geometry and its applications*. John Wiley & Sons, Jun. 2013.

[52] J. F. C. Kingman, *Poisson processes*. Clarendon Press, Dec. 1992, vol. 3.

[53] D. J. Daley and D. Vere-Jones, *An introduction to the theory of point processes: volume II: general theory and structure*. Springer Science & Business Media, Nov. 2007.

[54] J. G. Andrews, F. Baccelli, and R. K. Ganti, "A tractable approach to coverage and rate in cellular networks," *IEEE Trans. Commun.*, vol. 59, no. 11, pp. 3122–3134, Oct. 2011.

[55] N. Deng, W. Zhou, and M. Haenggi, "The ginibre point process as a model for wireless networks with repulsion," *IEEE Trans. Wirel. Commun.*, vol. 14, no. 1, pp. 107–121, Jun. 2014.

[56] H. S. Dhillon, R. K. Ganti, and J. G. Andrews, "A tractable framework for coverage and outage in heterogeneous cellular networks," in *2011 information theory and applications workshop*. IEEE, Feb. 2011, pp. 1–6.

[57] Y. J. Chun, M. O. Hasna, and A. Ghrayeb, "Modeling heterogeneous cellular networks interference using poisson cluster processes," *IEEE J. Sel. Areas Commun.*, vol. 33, no. 10, pp. 2182–2195, May 2015.

[58] N. Deng, W. Zhou, and M. Haenggi, "Heterogeneous cellular network models with dependence," *IEEE J. Sel. Areas Commun*, vol. 33, no. 10, pp. 2167–2181, May 2015.

[59] X. Zhang and J. G. Andrews, "Downlink cellular network analysis with multi-slope path loss models," *IEEE Trans. Commun.*, vol. 63, no. 5, pp. 1881–1894, Mar. 2015.

[60] C. Galiotto, N. K. Pratas, N. Marchetti, and L. Doyle, "A stochastic geometry framework for LOS/NLOS propagation in dense small cell networks," in *2015 IEEE International Conference on Communications (ICC)*. IEEE, Jun. 2015, pp. 2851–2856.

[61] M. Ding, P. Wang, D. López-Pérez, G. Mao, and Z. Lin, "Performance impact of LoS and NLoS transmissions in dense cellular networks," *IEEE Trans. Wirel. Commun.*, vol. 15, no. 3, pp. 2365–2380, Nov. 2015.

[62] J. Arnau, I. Atzeni, and M. Kountouris, "Impact of LOS/NLOS propagation and path loss in ultra-dense cellular networks," in *2016 IEEE international conference on communications (ICC)*. IEEE, May 2016, pp. 1–6.

[63] M. Ding, D. Lopez-Perez, G. Mao, and Z. Lin, "Performance impact of idle mode capability on dense small cell networks," *IEEE Trans. Veh. Technol.*, vol. 66, no. 11, pp. 10 446–10 460, Sep. 2017.

[64] 3GPP TR 36.814 v 9.0.0, "Evolved universal terrestrial radio access (E-UTRA); Further advancements for E-UTRA physical layer aspects," Mar. 2020.

[65] B. Mondal, T. A. Thomas, E. Visotsky, F. W. Vook, A. Ghosh, Y.-H. Nam, Y. Li, J. Zhang, M. Zhang, Q. Luo *et al.*, "3D channel model in 3GPP," *IEEE Commun. Mag.*, vol. 53, no. 3, pp. 16–23, Mar. 2015.

[66] S. Sun, T. A. Thomas, T. S. Rappaport, H. Nguyen, I. Z. Kovacs, and I. Rodriguez, "Path loss, shadow fading, and line-of-sight probability models for 5G urban macro-cellular scenarios," in *2015 IEEE Globecom Workshops (GC Wkshps)*, Dec. 2015, pp. 1–7.

[67] H. Zheng, J. Zhang, H. Li, Q. Hong, H. Hu, and J. Zhang, "Exact line-of-sight probability for channel modeling in typical indoor environments," *IEEE Antennas Wireless Propag. Lett.*, vol. 17, no. 7, pp. 1359–1362, Jun. 2018.

[68] W. Yang, J. Zhang, A. A. Glazunov, and J. Zhang, "Line-of-sight probability for channel modeling in 3-D indoor environments," *IEEE Antennas Wirel. Propag. Lett.*, vol. 19, no. 7, pp. 1182–1186, May 2020.

[69] K. R. Schaubach, N. J. Davis, and T. S. Rappaport, "A ray tracing method for predicting path loss and delay spread in microcellular environments," in *[1992 Proceedings] Vehicular Technology Society 42nd VTS Conference-Frontiers of Technology*. IEEE, May 1992, pp. 932–935.

[70] K. Rizk, J.-F. Wagen, and F. Gardiol, "Two-dimensional ray-tracing modeling for propagation prediction in microcellular environments," *IEEE Trans. Veh. Technol.*, vol. 46, no. 2, pp. 508–518, May 1997.

[71] T. Bai, R. Vaze, and R. W. Heath, "Using random shape theory to model blockage in random cellular networks," in *2012 International Conference on Signal Processing and Communications (SPCOM)*. IEEE, Jul. 2012, pp. 1–5.

[72] ——, "Analysis of blockage effects on urban cellular networks," *IEEE Trans. Wirel. Commun*, vol. 13, no. 9, pp. 5070–5083, Jun. 2014.

[73] M. K. Müller, M. Taranetz, and M. Rupp, "Effects of wall-angle distributions in indoor wireless communications," in *2016 IEEE 17th International Workshop on Signal Processing Advances in Wireless Communications (SPAWC)*. IEEE, Jul. 2016, pp. 1–5.

[74] F. Baccelli and X. Zhang, "A correlated shadowing model for urban wireless networks," in *2015 IEEE Conference on Computer Communications (INFOCOM)*. IEEE, Apr. 2015, pp. 801–809.

[75] J. Lee, X. Zhang, and F. Baccelli, "A 3-D spatial model for in-building wireless networks with correlated shadowing," *IEEE Trans. Wirel. Commun*, vol. 15, no. 11, pp. 7778–7793, Sep. 2016.

[76] W. Yang, J. Zhang, H. Song, and J. Zhang, "Partition-based analytic evaluation of building wireless performance," *IEEE Trans. Veh. Technol.*, vol. 70, no. 9, pp. 9036–9049, Jul. 2021.

[77] J. Wen, S. Lee, G. Lee, and J. Chang, "Timing and delay spread estimation scheme in OFDM systems," *IEEE Transactions on Consumer Electronics*, vol. 54, no. 2, pp. 316–320, May 2008.

[78] R. Sun and D. W. Matolak, "Path loss and delay spread for the stairwell channel at 5 GHz," *Int. J. Commun. Syst.*, vol. 30, no. 1, p. e2920, Jan. 2017.

[79] D. Cassioli, L. A. Annoni, and S. Piersanti, "Characterization of path loss and delay spread of 60-GHz UWB channels vs. frequency," in *2013 IEEE International Conference on Communications (ICC)*, Nov. 2013, pp. 5153–5157.

[80] A. G. Siamarou and M. Al-Nuaimi, "Multipath delay spread and signal level measurements for indoor wireless radio channels at 62.4 GHz," in *IEEE VTS 53rd Vehicular Technology Conference, Spring 2001. Proceedings (Cat. No. 01CH37202)*, vol. 1, May 2001, pp. 454–458.

[81] H. Hashemi and D. Tholl, "Analysis of the RMS delay spread of indoor radio propagation channels," in *SUPERCOMM/ICC'92 Discovering a New World of Communications*, Jun. 1992, pp. 875–881.

[82] J. Weng, X. Tu, Z. Lai, S. Salous, and J. Zhang, "Indoor massive MIMO channel modelling using ray-launching simulation," *Int. J. Antennas Propag.*, vol. 2014, Aug. 2014.

[83] A. P. Guevara and S. Pollin, "Densely deployed indoor massive MIMO experiment: From small cells to spectrum sharing to cooperation," *Sensors*, vol. 21, no. 13, p. 4346, Jun. 2021.

[84] C. Sanchis-Borrás, M.-T. Martinez-Ingles, and J.-M. Molina-Garcia-Pardo, "Massive MIMO indoor transmissions at 38 and 65 GHz applying novel hbf techniques for 5G," *Sensors*, vol. 22, no. 10, p. 3716, May 2022.

[85] H. Q. Ngo, A. Ashikhmin, H. Yang, E. G. Larsson, and T. L. Marzetta, "Cell-free massive MIMO: Uniformly great service for everyone," in *2015 IEEE 16th international workshop on signal processing advances in wireless communications (SPAWC)*. IEEE, Jun. 2015, pp. 201–205.

[86] ——, "Cell-free massive MIMO versus small cells," *IEEE Trans. Wirel. Commun*, vol. 16, no. 3, pp. 1834–1850, Jan. 2017.

[87] Z. Chen and E. Björnson, "Channel hardening and favorable propagation in cell-free massive MIMO with stochastic geometry," *IEEE Trans. Commun.*, vol. 66, no. 11, pp. 5205–5219, Jun. 2018.

[88] G. Interdonato, H. Q. Ngo, E. G. Larsson, and P. Frenger, "How much do downlink pilots improve cell-free massive MIMO?" in *2016 IEEE Global Communications Conference (GLOBECOM)*. IEEE, Dec. 2016, pp. 1–7.

[89] A. Á. Polegre, F. Riera-Palou, G. Femenias, and A. G. Armada, "New insights on channel hardening in cell-free massive MIMO networks," in *2020 IEEE International Conference on Communications Workshops*, Jun. 2020, pp. 1–7.

[90] H. Q. Ngo and E. G. Larsson, "No downlink pilots are needed in TDD massive MIMO," *IEEE Trans. Wireless Commun.*, vol. 16, no. 5, pp. 2921–2935, May 2017.

[91] L. Sanguinetti, E. Björnson, and J. Hoydis, "Toward massive MIMO 2.0: Understanding spatial correlation, interference suppression, and pilot contamination," *IEEE Trans. Commun.*, vol. 68, no. 1, pp. 232–257, Oct. 2019.

[92] E. Björnson, J. Hoydis, L. Sanguinetti *et al.*, "Massive MIMO networks: Spectral, energy, and hardware efficiency," *Found. Trends Signal Process.*, vol. 11, no. 3-4, pp. 154–655, Nov. 2017.

[93] 3GPP TS 22.104 v 17.0.0, "Service requirements for cyber-physical control applications in vertical domains," Jun. 2019.

[94] NGMN, "5G E2E Technology to Support Verticals URLLC Requirement," Nov. 2019. [Online]. Available: https://www.ngmn.org/wp-content

[95] 3GPP TR 22.804 v 16.3.0, "Study on communication for automation in vertical domains," Jun. 2020.

[96] R. Sabella, A. Thuelig, M. Carrozza, and M. Ippolito, "Industrial automation enabled by robotics, machine intelligence and 5G," Feb. 2018. [Online].

Available: https://www.ericsson.com/en/ericsson-technology-review/archive/2018/industrial-automation-enabled-by-roboticsmachine-intelligence-and-5g

[97] T. S. Rappaport, *Wireless communications: principles and practice*. prentice hall PTR New Jersey, Jan. 1996, vol. 2.

[98] T. T. Ha, *Theory and design of digital communication systems*. Cambridge University Press, Oct. 2010.

[99] J. Walrand and P. P. Varaiya, *High-performance communication networks*. Morgan Kaufmann, Oct. 1999.

[100] V. Diez, A. Arriola, I. Val, and M. Velez, "Reliability evaluation of point-to-point links based on IEEE 802.15. 4 physical layer for IWSAN applications," *Int. J. Electron. Commun.*, vol. 113, p. 152967, Jan. 2020.

[101] W. Debaenst, A. Feys, I. Cuiñas, M. Garcia Sanchez, and J. Verhaevert, "RMS delay spread vs. coherence bandwidth from 5G indoor radio channel measurements at 3.5 GHz band," *Sensors*, vol. 20, no. 3, p. 750, Jan. 2020.

[102] 3GPP TS 38.300 v 16.0.0, "NR; Overall description; Stage-2," Dec. 2019.

[103] 3GPP TR 38.913 v 16.0.0, "Study on scenarios and requirements for next generation access technologies," Jul. 2018.

[104] W. Shieh and I. B. Djordjevic, *OFDM for optical communications*. Academic press, Sep. 2009.

[105] H. Hashemi, "Impulse response modeling of indoor radio propagation channels," *IEEE J. Sel. Areas Commun.*, vol. 11, no. 7, pp. 967–978, Sep. 1993.

[106] H. Hashemi and D. Tholl, "Statistical modeling and simulation of the RMS delay spread of indoor radio propagation channels," *IEEE Trans. Veh. Technol.*, vol. 43, no. 1, pp. 110–120, Feb. 1994.

[107] M. S. Varela and M. G. Sánchez, "RMS delay and coherence bandwidth measurements in indoor radio channels in the UHF band," *IEEE Trans. Veh. Technol.*, vol. 50, no. 2, pp. 515–525, Mar. 2001.

[108] Y. Zahedi, R. Ngah, S. Nunoo, M. Mokayef, S. Alavi, and I. Amiri, "Experimental measurement and statistical analysis of the RMS delay spread in time-varying ultra-wideband communication channel," *Measurement*, vol. 89, pp. 179–188, Jul. 2016.

[109] D. Coko and I. Marinovic, "RMS delay spread assessment for indoor UWB propagation channels," *Wirel. Pers. Commun.*, vol. 95, no. 3, pp. 2625–2633, Aug. 2017.

[110] R. Sharma, A. C. Kumari, M. Aggarwal, and S. Ahuja, "Improved RMS delay and optimal system design of LED based indoor mobile visible light communication system," *Phys. Commun.*, vol. 28, pp. 89–96, Jun. 2018.

[111] Y. Yu, Y. Liu, W.-J. Lu, and H.-B. Zhu, "Antenna-height-dependent delay spread model under indoor stair environment for small cell deployment in future mobile communications," *IEEJ Trans. Electr. Electron. Eng.*, vol. 10, pp. S7–S13, Oct. 2015.

[112] A. Saakian, *Radio wave propagation fundamentals*. Artech House, Dec. 2020.

[113] S. Willhammar, J. Flordelis, L. Van Der Perre, and F. Tufvesson, "Channel hardening in massive MIMO: Model parameters and experimental assessment," *IEEE Open Journal of the Communications Society*, vol. 1, pp. 501–512, Apr. 2020.

[114] N. Pourjafari and J. Seifali Harsini, "On the complete convergence of channel hardening and favorable propagation properties in massive-MIMO communications systems," *J. Math Model*, vol. 7, no. 4, pp. 429–443, Dec. 2019.

[115] G. Geraci, A. Garcia-Rodriguez, D. López-Pérez, L. G. Giordano, P. Baracca, and H. Claussen, "Indoor massive mimo deployments for uniformly high wireless capacity," in *2018 IEEE Wireless Communications and Networking Conference (WCNC)*. IEEE, Apr. 2018, pp. 1–6.

[116] M. Giordani, M. Polese, M. Mezzavilla, S. Rangan, and M. Zorzi, "Toward 6G networks: Use cases and technologies," *IEEE Commun. Mag.*, vol. 58, no. 3, pp. 55–61, Dec. 2020.

[117] V. W. Wong, R. Schober, D. W. K. Ng, and L.-C. Wang, *Key technologies for 5G wireless systems*. Cambridge university press, Mar. 2017.

[118] L. Pérez-Lombard, J. Ortiz, and C. Pout, "A review on buildings energy consumption information," *Energy Build.*, vol. 40, no. 3, pp. 394–398, Jan. 2008.

[119] W. Yang, J. Zhang, and J. Zhang, "Machine learning based indoor line-of-sight probability prediction," in *Proc. IEEE ISAP*. IEEE, Dec. 2019, pp. 1–3.